Rational Design and Engineering of Metal-based Nanomaterials for Multifunctional Electrocatalysis

by

Hangxuan Li

A thesis submitted in partial fulfillment of the requirements for the degree of

Master of Science

Department of Mechanical Engineering
University of Alberta

Abstract

Multifunctional electrocatalysis plays an important role in renewable energy conversion, supporting a variety of clean energy devices such as fuel cells, electrolyzers, and metal-air batteries. Hydrogen evolution reaction (HER), oxygen evolution reaction (OER), and oxygen reduction reaction (ORR) are the most significant electrocatalytic reactions that have attracted great research interest. However, several challenges still exist in the design and fabrication of electrocatalysts in terms of cost, performance, and stability.

To address these issues, I attempt to tackle the problems of both cost and electrocatalytic performance, and also fabricate the multifunctional catalysts for different half reactions. Based on the literature review of recent works, I successfully fabricated the transition metal-based nanomaterials supported on the nickel foam and it shows bifunctional electrocatalytic performance for HER and OER.

Chapter 1 is a literature review on novel Pd-based and transition metal-based nanomaterials for multifunctional ORR/OER/HER electrocatalysis in both acidic and alkaline media. The mechanism of electrocatalytic reactions and the challenges of both Pd-based and transition metal-based catalysts are demonstrated. Effective strategies such as alloying design, single-atom catalyst design, interface engineering, and heterojunction construction are summarized.

Chapter 2 clarifies the objectives and experimental design based on the literature review.

Chapter 3 is an experimental section for the design and fabrication of transition metal-based heterogeneous structural Co_2P-Ni_3S_2 hollow nanowires supported on nickel foam (Co_2P-Ni_3S_2/NF). Owing to the multiple active sites provided by transition metal

compounds, the large surface area of the unique hollow nanowire morphology, and the synergistic effect of Co_2P-Ni_3S_2 heterostructure interfaces, the as-prepared catalyst exhibits remarkable bifunctional HER/OER performance. It requires ultralow overpotentials of 110, 164 mV for HER and 331.7, 358.3 mV for OER at large current densities of 100, 500 mA cm^{-2} in alkaline medium, respectively. Impressively, the two-electrode electrolyzer assembled by Co_2P-Ni_3S_2/NF displays a cell voltage of 1.54 V at 10 mA cm^{-2} and operates stably over 24 h at 100 mA cm^{-2}.

Chapter 4 briefly summarizes recent progress in the literature review and experimental results in the first three chapters, analyzes the existing challenges, and proposes future prospects.

Preface

This thesis is an original work by Hangxuan Li under the supervision of Dr. Ge Li. Section 1.3.1 in Chapter 1 of this thesis has been published as H. Li, G. Li, Novel Palladium-based Nanomaterials towards Multifunctional ORR/OER/HER Electrocatalysis, J. Mater. Chem. A (2023). I finished the original manuscript, organized figures, and managed references. Dr. Ge Li contributed to the supervision, review, and editing of the manuscript.

This thesis is dedicated to

my parents, Gaohe Li and Sha Tang,

for their love

Acknowledgements

I would like to thank my supervisor, Dr. Ge Li, for giving me the valuable opportunity to work in the research group at the Department of Mechanical Engineering, University of Alberta. Her support, guidance, and supervision were vital for my study and research. When I encountered difficulties in the lab, Dr. Li always gave me guidance, and I could follow her instructions to solve the problem. The professional knowledge imparted by Dr. Li will play an important role in my future career.

I would like to thank all the group members, for their help, support, encouragement, understanding, and companionship all the time.

I would like to thank all the staff and professors in the Department of Mechanical Engineering, for their help, knowledge, and guidance.

I would also like to thank the Natural Sciences and Engineering Research Council of Canada (NSERC) and the Canada First Research Excellence Fund to support my research.

Table of contents

List of tables

List of figures

List of abbreviations

ORR	Oxygen reduction reaction
OER	Oxygen evolution reaction
HER	Hydrogen evolution reaction
Pt/C	Platinum on carbon
MOF	Metal organic frameworks
SAAs	Single-atom alloys
HSAG	High surface area graphite
PTH	Polythiophene
DACs	Dual-atom catalysts
rGO	Reduced graphene oxide
COF	Covalent organic frameworks
TMP	Transition metal phosphides
TMS	Transition metal sulfides
TMN	Transition metal nitrides
TMC	Transition metal carbides
TMO	Transition metal oxides
2D	Two-dimensional
3D	Three-dimensional
SACs	Single-atom catalysts
TOF	Turnover frequency
NF	Nickel foam
CNT	Carbon nanotubes
NCNT	Nitrogen-doped carbon nanotubes
DFT	Density functional theory
RDS	Rate-determining step
EIS	Electrochemical impedance spectroscopy
XPS	X-ray photoelectron spectroscopy

ZIF	Zeolitic imidazolate framework
TEM	Transmission electron microscopy
HRTEM	High-resolution transmission electron microscopy
CNF	Carbon nanofibers
SEM	Scanning electron microscope
LSV	Linear sweep voltammetry
XRD	X-ray diffraction patterns
LDH	Layered double hydroxide
HAADF-STEM	High-angle annular dark-field scanning transmission electron microscopy
DESs	Deep eutectic solvents
C_{dl}	Double-layer capacitances
ECSA	Electrochemical surface area
CC	Carbon cloth
CV	Cyclic voltammetry
ZAB	Zinc air battery
DI	Deionized water
FESEM	Field emission scanning electron microscopy
EDS	Energy dispersive spectrometer
SCE	Saturated calomel electrode
RHE	Reversible hydrogen electrode
CA	Contact angle

Chapter 1. Literature review

1.1 Introduction

With the growth of the earth's population worldwide and industrialization in developing countries, the demand for energy by humans has reached an unprecedented level [1]. The majority resource of energy in daily life comes from fossil fuels. However, the huge consumption of fossil fuels has caused many problems in the last 50 years [2]. For example, the rising emissions of greenhouse gas are closely related to the combustion of fossil fuels. Besides, due to the non-renewability of fossil fuels, people may face a shortage problem of fossil fuels in the next few decades. Hence, seeking alternatives to fossil fuels is very important to address the energy and environmental problems of the 21st century [3]. Oxygen reduction reaction (ORR), oxygen evolution reaction (OER), and hydrogen evolution reaction (HER) are the most important half reactions with extensive applications in electrocatalysis [4]. These reactions play a critical role in many clean energy conversion technologies, including hydrogen production, electrochemical cells, and carbon dioxide reduction. For example, water splitting electrolyzer can realize the decomposition of water into hydrogen and oxygen, becoming one of the most promising hydrogen production technologies; Metal-air battery is an electrochemical cell that the redox reactions between the anode and the cathode generate electricity; Fuel cell is also an electrochemical cell that converts the chemical energy of a fuel and oxygen into electricity by redox reactions. In detail, ORR occurs in the cathode of fuel cells; Water splitting includes the OER and HER; Metal-air battery includes the ORR and OER. Developing efficient and stable electrocatalysts for these reactions becomes more and more important over the years [5]. Pt/C is a commonly used commercial electrocatalyst, but the low scarcity and inferior stability largely impede the development of Pt-based electrocatalysts. At the same time, Pt-based materials cannot be applied to OER electrocatalysis, because the OER performance and stability of Pt-based catalyst is not good as Ru-based or Ir-based catalyts. For OER, the

commercial catalyst is RuO_2 or IrO_2 supported on the carbon, which shows similar problems to the commercial Pt/C. Except for the consideration of half reactions, the electrolyte system and practical applications in the device are also important. Moreover, the development of novel nanomaterials for multifunctional electrocatalysis gradually gains researchers' attention due to the demand for energy conversion devices (*e.g.,* fuel cell, electrolyzer, metal-air batteries).

In general, some significant parameters are needed to be considered for electrocatalysis [6], including the cost of the materials, the performance of electrocatalysis (*e.g.,* the overpotential and current density of the reaction), the long-time durability in different working environments [7], the multiple functions towards different electrocatalytic reactions, the complexity of the synthesis processes, *etc.* For these points, researchers have proposed different strategies to solve the relevant questions and have addressed the issues of the materials. To decrease the cost, researchers try to develop non-noble metal-based materials such as transition metal oxides, transition metal sulfides [8], transition metal phosphides, and some carbon materials such as metal graphite, metal–organic frameworks (MOF)-based electrocatalysts [9-11]. To improve intrinsic activity for electrocatalysis, researchers need to construct highly active sites on the surface, such as metal ions (Pd, Fe, Co, Ni, *etc*.), defects, edges, and so on. To promote the high catalytic performance of catalysts, it is of paramount importance to focus on the reaction mechanisms to manipulate the adsorption energy of intermediates and center on several aspects: (1) increase the number of active sites, (2) enhance the adsorption of reactants, (3) accelerate the desorption process of products. Notably, these improvements are relative to materials' geometry structure, morphology, electronic structure, active sites on the surface area, *etc.* To improve the long-time durability during the working potential, various morphologies are designed to stabilize the material structures and reduce the aggregation of the nanoparticles during the electrochemical reactions.

Inspired by the fast development of different strategies to design efficient catalysts in the catalytic research field, in this literature review, the mechanism of electrocatalytic

reactions is clearly demonstrated, and novel metal-based electrocatalysts including Pd-based and transition metal compound-based nanomaterials are summarized. In this chapter, section 1.2 presents the mechanisms of half reactions including OER and HER; section 1.3 presents two different metal-based nanomaterials and corresponding strategies to modify the catalysts; section 1.4 summarizes this chapter and provides prospectives.

1.2 Mechanism

1.2.1 Oxygen evolution reaction (OER)

The OER is the half reaction of water splitting or metal-air battery, which generates oxygen from water, proton, or hydroxyl group [12]. The main mechanism of OER is four-electron/proton transfer steps in acidic or alkaline environment. Based on the pH value of the media, the step reactions and intermediates show a large difference. The overall reaction under acidic conditions of OER is [13]:

$$2H_2O \rightarrow O_2 + 4H^+ + 4e^-$$

The above reaction has the following four steps:

$$H_2O + * \rightarrow {}^*OH + H^+ + e^-$$

$${}^*OH \rightarrow {}^*O + H^+ + e^-$$

$$H_2O + {}^*O \rightarrow {}^*OOH + H^+ + e^-$$

$${}^*OOH \rightarrow * + O_2 + H^+ + e^-$$

The * represents the active sites and the intermediates. The proton and electron transfer distribute evenly in the four steps, and in each step, intermediates are produced or consumed, finally transferred into oxygen. In the process, the number and activity of active sites largely influence the performance of OER [14]. The commonly used materials in the acidic medium are the metal oxides like commercial RuO_2 and IrO_2 supported on carbon, but some materials are not stable in the acidic medium like metal

sulfide and metal phosphite. Therefore, it's important to investigate the OER mechanism occurring in the alkaline medium. The overall reaction under alkaline conditions of OER is:

$$4OH^- \rightarrow O_2 + 2H_2O + 4e^-$$

And the four steps during the whole process:

$$OH^- + * \rightarrow {}^*OH + e^-$$

$${}^*OH + OH^- \rightarrow {}^*O + H_2O + e^-$$

$$OH^- + {}^*O \rightarrow {}^*OOH + e^-$$

$${}^*OOH + OH^- \rightarrow * + O_2 + H_2O + e^-$$

In summary, the proton from the proton provider (H_2O in acidic environment, OH- in alkaline environment) and the electron the overpotential provides have a transfer process on the active sites and the formed intermediates successfully occupy the active sites. With further proton and electron transfer, the intermediates (including *OH, *O, *OOH) react step by step and generate the product [15].

1.2.2 Hydrogen evolution reaction (HER)

Hydrogen evolution reaction involves two reaction steps to convert H^+ or H_2O to the product H_2 [16]. Depending on the pH condition, the reaction varies in the acidic media and the alkaline media [17]. The HER mechanism occurring in the acidic media is shown in the following reaction steps:

$$* + H^+ + e^- \rightarrow H^*$$

$$H^* + H^+ + e^- \rightarrow H_2$$

The first step is the adsorption of protons on the active sites of the catalysts, i.e., the combination of active sites and protons with electron transfer generates the intermediate H*. Then, this intermediate proceeds further proton and electron transfer to generate H_2 and release it, named the electrochemical desorption step [18]. After the generation of the intermediate H*, there is another choice to finish the generation of H_2 shown in the following reaction:

$$H^* + H^* \rightarrow H_2$$

This step is the chemical desorption step [18]. Two intermediate H* combine with each other to form the H_2 and release from the surface of the catalysts. The overall HER reaction is shown in the following reaction involving these two successive steps.

$$2H^+ + 2e^- \rightarrow H_2$$

Similarly, the HER in the alkaline media involves the generation of the intermediate H* and the conversion from the intermediate H* to H_2.

$$* + H_2O + e^- \rightarrow H^* + OH^-$$

$$H^* + H_2O + e^- \rightarrow H_2 + OH^-$$

The conversion from the intermediate H* to H_2 is the electrochemical desorption step and it also could be replaced by the chemical desorption step. And the overall HER reaction in the alkaline media is shown in the following reaction:

$$2H_2O + 2e^- \rightarrow H_2 + 2OH^-$$

Unlike the complex intermediate of other electrocatalytic reactions like ORR and OER, the HER possesses only one intermediate H*. Also, the overall reaction only includes two successive steps, which is simpler than the other ones. Therefore, the catalytic activity is strongly dependent on the interaction between the active sites of the catalysts and the intermediate H*, indicating that the generation, conversion, and interaction of the H* plays a significant role in the HER performance [17]. Based on the Sabatier principle [19], we can use the volcano curve to describe the relationship between the adsorption behavior of the intermediate H* and the HER performance shown in **Figure 1**. According to different approaches, we can evaluate the HER catalytic performance: overpotential with the same current density, Tafel slope, turnover frequency (TOF), *etc*.

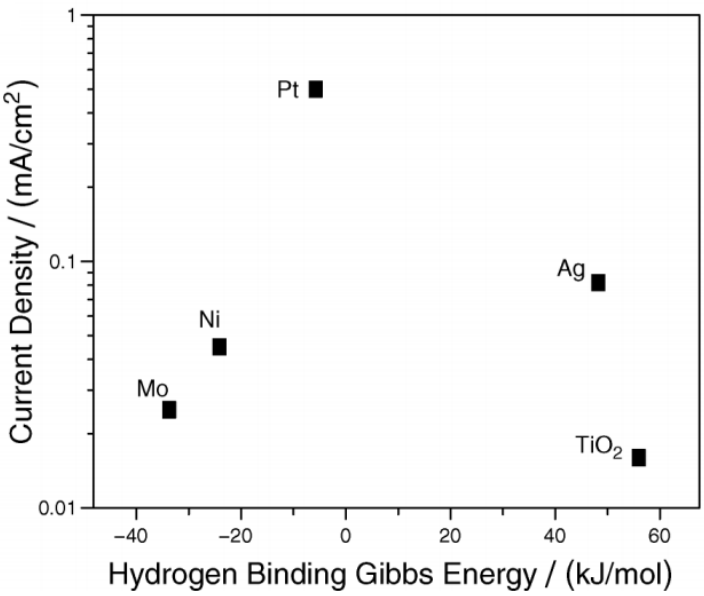

Figure 1. Sabatier plot of the activity of the measured catalysts versus the reactivity described by the DFT calculated hydrogen binding energy. Reproduced with permission. [20] Copyright 2021, American Chemical Society.

1.3 Catalytic metal-based nanomaterials

Platinum-based materials are still state-of-the-art catalysts for ORR, HER, and other electrocatalysis in the acidic conditions. However, the high cost, low scarcity, and poor impurity tolerance of Pt-based materials impose restrictions on the industrial application of energy conversion devices and also stimulate the development of non-platinum electrocatalysts as alternatives [21], including other noble metals like Pd, non-noble metals, metal-free catalysts, *etc*. By comparison of Pt and Pd, it can be concluded that these two noble metals have both commonality and unique characteristics. Both Pd and Pt are platinum group metals, with similar physical and chemical properties like stability in the air [5], the feasibility of alloy, and the designability towards nanostructures. The similar electronic properties of Pd and Pt result in optimal adsorption energy with intermediates. In the Sabatier plot, the nearby position of the elements indicates the similar binding energy, thus possessing the similar intrinsic

activity. Besides, many researchers combined Pd and Pt and used the synergistic effect to enhance the electrocatalytic activity [22-26]. In terms of Pt-based catalysts, the scarcity is low, and stability is inferior in the alkaline conditions. Compared with platinum, Pd is more abundant and the historical price of Pd is lower than Pt, although the price of Pd is higher in recent years. The catalyst fabrication cost is also related to the loading mass of noble metals, and researchers utilized different strategies to address the cost issue like alloying with non-noble metals [22,27-29]. These comparable properties of Pd make it attractive for high-performance electrocatalysis. Based on Pd, researchers can design different materials to meet different requirements for electrocatalytic functions. Pd-based materials have been used for not only ORR, HER, or OER single-functional electrocatalysis, but also multifunctional reactions like water splitting and metal-air batteries. It's hard for only Pd metal to have all the advantages mentioned above including cost, performance, stability, and multifunctional applications, but there are some strategies to improve the overall performance to lower the cost, reduce the overpotential, increase the current density, and enhance the stability. For example, alloying with nonprecious metals, fabricating Pd single-atom catalysts (SACs), synthesizing composite materials, and constructing 2D nanomaterials [30], are good ways to reduce the loading mass of Pd and improve the performance at the same time.

To further reduce costs, it's particularly important to develop non-noble metal-based materials for multifunctional electrocatalysis. Among non-noble metal-based catalysts, transition metal compounds have attracted increasing interest in electrochemistry and energy fields [31-34]. The properties such as intrinsic catalytic activity, low cost [35,36], earth-abundance, and good designability, contribute to the rapid development of transition metal compounds for highly efficient and strongly durable electrocatalysis. There are various types of transition metal compounds, including transition metal phosphides (TMP), transition metal sulfides (TMS), transition metal nitrides (TMN), transition metal carbides (TMC), transition metal oxides (TMO), *etc*. Transition metal compound-based nanomaterials provide numerous active sites [37] for the adsorption

of reactants and intermediates. Specifically, the metal ions in the transition metal compounds serve as the actual active sites, while the anions serve as electron donors for electron regulation [38]. The strong electronic interaction between the metal ions and anions can lead to charge redistribution [39] on the surface, thus optimizing the electronic states and improving the catalytic activity. Moreover, due to the variety of d-orbital electrons [40], the transition metals exhibit various oxidation states in different nanomaterials, resulting in tunable electrocatalytic performance. To further promote the electrocatalytic activity of transition metal compound-based nanomaterials, some strategies have been utilized such as doping [41], alloying, heterostructure construction, interfacial engineering [42], and so on. Transition metal compound-based nanomaterials exhibit superior stability via various fabrication strategies. For example, combining two-dimensional (2D) MoS_2 nanosheets with three-dimensional (3D) Co–Ni–P spheres [43] contributes to the stable structure by preventing particle aggregation and electrochemical deformation.

1.3.1 Palladium-based nanomaterials

1.3.1.1 Alloying design

Alloying is a commonly used method to improve the catalytic activity and stabilize the materials for the Pd-based catalysts [44]. Among different alloying strategies, transition metals are utilized as alloying elements such as Fe, Ni, Co, *etc*. The bimetallic compounds (e.g., Pd-Fe, Pd-Mo) formed by two transition metals benefit the catalytic activity of both metals, lower the price due to the addition of the cheap elements, and improve the durability of the unstable transition metals [45]. Besides, the alloying brings some beneficial effects towards good ORR performance: (1) constructing the controllable morphology and specific geometry like curved bimetallene (**Figure 2c**) [46], (2) causing strain in the surface, (3) adjusting the electronic structure to fit the optimal oxygen binding energy, *etc* [47]. M. Neergat *et al*. prepared Pd-Fe bimetallic

compounds in a low-temperature synthesis route (**Figure 2b**) [48], and concluded that the low-temperature treatment maintained the size of PdFe bimetallic crystals without surface segregation, the performance results showed a good methanol tolerance. This early work indicated the key points of alloy syntheses.

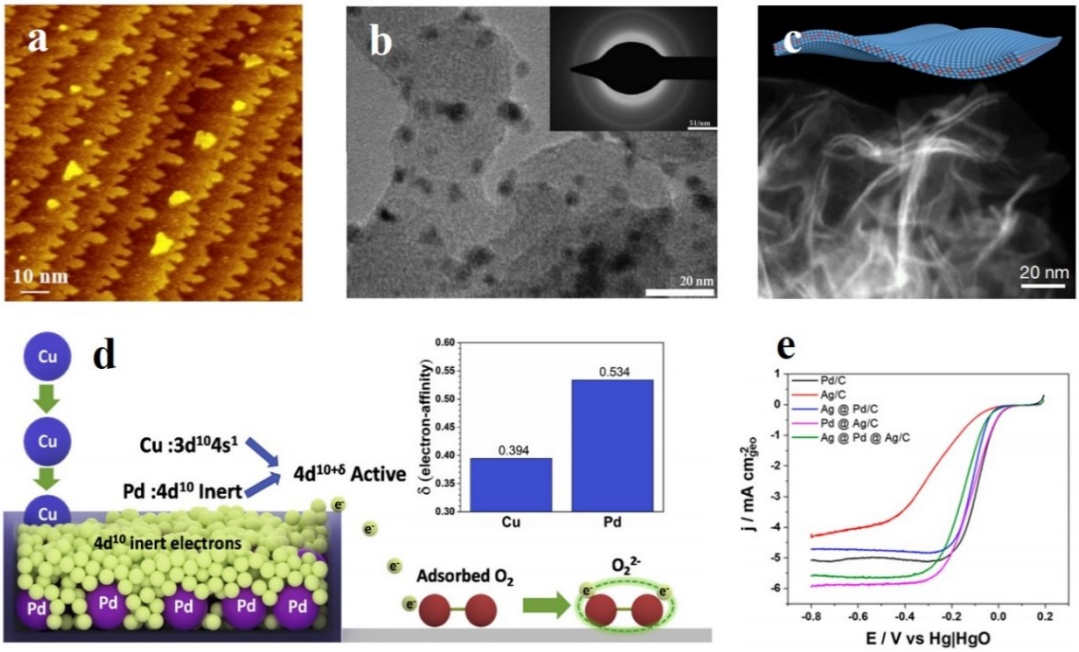

Figure 2. (a) STM image after deposition of 0.4 ML Au on $Pd_3Fe(111)$ at 300 K. Au films grew preferentially at step edges and formed 2-D nanoislands (~5 nm) and nanogaps (~2 nm). Image size: (100 * 100) nm^2. Reproduced with permission. [27] Copyright 2019, John Wiley and Sons. (b) TEM image of 20 wt.% Pd_3Fe/C. Inset shows selected area diffraction pattern of Pd_3Fe/C. Reproduced with permission. [48] Copyright 2011, Elsevier. (c) TEM image of PdMo bimetallene. Reproduced with permission. [46] Copyright 2019, Springer Nature. (d) Illustration of the active electron-affinity of Pd_3Cu for boosting the alkaline ORR. Inset: Determination of electron-affinity of Pd and Cu. Reproduced with permission. [28] Copyright 2019, Elsevier. (e) Electrochemical oxygen reduction reaction (ORR) activity comparison between Ag and Pd alloys and their pure constituents. Reproduced with permission. [49] Copyright 2020, American Chemical Society.

Recently, Luis E. Betancourt *et al*. designed the interactions between Pd and Ag to synthesize the Pd-Ag alloy supported on carbon [49]. The deposition of Pd tuned the

electronic properties of the catalyst and increased the ORR performance twice that of Pd/C (**Figure 2e**). The Pd in the alloy accelerated the adsorption of reactants and the Ag facilitated the desorption step of the products, demonstrating a unique collaboration way of the bimetallic alloys towards ORR. In order to investigate the original influences of different Pd-based bimetallic alloys, Georgios Bampos *et al*. [29] researched several kinds of alloys like Pd-Cu, Pd-Ag, Pd-Ca, Pd-Ni synthesized by wet impregnation method and compared their intrinsic ORR activities. According to electrochemical tests and various characterization techniques, the Pd-Cu performs best due to the optimal Pd lattice strain among all the alloys. In another work, Tong Wu *et al*. [28] applied DFT (Density Functional Theory) calculation to study the intrinsic properties of Pd_3Cu and tried to explain the excellent balance between activity and durability (**Figure 2d**). According to the construction of a possible reaction mechanism occurring on the Pd_3Cu surface, the researcher analyzed the adsorption strengths of reaction intermediates and the electron-affinitive property, thus developing the application of d-band center theory for the explanation of ORR activity.

However, problems of catalytic activity and stability still exist in binary alloys. Considering that two active metals provide optimal electronic property, oxygen binding energy, and super good performance, they cannot maintain stable under a working environment like the alkaline medium due to the high activity [50]. To solve the problems existing in the binary alloy catalysts, researchers start to try more components in the alloy compound, like ternary alloys. Xiaofang Yang *et al*. [27] used the inactive bulk gold to cover the surface of the Pd-Fe alloy catalyst and the results showed large improvement in stability (**Figure 2a**). In this compound, the part of Pd-Fe performed highly active ORR performance and Au served as an electronic modifier and structural stabilizer. This balancing strategy took advantage of different metals' properties and verified the feasibility of ternary alloy catalysts. Xian Jiang *et al*. [51] grew PdPb bimetallic alloy nanolayers on the Au nanowires to fabricate the trimetallic catalyst for highly active ORR reaction. The core-shell structure of Au@PdPb and the anisotropic one-dimensional nanowire morphology largely increased the utilization efficiency of

noble metal atoms, exhibiting enhanced ORR activity. Compared to zero-dimensional nanostructure, the anisotropic one-dimensional nanowires could prevent aggregation and dissolution, thus improving the ORR stability. Qiuyan Chen *et al*. [22] designed core-shell nanosheets with Pd, Pt, Ni, and tuned the shell thickness to optimize the electrocatalytic performance. Combining the core-shell morphology and ultra-thin nanosheet structure, this ternary alloy exhibited promising ORR performance compared with commercial Pt/C. However, the material becomes more complex with the additional element and it's hard to predict and control the morphology and structure of ternary alloys. Mashu Torihata *et al*. [23] studied the surface structure and composition of the Pt-Pd-Co ternary alloy, they fabricated several composition ratio compounds and compared several surface planes, and showed that the low index planes of the Pt-Pd-Co ternary alloy had higher activity compared with Pt's corresponding planes. With more elements in the material synthesis, it's hard to control the catalytic properties of the prepared samples. Dinesh Bhalothia *et al*. [24] carefully studied the effect of the third metal Pt in the ternary alloy NiPdPt nanoparticles and showed that the adsorption time and content of Pt had a severe influence on atomic arrangement and charge density distribution of the final ternary alloy nanoparticles. In the presence of atomic Pt clusters on the surface, the defect active sites were well protected thus enhancing the total ORR performance.

The alloying strategy with Pd and non-noble metals indeed provides superior catalytic performance and reduces the cost. However, the reduced atomic percentage of Pd leads to limited durability under harsh operating conditions, especially when the atomic percentage of Pd is lower than 50% [52]. To solve this problem, Zhi-Peng Wu *et al*. [52] developed an alloying-realloying strategy to address the issue of Pd-based alloys' durability. Researchers synthesized PtPdM (M = Cu, Ni or Co) ternary alloy and studied their durability issues by in-situ high-energy synchrotron XRD. Results showed that the dealloying-realloying cycles played an important role in the overall stability. The realloying process occurred in the compressive-strained single-phase alloy state and helped the "self-healing" of the material. Inside the ternary compositions, Pd could

decrease the dealloying degree and facilitate the realloying process, thus improving the durability of the alloying-realloying strategy.

1.3.1.2 Size effect

The size effect, changing from nanoparticles to nanoclusters, then to single/dual-atom scale, plays a critical role in the nanomaterials' physicochemical properties. Pd nanocluster could provide extra active sites based on the transition metal catalysts. Xiaoqian Wei *et al*. [53] utilized the electronic interaction between Pd nanoclusters and Fe single atoms, triggering the Fe single atom's spin-state to intermediate spin. The change of spin state enhanced ORR dissociative pathway and improved the catalytic activity. This atomic-scale mechanism study provided researchers with new insights into the spin-regulation strategy. H. Cruz-Martı´nez *et al*. [54] applied auxiliary density functional theory to study the ORR activity of the Pd-based core-shell clusters, including Pd nanoclusters, M@Pd bimetallic nanoclusters, and M@PdPt trimetallic nanoclusters. Researchers computed the adsorption energies of some intermediates (O, OH) as predictors to evaluate the ORR activity and investigated the catalytic trends of these Pd-based nanoclusters. From the theoretical viewpoint, the conclusion of the activity trends was $M_6@Pd_{30}Pt_8$ > $M_6@Pd_{38}$ > Pd_{44} and the stability of these nanoclusters was further studied in a vacuum and an oxidizing environment.

To maximize the utilization of precious metals, fabricating single-atom catalysts (SACs) is an efficient method to fully make use of the active sites and achieve 100% atom efficiency [55]. In the traditional bulk Pd materials, waste of inner precious metals largely increases the cost, while the palladium single atoms supported on some carbon materials could maximize the benefits. Hee-Eun Kim *et al*. [56] synthesized Pd single atoms supported on the graphitic carbon nitride with carbon black and this catalyst showed high activity and selectivity towards two-electron transfer ORR. Due to the rich N-anchoring sites in the carbon nitrate, researchers used the quite simple impregnation method to immobilize the Pd single atoms into the sites without forming Pd

nanoparticles. This work showed the advantages of SACs: low cost, simple synthesis, high activity, high selectivity, and many studies confirmed these features. Nan Wang *et al*. [55] synthesized Pd-doped zeolitic imidazolate framework material for H_2O_2 generation (**Figure 3c**). Similar to the Pd single atoms immobilized on the graphitic carbon material, this catalyst is also N-coordinated single-atom Pd material. According to DFT calculation, the researcher pointed out that the Pd single-atom sites in the form of Pd-N_4 preferred breaking the bonds between oxygen atoms and active sites, resulting in the high selectivity of two-electron transfer during the ORR process. The fabrication of SACs depends on different transition metals as active sites and various carbon materials as the conductive supporting base. Kun Jiang *et al*. [57] fabricated the transition metal single atoms immobilized on the carbon nanotubes and achieved a flexible control towards oxygen reduction pathways. The transition metal SACs in the work like Fe-C-O single atom catalysts tuned the product selectivity and brought inspiration and guidance towards other metals like Pd. Similar to N-coordinated Pd SACs, some researchers focused on carbon-coordinated SACs, like defect graphene. Zengxi Wei *et al*. [58] found new Pd SACs (C_4Pd) and analyzed the mechanism for high activity and selectivity for two-electron transfer to produce H_2O_2 (**Figure 3d**). As a reference, they also fabricated Pd clusters immobilized on the defect graphene with the formula C_4Pd_x (x = 2, 3, 4, 5), which exhibited worse performance than the single atom catalyst (**Figure 3e**). Considering the multifunctional feature, SACs are still competitive. In order to find the trifunctional catalysts for ORR, OER, and HER, Zhanzhao Fu *et al*. [59] took advantage of single-layer Ti_3C_2 and fabricated Pd SACs on the $Ti_3C_2O_2$ (**Figure 3b**). The combination of Ti_3C_2's intrinsic high activity for HER and traditional ORR and OER active center of the Pd metal successfully constructed the highly active trifunctional catalyst $Pd_1@Ti_3C_2O_2$. The interaction between these two parts could change the d-band center of Pd atoms to an optimal position and improve the catalytic performance. As for stability, the study demonstrated that the aggregation of Pd single atoms into small clusters could not influence the activity.

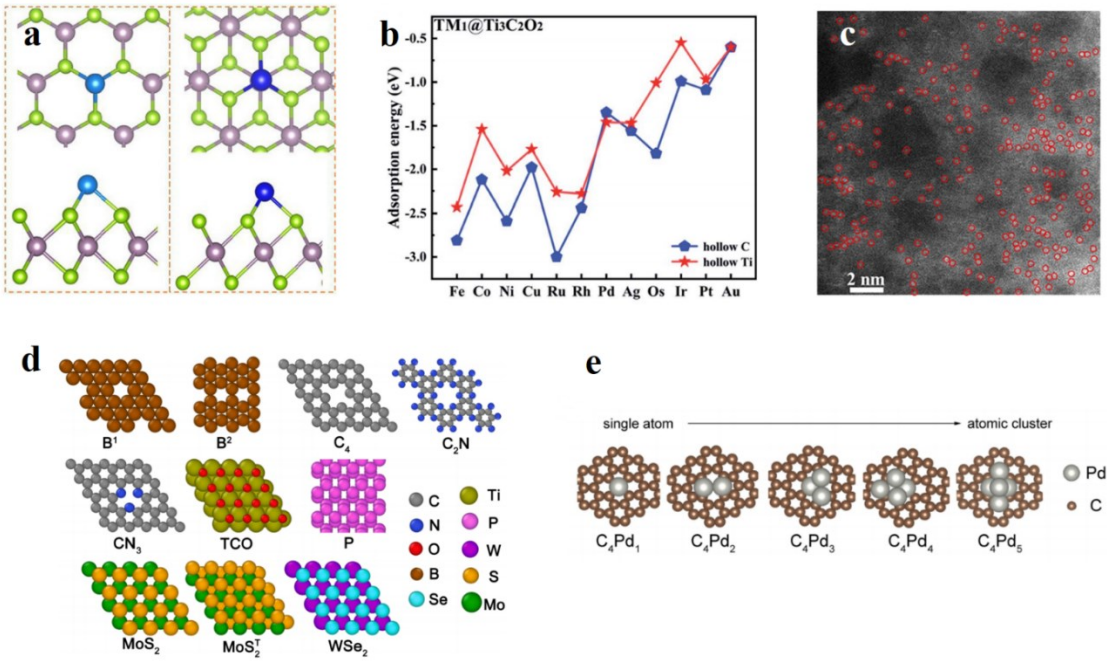

Figure 3. (a) The obtained lowest-energy configurations for single TM atom anchored on 2H– and 1 T-$MoSe_2$ monolayer. Reproduced with permission. [60] Copyright 2022, Elsevier. (b) Adsorption energies of different TM atoms on hollow Ti (red stars) and hollow C (blue pentagons) sites of $Ti_3C_2O_2$. Reproduced with permission. [59] Copyright 2020, Royal Society of Chemistry. (c) Structural characterization for $Pd_{0.157}$-NC, showing the configuration of Pd single atoms in Pd-NC. Reproduced with permission. [55] Copyright 2022, American Chemical Society. (d) Proposed 2D materials with different binding environments (B, C, N, O, P, S, Se) for one single Pd atom. Reproduced with permission. [58] Copyright 2022, Elsevier. (e) Optimized structures of C_4Pd_x (x = 1, 2, 3, 4, 5). Reproduced with permission. [58] Copyright 2022, Elsevier.

Except for using one kind of transition metal as the active sites, distributing two or more kinds of elements as single atoms into carbon materials is also a feasible strategy. Matthew T. Darby *et al*. [61] reported the single-atom alloys (SAAs) for ORR electrocatalysis. Through DFT calculations, the SAAs exhibited excellent activity and durability like high tolerance to CO poisoning due to the C-C coupling and C-H activation reactions. Among 10 kinds of SAAs, the doped metals like Pd, Pt, and Rh largely improved the activity of the host metals like Au and Ag, demonstrating the

SAAs enhanced ORR performance over corresponding monometallic SACs.

Transition metal dichalcogenide (TMD) nanosheets provide new ideas for the choice of supporting 2D nanostructures. The TMD nanosheets are promising for anchoring metal single atoms due to their low cost and good stability. Zengming Qin *et al*. [60] stabilized various transition metals on the TMD $MoSe_2$ (**Figure 3a**) and compared their overpotentials during the ORR and OER processes (**Figure 7b**). The Ni@1T-$MoSe_2$ had the lowest OER overpotential while the Pd@1T-$MoSe_2$ performed best comprehensively.

Dual-atom catalyst is also promising for high atom-utilization efficiency [62,63]. Compared with single-atom catalysts, it could supply more active sites for reactants and intermediates, especially some necessary bridge adsorption. Xuewei Wang *et al*. [64] engineered both single-Pd-site catalysts and dual-Pd-site catalysts with different coordination environments and compared the adsorption characteristics. Specifically, researchers tried C, B, and N as coordination environments, and tested the influences on the adsorption of the reactant (O_2) and intermediates. The results showed that the removal of *OH should be the potential determining step for B coordination environment, while the formation of *OOH should be the potential determining step for C and N coordination environments. From the perspective of mechanism, Pd_2B_6/C material could facilitate the O=O cleavage, thus enhancing both associative and dissociative pathways.

1.3.1.3 Functionalized composite design

Functionalized hybrid materials composed of the metals and other materials like carbide, nitrate, polymers are promising for electrocatalysis due to the simple synthesis routes and relatively low cost [65,66]. Researchers could design the morphology of different materials separately and think about the combination strategy, thus fully utilizing the advantages of the hybrid materials' different parts and their interactions. Recently, Hongjing Wang *et al*. [67] prepared polyaniline-functionalized porous Pd metallene

(**Figure 4a**) and used it for a long-term ORR test. The ultrathin porous Pd nanosheets could provide extensive catalytic active sites due to the high ratio of the surface area to the bulk volume, while the polyaniline could provide high conductivity, excellent hydrophilicity, and relatively good stability. As mentioned above, the interactions between different parts of hybrid materials could be beneficial to the whole catalytic performance (**Figure 4b**). The results revealed that the π-conjugated ligand in the polyaniline would modify the d-band center and electronic structure. To investigate the specific function of polyaniline in the Pd-based nanocomposites, Mphoma S. Matseke *et al*. [68] synthesized Pd/PANI/C (carbon black) composite materials for electrocatalytic ORR. According to the TEM images, the sample with polyaniline showed more even distribution of the Pd nanoparticles on the surface than the traditional Pd/Carbon Black catalysts. The stability test demonstrated that the incorporation of polyaniline could improve durability due to the alleviation of the Pd nanoparticles' agglomerations. Besides, the properties of polyaniline have been studied comprehensively like the relationship between the catalytic activity and the thickness of polyaniline shell [69]. Researchers broaden their horizons towards extensive carbon material supports. To utilize the nitrogen-doped reduced graphene oxide, Ammara Ejaz *et al*. [70] reported an efficient method to fabricate the Pd @ nitrogen-doped reduced graphene oxide nanocomposite, with various inner interactions among the nitrogen, oxygenated functionalities of graphene oxide and Pd nanoparticles. Due to the complex coordination environment of the nitrogen, researchers investigated the distinct role of pyrrolic, pyridinic, and graphitic nitrogen. The results showed that the type of nitrogen influenced the size and distribution of the Pd nanoparticles.

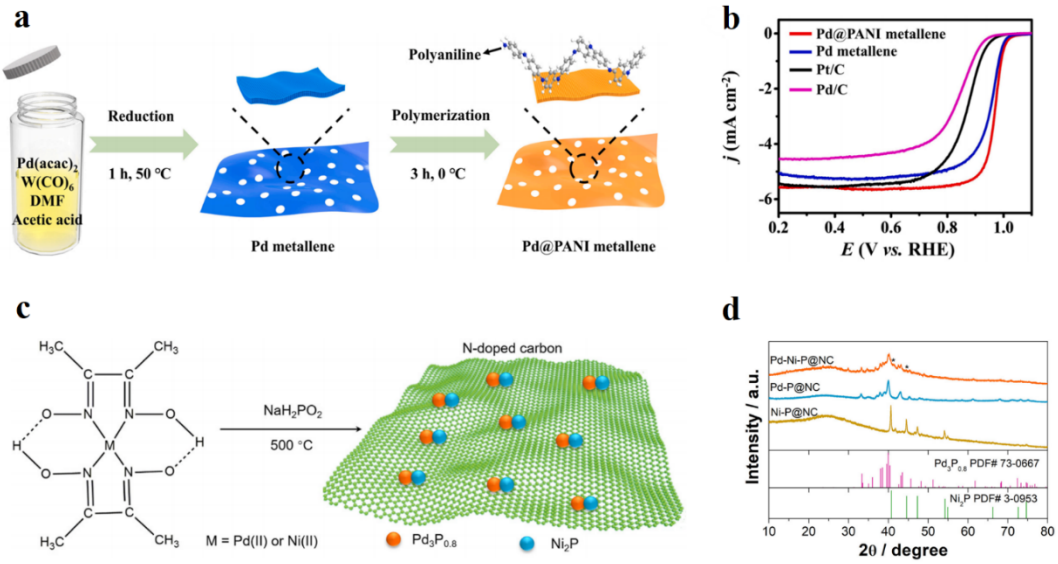

Figure 4. (a) The synthetic scheme of Pd@PANI metallene. Reproduced with permission. [67] Copyright 2022, Elsevier. (b) ORR polarization curves in an O_2-saturated 0.1 M KOH solution with a rotation rate of 1600 rpm at a scan speed of 10 mV s^{-1}. Reproduced with permission. [67] Copyright 2022, Elsevier. (c) Schematic illustration for the synthesis of Pd–Ni–P@NC by reacting Pd(II)/Ni(II)-dimethylglyoxime with NaH_2PO_2. Reproduced with permission. [71] Copyright 2019, Elsevier. (d) XRD patterns of Ni–P@NC, Pd–P@NC, and Pd–Ni–P@NC. Reproduced with permission. [71] Copyright 2019, Elsevier.

Metal phosphide is another choice because of the high mass activity and specific activity, resulting from the enhanced charge transfer and electronic modification [72]. Xue Dong *et al*. [71] studied the bimetallic phosphide supported on the nitrogen-doped carbon material and investigated the effects of the interfacial coupling interaction of metal phosphides (**Figure 4c**, **d**). The incorporation of the palladium phosphide and the nickel phosphide performed synergistic effects which optimized the electronic structure. By using dimethylglyoxime, the nitrogen-doped carbon material was easily synthesized during the pyrolysis while the phosphating process occurred in the same step.

1.3.1.4 Hybrid material design strategies

Alloying is an excellent strategy for efficient and durable catalysts of OER. Zafar Khan Ghouri *et al*. [73] synthesized PdCe alloy nanoparticles supported on the carbon nanowires for OER (**Figure 5a**, **b**). Due to a large number of active sites and low charge transfer resistance, the cooperative effect of bimetallic nanoparticles improved the catalytic activity and selectivity (**Figure 5c**) [73]. In addition, this kind of cooperative effect could enhance the chemisorption efficiency of oxygen-containing species and the 3D structure of the nanowires could improve the electrochemical surface area. The palladium in the catalyst could offer active centers by an electron inductive effect. Tao Zhang *et al*. [74] tuned the nanostructure of Ir-Pd alloy with three shapes, including hollow spheres, wires, and tetrahedrons, and investigated the OER performance of these nanoparticles (**Figure 5e**). Among the three microstructures, the nanowires and nanotetrahedrons exhibited excellent OER performance whose mass activity was five times that of the commercial Ir/C catalyst. Palladium oxide-based nanomaterials also exhibit large potential towards OER. Gabriel M.S. Salvador *et al*. [75] replaced Mn^{3+} of α-MnO_2 by Pd^{4+} due to the similar radius of Mn^{3+} and Pd^{4+}, and synthesized Pd/α-MnO_2 for OER (**Figure 5d**). The PdO on the surface of the catalysts provided active sites and enhanced the overall OER performance compared with pure α-MnO_2, indicating the successful Pd-doping strategy.

Composite nanomaterials are promising for enhancing OER performance [76]. The design of nanocomposite materials has been widely developed, including core-shell structure-based nanocomposites, multidimensional nanocomposites consisting of 3D and 2D blocks [77], *etc*. Jiahui Kang *et al*. [78] designed a quite complex nanomaterial named "Pd nanoparticle-interspersed nickel cobalt hydroxide carbonate nanothorn-coated copper hydroxide nanotube arrays grown on a copper foam" and it exhibited quite high OER performance due to the large surface areas, the increased number of active sites and the fast electron and mass transfer (**Figure 5f**). This Pd nanoparticle and core-shell carbon composite material possessed the interfacial interaction resulting

in an optimized electronic structure, leading to enhanced OER activity.

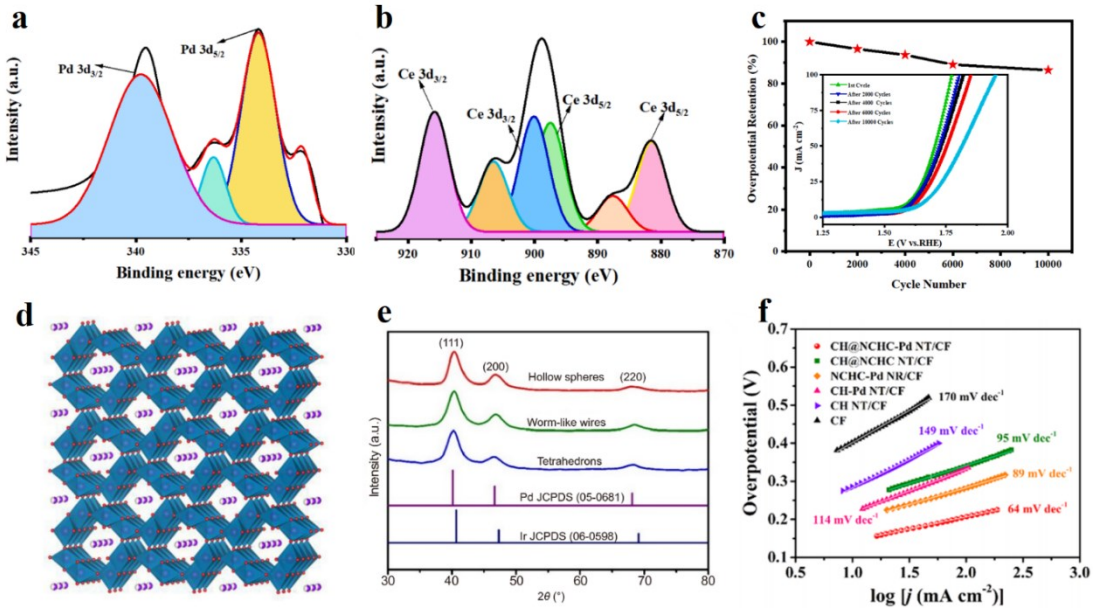

Figure 5. (a) XPS Pd 3d spectra; b) XPS Ce3d spectra for synthesized PdCe/CNWs nanocomposite. Reproduced with permission. [73] Copyright 2022, Elsevier. (c) Overpotential retention as a function of LSV cycle number and (inset) corresponding LSV cycles for synthesized PdCe/CNWs electrodes. Reproduced with permission. [73] Copyright 2022, Elsevier. (d) Framework lattice crystal structure of α-MnO_2. Reproduced with permission. [75] Copyright 2021, Elsevier. (e) XRD patterns of as-synthesized Ir-Pd alloy nanocrystals. Reproduced with permission. [74] Copyright 2018, Springer Nature. (f) Tafel plots of the developed catalysts in 1 M KOH. Reproduced with permission. [78] Copyright 2019, American Chemical Society.

1.3.1.5 Multifunctional OER/ORR catalyst design

The demand for bifunctional electrocatalysts for OER and ORR largely increases with the development of rechargeable metal-air batteries like zinc-air batteries [79-81]. However, it is hard to possess both excellent OER and ORR catalytic activity at the same time. For example, Pt/C is the commercial catalyst applied in ORR, while RuO_2 and IrO_2 are recognized as the best catalysts for OER, but they can only serve as single functional catalysts [82]. As a substitute for Pt metal, many Pd-based catalysts are

developed for ORR. Due to the oxide materials' promising activity towards OER, designing the Pd metal oxide catalysts or Pd-based transition-metal oxides can be a hopeful way to develop bifunctional electrocatalysts. Hong-Chao Li *et al*. [9] applied a two-step carbonization strategy based on Pd-incorporated ZIF material to form structural nanocubes (**Figure 6c**). This catalyst showed a better catalytic performance of OER and ORR than the commercial RuO_2 and the commercial Pt/C, respectively. In the OER working environment, CoOOH formed on the surface of the nanocubes, preventing further oxidation of the whole materials, and serving as OER active sites simultaneously (**Figure 7a**). To increase the electronic conductivity, researchers chose to make the conducting carbon materials derived from ZIF as the base and also maintained the porous morphology of the initial framework. Jia-Xing Guo *et al*. [83] comprehensively studied the bifunctional catalysis of the single precious metals (including Pd, Pt, and Ir) anchored on the Janus MoSSe monolayers (**Figure 6b**). According to the analysis of the reaction mechanism, the intermediate form, and the adsorption behaviors, the Pd and Pt single atom samples exhibited better OER and ORR activity compared with the Ir one. Researchers pointed out that the built-in electric field of the Janus MoSSe monolayer structure could be one of the reasons for the excellent OER performance. Xiaomeng Liu *et al*. [84] prepared heterostructured Pd/Pd_4S supported on the hollow carbon spheres for efficient bifunctional electrocatalysis (**Figure 6d**). The porous morphology provided an extremely large surface area and abundant transportation channels for reactants and intermediates, while the interfacial engineering of Pd/Pd_4S provided excellent intrinsic catalytic activity. The synergistic effect of the two parts enhanced the catalytic performance and the application for the lithium oxygen battery showed pretty good specific capacities. Mi Young Oh *et al*. [85] aimed to use Pd-based perovskite oxide materials to fabricate the lithium oxygen battery and synthesized the nanostructured La(Sr)Fe(Co)$O_{3-\delta}$@Pd matrix (**Figure 6a**). The combination of Pd nanoparticles' ORR activity and perovskite oxides' OER activity enabled the superior charge-discharge capacity and cycling performance of the lithium oxygen battery.

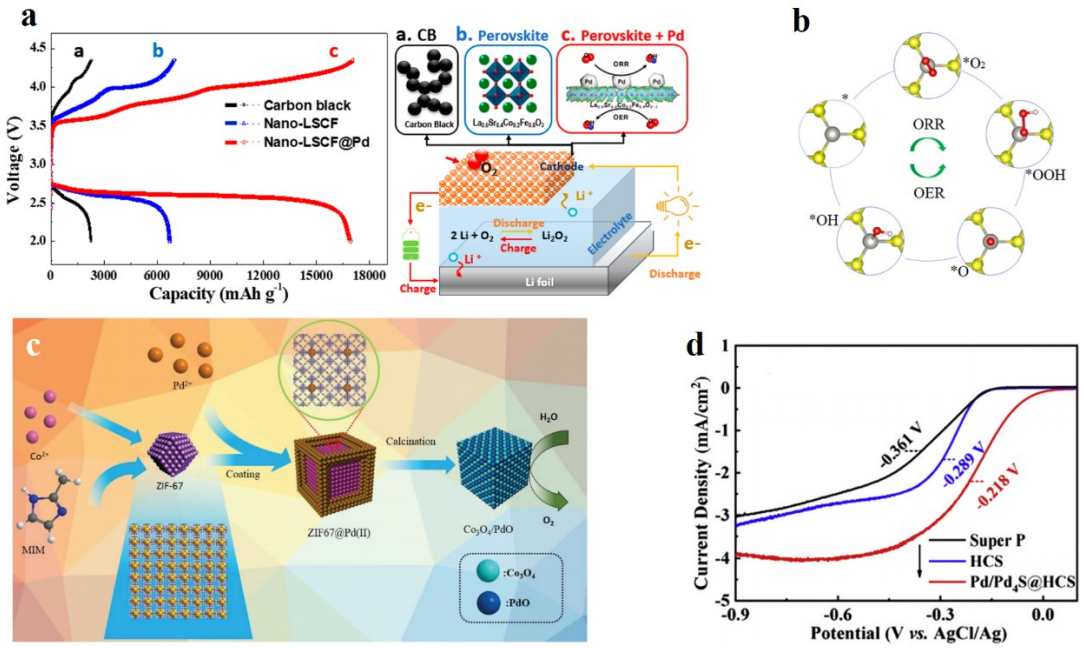

Figure 6. (a) Electrochemical performances of Li−O_2 batteries: the initial discharge profiles of a) carbon black, b) Nano-LSCF, and c) Nano LSCF@Pd as air cathode materials in the potential range of 2.0−4.35 V vs Li/Li^+ at a current density of 200 mA g^{-1}. Schematic illustration comparing different cathode catalysts: a) carbon black, b) Nano-LSCF, and c) Nano-LSCF@Pd (right). Reproduced with permission. [85] Copyright 2019, American Chemical Society. (b) Reaction schemes of ORR and OER processes on Pd- and Pt-MoSSe. Reproduced with permission. [83] Copyright 2022, Elsevier. (c) Schematic illustration of the synthesis of the Pd@PdO–Co_3O_4 nanocubes. Reproduced with permission. [9] Copyright 2018, John Wiley and Sons. (d) LSV curves for ORR of Super P, HCS, Pd/Pd_4S@HCS. Reproduced with permission. [84] Copyright 2021, Elsevier.

1.3.1.6 Multifunctional OER/HER catalyst design

Water-splitting bifunctional electrocatalysts also attracts researchers' attention [86,87]. Among numerous catalysts, MOF-based materials are desirable multifunctional electrocatalysts due to the intrinsic properties of well-defined compositions, tunable morphology, porous structures, and high surface area [88]. Adewale K. Ipadeola *et al*. [89] developed bimetallic Pd/Ni nanocrystals on MOF-derived carbon materials for

water-splitting, including OER and HER electrocatalysis (**Figure 7c**). The researchers treated the MOF template with chemical etching and compared the sample with and without the etching process. The results showed that the untreated sample performed better due to the superior conductivity. MOF-derived carbon materials have promising properties towards high catalytic activity resulting from the tunable porosity and high surface area. The metal oxides have pretty good intrinsic OER activity and based on it, Papri Mondal *et al*. [90] studied the metal permanganate materials. After the compositing and doping process, researchers fabricated silver permanganate modified by both metallic and oxidized Pd (Pd^0 and $Pd^{\delta+}$). Attributed to the synergistic effect of the different parts of the nanocomposites (i.e., silver permanganate, metallic Pd, oxidized Pd), the adsorption ability, charge transport, and long-term durability improved remarkably (**Figure 7d**). Researchers also investigated the influence of oxidation states of oxidized Pd species on the bifunctional catalytic properties and the mixed-valence Pd performed best. Xiao Zhang *et al*. [91] developed the bimetallic nanoparticles doped in carbon nanotubes for trifunctional (OER, HER, ORR) electrocatalysis. According to the calcination and reducing agent treatment, researchers immobilized the Ni and Pd nanoparticles into the CNTs with sizes of 1 nm and 2-5 nm, respectively. This accurate control of the size and distribution of the metal nanoparticles successfully enhanced the catalytic activity under the acidic medium.

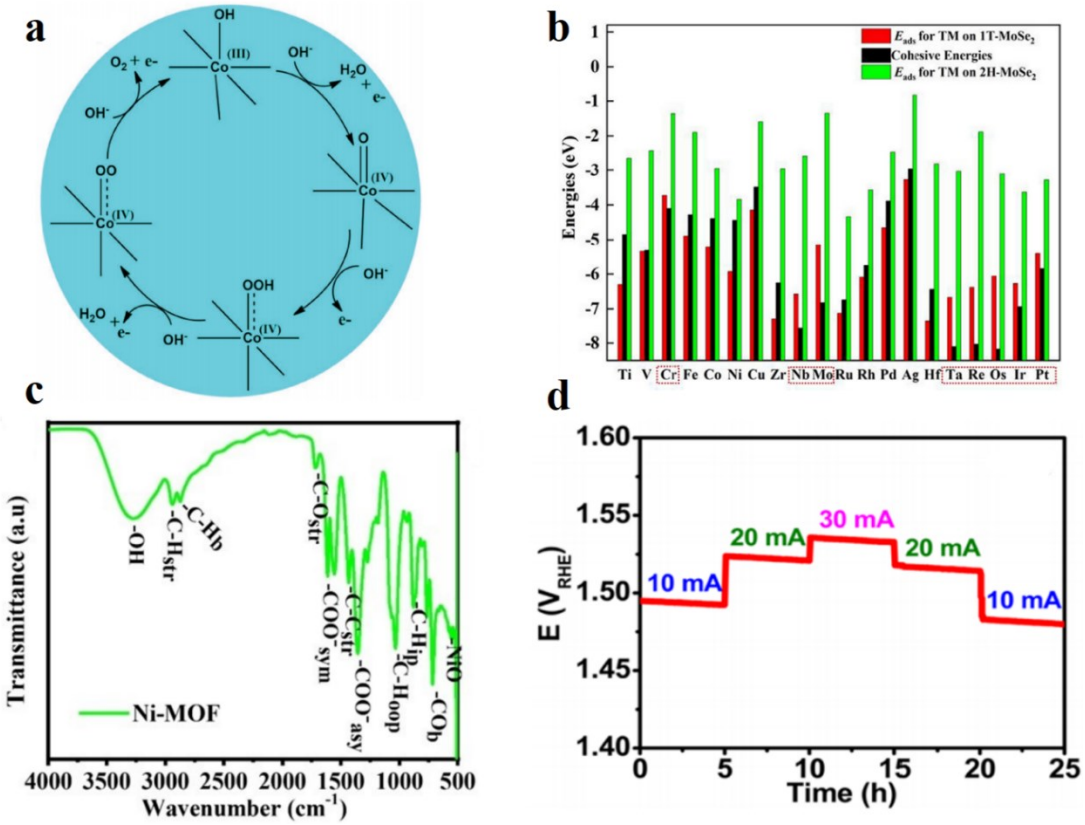

Figure 7. (a) Catalytic cycle of Co during the water oxidation process. Reproduced with permission. [9] Copyright 2018, John Wiley and Sons. (b) Adsorption energies (E_{ads}) and cohesive energies for single TM atom anchored on 2H- and 1 T-$MoSe_2$ monolayer. Reproduced with permission. [60] Copyright 2022, Elsevier. (c) FTIR spectra of Ni-MOF. Reproduced with permission. [89] Copyright 2020, John Wiley and Sons. (d) Chronopotentiometric stability measurements of the NComp-3-based electrolyzer for 25 h. Reproduced with permission. [90] Copyright 2021, American Chemical Society.

1.3.1.7 Interface engineering

Interface engineering is a good method to provide more highly active reaction sites for hydrogen evolution reaction and enhance performance [92]. Palladium nanoparticles could serve as active sites on the surface of HER electrocatalysts. Yang-Yi Liu *et al*. [92] constructed perfect interfaces between Pd-Ag and carbon/nitrogen materials C/N

by controlling the fabricating temperature and successfully synthesized the Pd-doped core-shell nanowire structure (**Figure 8a**). This interface controlling strategy could provide more active sites on the surface and enhance adsorbing, activating, and converting the reactants, intermediates to the products. Following this initial idea, the researchers chose the noble metal alloy-carbon material interface system. Based on the ratio adjustment of Pd and Ag, the catalysts exhibited extremely high performance with a low Tafel slope of 64 mV per decade. Except for the 3D nanostructure, the 2D nanosheet-based interface is also a good choice. Jin Li *et al*. [93] atomically dispersed Pd on the MoO_3 nanosheets to form the Pd@MoO_3 heterostructure and interface (**Figure 9a**, **b**). This catalyst performed very well in the acidic medium with quite a low overpotential and Tafel slope value. The well-designed interface enhanced ion/electron transfer on the surface and increased the catalytic rate. Based on the self-assembly-directed synthesis method, the researcher achieved the fabrication of an efficient and large-size electrocatalyst.

1.3.1.8 Morphology design

Morphology design is another promising strategy to design catalysts. To increase the number of active sites and lower the costs, Daniel Ohm *et al*. [94] used the nano-confining strategy to grow some atomically dispersed Pd/Ir islands on the Au(111) and optimized the HER performance by controlling the morphology, density, and size of the islands (**Figure 8e**). Based on the Cu underpotential deposition and galvanic displacement, the researchers deposited the sublayers on the surface of Au and then successfully fabricated the discrete islands of Pd/Ir. By controlling the deposition process of Cu, researchers could shape the islands as the designed morphology. Balasingh *et al*. [95] also used the galvanic replacement method to synthesize distinct nanostructures. The researchers developed a facile route to fabricate the carbon-supported porous Pd core with Pt enriched shell surface. The prepared PdPt/C nanocrystals had high crystallinity thus exhibiting super good stability and providing a

feasible way to synthesize the bimetallic catalysts.

Core-shell structures are widely studied with different elements. Yihe Wang *et al*. [25] fabricated the Pd/Pt core-shell nanostructure and adjusted the shell layers by the etching method (**Figure 8c**). These hollow nanocages could increase the atom utilization efficiency of both noble metals and the bilayer nanocages performed better than monolayer ones. It's worth noting that the activity improvement of this bilayer thin wall was more than twice that of the monolayer one. To further reduce the cost of fabrication, constructing a core-shell structure with some less expensive transition metals like Cu could be a feasible way. Jing Li *et al*. [96] reduced $Cu(acac)_2$ and Na_2PdCl_4 to synthesize PdCu alloy nanocubes and dealt with electrochemical reactions to fabricate core@shell PdCu@Pd nanocubes by etching the surface Cu to enhance the overall HER activity. According to weakening the binding energy of the intermediates and exposure of more Pd active sites on the surface. Compared with the original PdCu alloy nanocubes, this core-shell structure brought a Pt-like performance and much greater stability. To further decrease the content of noble metals for low-cost electrocatalysts, fabricating bimetallic catalysts with large amounts of non-noble metals is a feasible way. However, balancing the stability of this kind of catalyst and the super low loading of noble metals is quite difficult. To find out the optimal solution for this problem, Xiaocheng Liu *et al*. [97] synthesized nanoporous NiPd/metallic glass and minimized the Pd loading in the alloys by implementing the dealloying method and galvanic replacement to load Pd on the surface.

To fabricate durable and active HER electrocatalysts, Uroš *et al*. [98] deposited Pd nanoparticles on the surface of TiO_2 nanotube arrays via a galvanic displacement strategy. The Pd content fills the entire tube walls with the matching length. The semiconductor properties of the TiO_2 nanotube and interactive Pd active sites provided optimized atomic hydrogen binding energy, thus boosting the HER activity. The 3D TiO_2 nanotube not only supported a large amount of Pd nanoparticles but also prevented degradation of the Pd active sites, enhancing the electrocatalytic durability under harsh working environments.

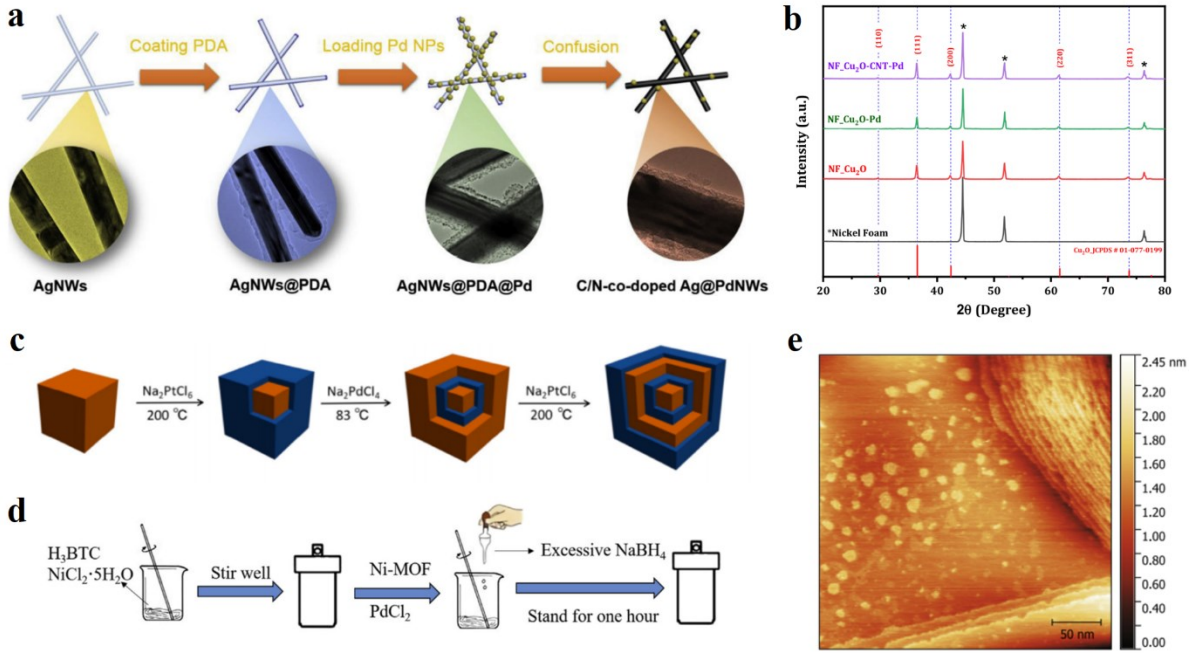

Figure 8. (a) Schematic illustration of the preparation of the C/N-co-doped Ag@Pd NWs. Reproduced with permission. [92] Copyright 2018, Elsevier. (b) X-Ray Diffraction patterns of NF_Cu_2O, NF_Cu_2O-Pd, and NF_Cu_2O-CNT-Pd samples. Reproduced with permission. [99] Copyright 2021, Elsevier. (c) Schematic illustration of the transformation from cubic Pd to the final Pd-Pt tripleshelled nanocube via layer-by-layer epitaxial approach. Blue = Pt, Brown = Pd. Reproduced with permission. [25] Copyright 2019, Springer Nature. (d) Schematic for the preparation of Pd/Ni alloy. Reproduced with permission. [100] Copyright 2020, Elsevier. (e) Example STM image of Au(111) surface after Pd displacement of Cu UPD (10 s UPD duration at 0.47 V vs SHE). Reproduced with permission. [94] Copyright 2021, Elsevier.

1.3.1.9 Modification strategy

Pd-based modification is a cost-efficient strategy for electrocatalysis, which improves the electrocatalytic performance according to surface modification of Pd-containing molecules [99]. Vishal Burungale *et al*. [99] fabricated the Pd/CNT modified Cu_2O/NF by spraying method to deal with the sluggish reaction kinetics of HER (**Figure 8b**). Compared with the pure Cu_2O/NF, the presence of Pd improved the catalytic activity

while the CNT part on the surface could largely enhance the charge transportation and conductivity (**Figure 9c**). The surface modification also provided porous structures and enhanced the dispersivity of Pd nanoparticles. Besides, noble metals like Pd are beneficial for the overall conductivity and activity of the catalysts.

Due to the poor conductivity of MOF-based materials, researchers modified these materials with some metal nanoparticles. Ming Nie *et al*. [101] took advantage of the Pd nanoparticles to enhance the electrical conduction of MOF materials for high-performance HER. According to the direct reduction method, researchers prepared the Pd/MOF materials and the synergistic effect of the improved specific surface area and conductivity enlarged the electrocatalytic activity. M. Nie *et al*. [100] reported the fabrication of the Pd-doped Ni-MOF materials for the high conductivity and stable three-dimensional HER catalyst (**Figure 8d**). To further improve the performance, researchers investigated the effect of different content ratios of Pd to Ni and found that this adjustment could reduce the resistance charge transfer (**Figure 9d**). The pore structure and adsorption ability derived from MOF structures, combined with the excellent electron transfer ability and highly active sites from the modified Pd nanoparticles, resulted in a super good performance.

In addition to MOF materials, other three-dimensional carbon materials also could be functionalized by noble metals to fabricate electrocatalysts. Jie-Yu Yue *et al*. [102] constructed Pd ions supported on the covalent organic frameworks (COF) materials for the HER application. This work developed the first Pd^{2+}/COF system for the HER electrocatalysis and the performance results indicated that the vinylene-linked COF platforms without a pyrolysis-free process could be a new design idea (**Figure 9e**). Due to the ordered crystalline porous structure linked by covalent bonds, the COF-based materials could be highly stable. Besides, the carbon-carbon double bonds derived from the vinylene adjusted the electronic structure and increased the surface areas. Therefore, the combination of Pd active sites and this COF structure enhanced the whole catalytic performance and durability. Chao Shu *et al*. [103] used the hydrothermal method to synthesize the low-loading Pd on the hollow titanium dioxide sphere and the Pd doping

effect could provide more active sites, resulting in the promoted catalytic performance. Utilizing the synergistic effect of Pd-based alloy as a modifier is also a promising strategy to fabricate cost-efficient electrocatalysts. Milutin Smiljanic *et al*. [104] deposited the Pd/Rh nanoislands on the polycrystalline gold electrode and compared it to Pd-polycrystalline gold, Rh-polycrystalline gold to investigate the synergistic effect of the tri-metallic catalyst. The results indicated that the strong interaction between these three metals lowered the adsorption energy of the intermediate during the HER process, thus enhancing the catalytic activity.

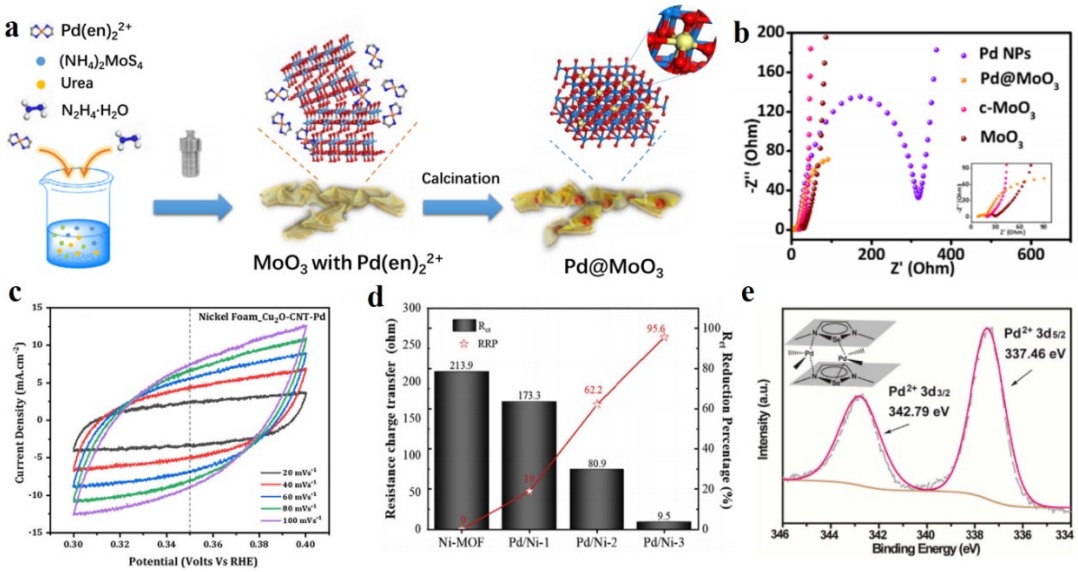

Figure 9. (a) Synthetic scheme of the Pd@MoO_3 heterostructure. Reproduced with permission. [93] Copyright 2019, American Chemical Society. (b) Nyquist plots of Pd@MoO_3, c-MoO_3, MoO_3, Pd NPs, and Pt/C. Reproduced with permission. [93] Copyright 2019, American Chemical Society. (c) Cyclic Voltammetry curves in a non-faradaic region at scan rates of 20, 40, 60, 80, and 100 mV/s for NF_Cu_2O-CNT-Pd samples. Reproduced with permission. [99] Copyright 2021, Elsevier. (d) Comparison of R_{ct} and reduction percentage based on Ni-MOF. Reproduced with permission. [100] Copyright 2020, Elsevier. (e) XPS spectra of Pd 3d in PY-SE–COF–Pd and inset was the possible Pd^{2+} coordination modes in PY-SE–COF–Pd. Reproduced with permission. [102] Copyright 2022, Elsevier.

1.3.2 Transition metal-based nanomaterials

1.3.2.1 Transition metal phosphides

Transition metal phosphides (TMP) and TMP-based materials have been widely investigated [31,35,36] and they have shown good electrocatalytic performance for HER, OER, and ORR. TMP exhibited superior catalytic activity in different fields including electrocatalysis, photocatalysis, diesel and gasoline desulfurization [39], *etc*. The triangular prism structure [39] of TMP endowed the material with rich chemical bonds like metallic and covalent bonds, numerous coordinated unsaturated surface atoms, and increased exposed active sites. Several strategies have been utilized to further improve the catalytic activity of TMP-based electrocatalysts, including adjusting the stoichiometric ratio of transition metal and P [31], alloying with different transition metals, hetero-atomic doping [105-108], morphology designing, *etc*. H. Liu *et al*. [109] developed a carbon dots-oriented method to construct a composite nanostructure consisting of fungus-like cobalt phosphide and nitrogen-doped carbon dots. **Figure 10a** shows the schematic illustration of the synthetic process, including a hydrothermal reaction to get CoCOH-NCDs/NF intermediate and the calcination process for phosphating. The synergistic effect and strong interactions between the fungus-like cobalt phosphide and nitrogen-doped carbon dots tuned the electronic structure of the composite material and largely improved the catalytic performance. **Figure 10b** shows the HER polarization curves and **Figure 10c** shows the corresponding Tafel plots, indicating that the experimental sample exhibited lower overpotential and larger Tafel slope compared to the counterparts, while the Pt/C still showed the most favorable HER activity. The catalysts achieved the low overpotentials of 103 mV for HER and 226 mV for OER at 10 mA cm^{-2} in 1.0 M KOH, and only required a cell voltage of 1.55 V to afford 10 mA cm^{-2}, showing excellent electrocatalytic performance of water splitting. **Figure 10d** shows the long-term electrochemical durability test, displaying good stability after 1000 cycles. G. Zhang *et*

al. [105] used a doping strategy to fabricate TMP-based nanomaterials for bifunctional electrocatalysis. Researchers tried different rare earth elements as doping agents and selected CoP as host materials to enhance electrocatalytic performance. As a result, the Er-doped ultrathin cobalt phosphide nanomeshes performed best among the various rare earth elements (Er, Nd, Ce, La, and Gd). This ultrathin nanomesh morphology largely increased the surface area and double-layer capacitance, thus providing more active sites. Besides, the modified electronic structure successfully optimized the hydrogen adsorption energy and enhanced the electrocatalytic activity. The Er-doped CoP catalyst achieved the low overpotentials of 66 mV for HER and 256 mV for OER at 10 mA cm^{-2} in alkaline medium, while it still exhibited excellent HER performance in acidic medium. The cost-efficient and operational water splitting electrolyzer has been fabricated by Er-doped CoP electrodes and it only required a cell voltage of 1.58 V to afford 10 mA cm^{-2} in alkaline medium. This study provides an appealing strategy to utilize doping method in TMP's design. Z. Lu *et al*. [110] designed complex heterogeneous nanostructure Co_2P/CoP@Co@NCNT to construct rich-interface catalysts. Researchers embedded metallic cobalt into nitrogen-doped carbon nanotubes (NCNT), which served as anchoring sites for carbon carrier. Then, they further embedded the heterogeneous Co_2P/CoP into the surface of the as-synthesized Co@NCNT. The synergistic effect of these three parts largely increased the interfacial active sites, accelerated electronic conductivity, and modulated the interfacial electronic structure. As a result of rich-interface construction, the catalyst required the ultralow overpotentials of 118 mV and 256 mV at 10 mA cm^{-2} in 1.0 M KOH for HER and OER, respectively. This rich-interface construction strategy brings new inspiration for facilitating the development of novel TMP electrocatalysts. Density functional theory (DFT) calculations revealed that the Gibbs free energy barrier of H* adsorption on Co_2P/CoP was smaller than Co_2P or CoP shown in **Figure 10e**, indicating enhanced HER kinetics. **Figure 10f** reveals that the rate-determining step (RDS) for Co_2P/CoP was the transformation from *O intermediate to *OOH intermediate. The electron transfer from CoP to Co_2P manifested the electron accumulation on Co_2P and the hole

accumulation on CoP, and this electron redistribution increased electrocatalytic activity. L. Ji *et al*. [111] took advantage interior volume of hollow structures and designed CoP nanoframes. Sufficient channels of this open structure provided a large number of active sites and avoided severe aggregation. This hollow structure improved the atom utilization efficiency, thus promoting electrocatalytic performance. J. Li *et al*. [112] fabricated multimetallic phosphide FeNi–Co_2P and investigated the OER and HER electrocatalytic performance of it. The different transition metals in the material largely improved intrinsic activity and the Fe incorporation increased the number of high-valence cobalt and nickel, leading to superior OER activity. It required the ultralow overpotentials of 225 mV at 10 mA cm^{-2} in 1.0 M KOH for OER. Tafel plots corresponding to the OER polarization curves displayed that the FeNi–Co_2P possessed the smallest Tafel slope value of 42.8 mA dec^{-1}, shown in **Figure 10g**. Compared to other Tafel slopes of 74.6 mV dec^{-1} (Ni–Co_3O_4), 47.3 mV dec^{-1} (FeNi–Co_3O_4), and 64.8 mV dec^{-1} (Ni–Co_2P), the small Tafel slope value indicated the fast reaction kinetics, large ramp rate of current densities against overpotentials, and exceptional catalytic performance. The electrochemical impedance spectroscopy (EIS) results demonstrated that the incorporation of Fe and the phosphating process reduced the charge transfer resistance. Besides, the disorder defects promoted the activation of the catalytic process. However, this trimetallic phosphide slightly decreased HER performance compared with Ni–Co_2P due to the low density of states. Therefore, researchers combined FeNi-Co_2P and Ni-Co_2P to fabricate the electrolyzer cell and it only required a cell voltage of 1.578 V to afford 10 mA cm^{-2}, providing a real-world application of renewable energy sources.

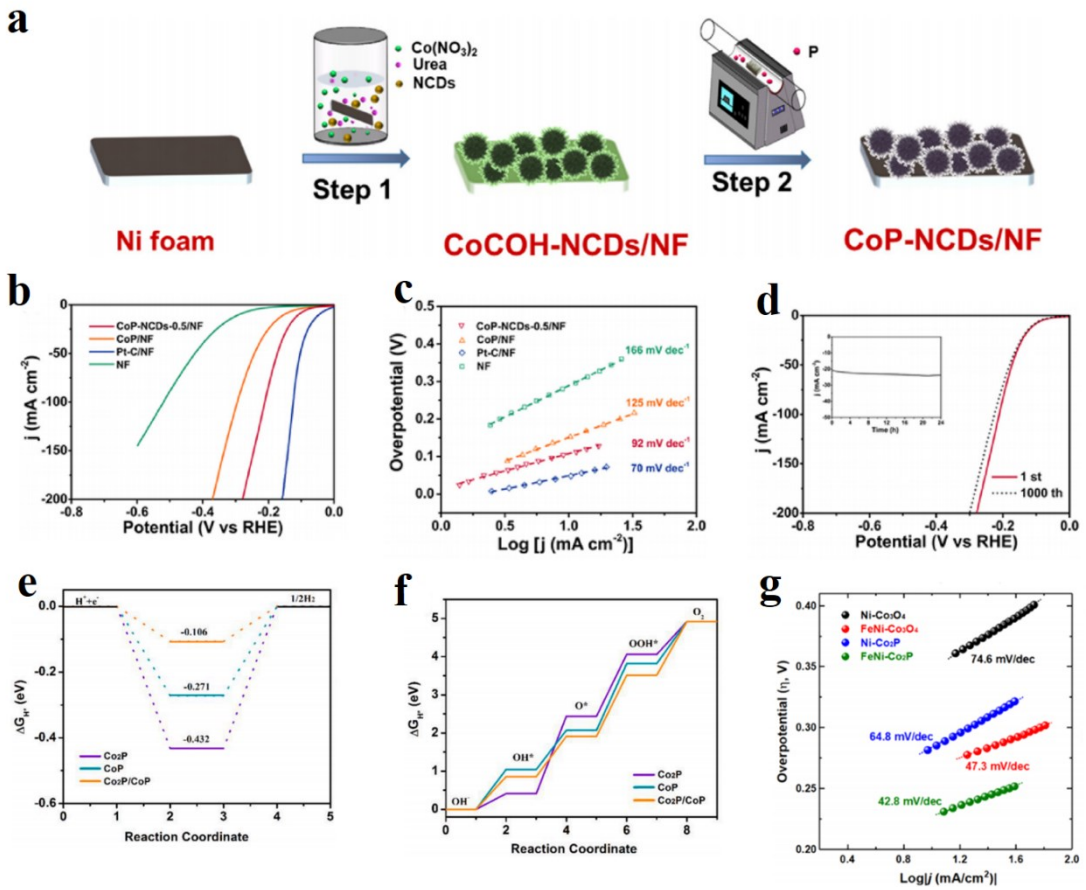

Figure 10. (a) Schematic illustration for the formation of CoP-NCDs/NF catalyst. Reproduced with permission. [109] Copyright 2021, Elsevier. (b) HER polarization curves of CoP-NCDs-0.5/NF, CoP/NF, bare Ni foam and Pt/C in 1.0 M KOH. Reproduced with permission. [109] Copyright 2021, Elsevier. (c) Tafel plots of CoP-NCDs-0.5/NF, CoP/NF, bare Ni foam and Pt/C in 1.0 M KOH. Reproduced with permission. [109] Copyright 2021, Elsevier. (d) Durability test for CoP-NCDs-0.5/NF in 1.0 M KOH before and after 1000 cycles; inset: long-term electrochemical durability of CoP-NCDs-0.5/NF for the HER for 24 h. Reproduced with permission. [109] Copyright 2021, Elsevier. (e) Calculated Gibbs free energy diagrams on bare Co_2P, CoP and Co_2P/CoP in 1 M KOH of H* adsorption during HER. Reproduced with permission. [110] Copyright 2022, Elsevier. (f) Calculated Gibbs free energy diagrams on bare Co_2P, CoP and Co_2P/CoP in 1 M KOH of intermediates *OH, *O, and *OOH adsorption during OER. Reproduced with permission. [110] Copyright 2022, Elsevier. (g) Tafel plots of Ni–Co_3O_4, FeNi–Co_3O_4, Ni–Co_2P, FeNi–Co_2P corresponding to OER polarization curves. Reproduced with permission. [112] Copyright 2021, American

Chemical Society.

Doping is an effective way for TMP-based materials' modification, and there are numerous doping agent choices such as metal doping and nonmetal doping. W. Li *et al*. [106] studied the mechanism of TMP's electrocatalysis and applied the doping strategy to enhance the water electrolysis. Researchers constructed Cr-doped cobalt phosphide nanoarrays to modulate the electronic structure of the material and applied it to pH-universal HER. The electron modulation could be verified by X-ray photoelectron spectroscopy (XPS) shown in **Figure 11a** and **Figure 11b**. The Co 2p high-resolution XPS spectra indicated that the negative peak shift could be attributed to electron density redistribution due to the doped Cr. This decreased positive charge of Co weakened the hydrogen adsorption on the active sites and reduced the energy barrier to form the intermediate. The positive peak shift of P 2p after Cr doping further verified the electron density redistribution and the enhanced charge transfer. The Cr-doped CoP required the ultralow overpotentials of 47 mV, 131 mV and 67 mV at 10 mA cm^{-2} for HER in 0.5 M H_2SO_4, neutral medium, and 1.0 M KOH, respectively. The mechanism study revealed that the M–P bonds changed from covalent bonds to ionic bonds in the early electrocatalysis stage, and then formed metal cations, which could serve as active centers for reactant adsorption and further transformation. The DFT calculation shown in **Figure 11c** demonstrated that the Gibbs free energy barriers for Co–Co bridge site and Co–Co top site in CoP were quite large, impeding the adsorption of hydrogen. After Cr doping, Gibbs free energy barriers for the bridge site and top site decreased, and the weakened hydrogen adsorption facilitated the electrocatalytic activity. J. Li *et al*. [107] used zeolitic imidazolate frameworks (ZIF) as a template to synthesize Ce-doped CoP by a phosphorization process. **Figure 11d** shows the SME image of Ce-doped ZIF-67, which displayed a uniform polyhedral morphology. **Figure 11e** shows the high-resolution transmission electron microscopy (HRTEM) image of the CoP products and the CoP (211) planes with a crystal lattice of 0.189 nm. The Ce incorporation applied electronic modulation, lowered the energy barrier of the potential-limiting step during

the electrocatalysis process, and optimized the adsorption of hydrogen on the materials' surface, thus accelerating the electron transfer and promoting the HER performance. According to the density functional theory (DFT) calculations, the adsorption and desorption energetics of the intermediate H* influenced the HER rate, and researchers have assessed the HER catalytic activity by the adsorption free energy of the intermediate H*, which has been reduced by the introduction of Ce, shown in **Figure 11f**. X. Q. Xie *et al*. [113] designed CoP/CNFs hierarchical structures with two-dimensional (2D) CoP nanosheets and one-dimensional (1D) carbon nanofibers (CNF). The nanocomposite 1D/2D structure provided a large number of active sites, accelerated electron and mass transfer during the electrocatalysis process, and facilitated the reaction kinetics. As a result, the optimized nanocomposite material required the ultralow overpotentials of 225 mV and 325 mV at 10 mA cm^{-2} in 1.0 M KOH for HER and OER, respectively. The electrolyzer assembled by CoP/CNFs was further evaluated for water splitting performance. **Figure 11g** shows the schematic illustration of CoP/CNFs/Ni foam||CoP/CNFs/Ni foam electrolyzer. The Linear sweep voltammetry (LSV) curves of the water splitting shown in **Figure 11h** disclosed that the CoP/CNFs exhibited superior catalytic activity compared to the bare Ni foam, and the stable performance shown in **Figure 11i** was obtained by chronoamperometric curve at an applied cell voltage of 1.65 V.

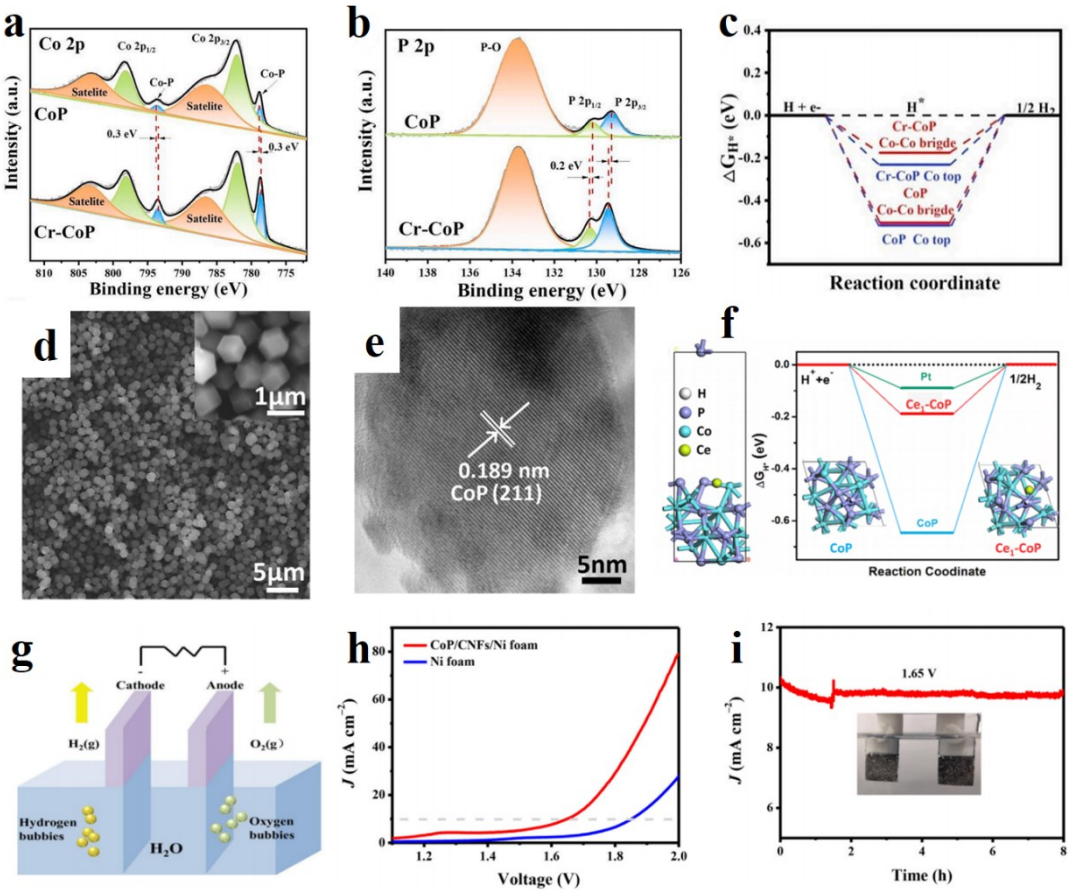

Figure 11. (a) Co 2p high-resolution XPS spectra of CoP and Cr-CoP. Reproduced with permission. [106] Copyright 2021, Elsevier. (b) P 2p high-resolution XPS spectra of CoP and Cr-CoP. Reproduced with permission. [106] Copyright 2021, Elsevier. (c) DFT calculations of hydrogen adsorption free energies. Reproduced with permission. [106] Copyright 2021, Elsevier. (d) Scanning electron microscope (SEM) image of 1% Ce-ZIF-67 (inset is the enlarged SEM image). Reproduced with permission. [107] Copyright 2020, American Chemical Society. (e) Morphological and structural characterization of HRTEM for Ce_1−CoP. Reproduced with permission. [107] Copyright 2020, American Chemical Society. (f) Atomic model and the DFT calculated results for HER on CoP and Ce_1−CoP. Reproduced with permission. [107] Copyright 2020, American Chemical Society. (g) Illustration of an electrolyzer for overall water splitting. Reproduced with permission. [113] Copyright 2022, Elsevier. (h) LSV curves of overall water splitting using CoP/CNFs/Ni foam||CoP/CNFs/Ni foam in 1.0 M KOH solution (scan rate: 5 mV s^{-1}). Reproduced with permission. [113] Copyright 2022,

Elsevier. (i) Chronoamperometric curve of water electrolysis at an applied potential of 1.65 V (catalyst loading ca. 0.68 mg cm^{-2}). Reproduced with permission. [113] Copyright 2022, Elsevier.

Framework-derived synthetic strategies make it possible to fabricate complex nanocomposites via facile synthetic steps. J. Liu *et al*. [114] used metal–organic framework (MOF) as a template to fabricate ultrathin cobalt phosphide nanosheets on the porous nanorods. The hierarchical structure endowed the material with a large surface area, short mass diffusion paths, boundary defects, and increased conductivity. The cobalt phosphide electrode has shown efficient catalytic activity with long-term durability. The fabricated real-world application for the overall water splitting exhibited excellent performance and the electrolyzer cell only required a cell voltage of 1.54 V to afford 10 mA cm^{-2}. J. Shi *et al*. [115] synthesized ZIF-derived CoP@FeCoP yolk-shell micro-polyhedra with nitrogen-doped carbon, which could largely decrease the agglomeration of CoP active sites and enhance long-term stability. The elemental mapping images shown in **Figure 12a** exhibited the uniform distribution of Co, P, Fe, N, C elements, and the Fe element mainly distributed in the outer shell. Besides, the complex structures increased the specific surface area and provided more active centers for electrocatalysis. Two parts of the material generated a synergistic effect which optimized the electronic structure and adjusted the adsorption energy. According to the energy band alignment diagram shown in **Figure 12c**, the electron could migrate from FeCoP/NC to CoP/NC, thus generating more active sites in the CoP/NC cores. B. Zhang *et al*. [116] engineered CoP@CoOOH core–shell heterojunction structure with rich oxygen vacancies to construct robust bifunctional HER/OER electrocatalysts. The anemone-like morphology and core–shell heterojunction structure strengthened the structural durability and prevented the agglomeration of the CoP active sites, while the oxygen vacancies in the materials reduced the energy barrier of rate determining steps. During the OER process, the structure of CoP@CoOOH transformed into CoOOH shown in **Figure 12b**. As-synthesized structure exhibited enhanced bifunctional

performance in both alkaline and neutral media, requiring the overpotentials of 89.6 mV and 81.7 mV for HER and 318 mV and 200 mV for OER at 10 mA cm^{-2} in neutral and alkaline media, respectively. DFT calculations shown in **Figure 12d** demonstrated that the rate-determining step of OER was the adsorption of *O, and the CoP@CoOOH successfully decreased the Gibbs free energy barrier of this rate-determining step from 1.84 V to 1.82 V. The oxygen vacancies reduced the Gibbs free energy barrier of *OOH intermediate to 1.67 V, further accelerating the reaction kinetics. G. Zhou *et al*. [117] implemented the heteroatom doping strategy to regulate the electronic structure of CoP nanosheets. Researchers incorporated oxygen into the CoP nanosheets and optimized the thermodynamics of the electrocatalytic reaction, thus accelerating the reaction kinetics. The modified adsorption free energy benefited the generation and transformation of the intermediates during the catalytic process. The anion-doping method boosted the catalytic performance of TMP and provided new inspiration for the electronic structure regulation strategy. Y. Sun *et al*. [41] applied a fluorination strategy to construct F-doped CoP nanoarrays on the copper foam. The F doping effect created a large number of P vacancies, resulting in amounts of active sites and better charge distribution. The simple fluorination step realized heteroatom doping, surface reconstruction, and vacancy engineering simultaneously. As-synthesized F-CoP showed low Tafel slopes of 32 mV dec^{-1} and 73.19 mV dec^{-1} for HER and OER, respectively. F. Zhang *et al*. [108] designed Ce-doping CoP/Ni_3P heterojunction structure to address the high intermediate energy barrier issue and accelerate the slow mass/charge transfer simultaneously. To confirm the crystal structure of Ce-CoP/Ni_3P, X-ray diffraction patterns (XRD) shown in **Figure 12e** were conducted. The hybrid CoP/Ni_3P and Ce-doping effect downshifted the d-band center to the Fermi level, optimized the local electronic structure and Gibbs free energy of hydrogen adsorption, and accelerated the product dissociation. Above properties endowed the Ce-CoP/Ni_3P electrocatalyst with high activity and superior pH-universality. The superior HER performance could be assessed by overpotentials shown in **Figure 12f**. The large electrochemical double-layer capacitance of Ce-CoP/Ni_3P shown in **Figure 12g**

indicated enlarged active area exposure. **Figure 12h** shows Tafel plots of the samples to describe the reaction kinetics, indicating that the Ce-doping and CoP/Ni_3P heterojunction decreased the Tafel slope values and accelerated the HER kinetics. To evaluate the stability of Ce-CoP/Ni_3P, the chronopotentiometry shown in **Figure 12i** displayed the long-term durability and the potential variations. The catalysts remained stable at the current densities of -100, -500, -1000 mA cm^{-2} for 200 h, exhibiting stable electrocatalysis at large-current-density. L. Li *et al*. [118] fabricated Mo-doped CoP nanomaterials and tuned different Mo/Co ratios to construct efficient and stable electrocatalysts for water splitting. Researchers used CoMo-layered double hydroxide (LDH) as the precursor and evenly dispersed the Mo atoms into the CoP lattice. As a result, the Co/Mo ratio of 1/2.3 exhibited the highest catalytic activity and durability, requiring the ultralow overpotentials of 118 mV and 317 mV at 10 mA cm^{-2} in 1.0 M KOH for HER and OER, respectively. This work developed a successful synthetic strategy by using LDH as the precursor for ultraeven doping. W. Gong *et al*. [119] utilized direct phosphorus-containing MOF pyrolysis to fabricate Co_2P/CoP embedded three-dimension N, P-doped graphite structure (denoted as Co_2P/CoP@NPGC) for ORR/OER electrocatalysis. By controlling the amount of P dopant, the crystalline phase of the product could be tuned. The 3D structure and Co_2P/CoP nanoparticles endowed as-obtained catalysts with fast mass/charge transfer and numerous active centers, respectively. Besides, the doping N and P in the graphite layer modified the electronic structure and promoted oxygen adsorption and dissociation on the surface. Y. Lin *et al*. [42] coupled CoP nanoparticles with defective carbon materials for bifunctional oxygen electrocatalysis. X-ray spectroscopic characterizations and theoretical calculations revealed that the defective carbon surface gathered electrons and the CoP surface gathered holes, thus constructing a strong interaction between these two parts. This interfacial polarization improved the ORR and OER catalytic activity by optimizing the interfacial electron distribution.

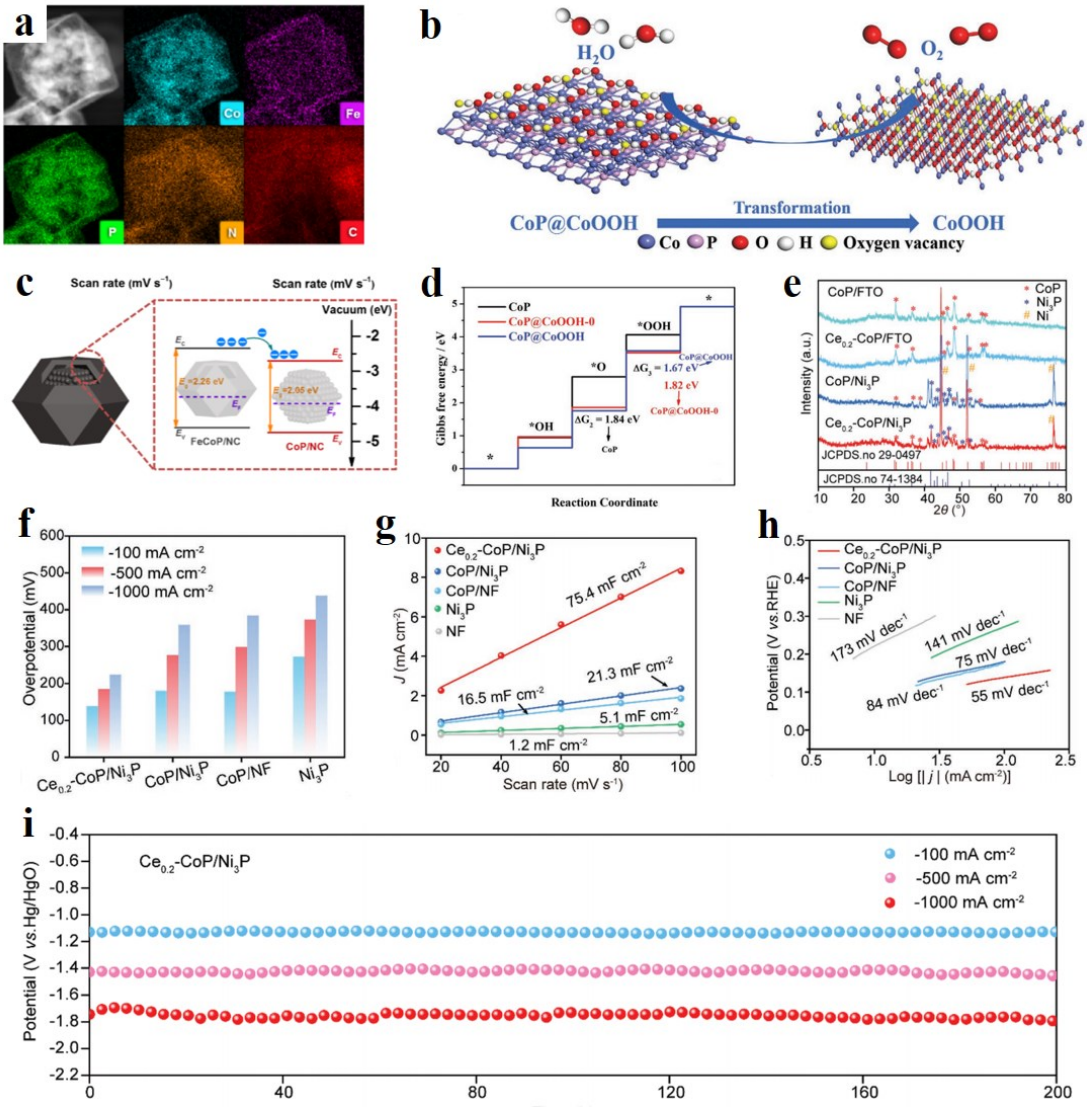

Figure 12. (a) High-angle annular dark-field scanning transmission electron microscopy (HAADF-STEM) and elemental mapping images for Co, Fe, P, N and C of CoP@FeCoP/NC YSMPs. Reproduced with permission. [115] Copyright 2021, Elsevier. (b) The transformation of CoP@CoOOH to CoOOH phase and the mechanism diagram of OER on the CoOOH surface. Reproduced with permission. [116] Copyright 2022, John Wiley and Sons. (c) Schematic energy band diagram of CoP@FeCoP/NC YSMPs. Reproduced with permission. [115] Copyright 2021, Elsevier. (d) The calculated free-energy diagram for OER on CoP, CoP@CoOOH-0, and CoP@CoOOH systems. Reproduced with permission. [116] Copyright 2022, John Wiley and Sons. (e) The XRD patterns of CoP/FTO, $Ce_{0.2}$-CoP/FTO, CoP/Ni_3P, $Ce_{0.2}$-CoP/Ni_3P. (f) The overpotentials of $Ce_{0.2}$-CoP/Ni_3P@NF, CoP/Ni_3P@NF, CoP/NF, Ni_3P@NF. (g) C_{dl}

values, (h) Tafel slopes of $Ce_{0.2}$-CoP/Ni_3P@NF, CoP/Ni_3P@NF, CoP/NF, Ni_3P@NF and bare NF. (i) Chronopotentiometry of $Ce_{0.2}$-CoP/Ni_3P@NF at -100, -500, and -1000 mA cm^{-2}. Reproduced with permission. [108] Copyright 2022, John Wiley and Sons.

1.3.2.2 Transition metal sulfides

Transition metal sulfides (TMS), especially MoS_2, have been widely studied due to their superior HER performance [32,34]. To develop TMS-based nanomaterials for efficient electrocatalysis, researchers have utilized the following strategies: a) Construct defect-rich surface and expose more active sites, thus promoting intrinsic activity. b) Combine the TMS nanomaterials with highly conductive carbon substrates to fabricate hybrid materials, accelerating the charge transfer and improving the performance. D. Zhang *et al*. [120] developed a one-step synthetic strategy to construct NiS/graphene heterostructures. To fabricate the two-dimensional/two-dimensional structure, researchers used deep eutectic solvents (DESs) as precursors followed by the pyrolysis method and sulfidation process. DESs precursor favored interface coupling during the synthetic process, thus successfully constructing the heterojunction structure between NiS and graphene and endowing the nanocomposite material with more active sites and enhanced conductivity. **Figure 13a** shows the atomic arrangement of the NiS/graphene heterostructures and relevant water splitting mechanism on the catalysts' surface. The theoretical calculations showed that the Gibbs free energy values of hydrogen adsorption largely decreased after the NiS/graphene two-phase recombination, indicating this heterojunction structure reduced the energy barrier and boosted the HER electrocatalytic performance. As a result, the electrolyzer constructed by the NiS/graphene bifunctional catalysts required a cell voltage of 1.54 V to afford 10 mA cm^{-2}, and it exhibited higher efficiency than the benchmarks (commercial Pt/C || IrO_2) and other reported non-noble metal bifunctional catalysts shown in **Figure 13b**. K. Srinivas *et al*. [121] developed a partial sulfurization strategy and applied it to

construct different nickel forms (Ni, α-NiS, β-NiS) implanted in the semi-MOF nanosheets. **Figure 13c** shows the schematic illustration of the synthetic process, which contained a two-step protocol of the hydrothermal reaction and annealing process. Researchers combined the Ni/NiS heteronanoparticles with a carbon nanotube network and this material displayed excellent bifunctional performance for HER and OER, requiring low overpotentials of 123 mV and 224 mV at 10 mA cm^{-2} in alkaline medium for HER and OER, respectively. **Figure 13d** shows the estimated double-layer capacitances (C_{dl}) of as-synthesized samples. Higher C_{dl} values indicated a larger electrochemical surface area (ECSA) of the catalysts, and the Ni-M@C-130 sample exhibited the largest ECSA and more numbers of exposed active sites. Unlike the pristine or completely pyrolyzed MOFs, this semi-MOF provided enhanced electronic conductivity and mechanical durability, bringing a new inspiration for novel MOF-derived nanocomposites' fabrication. To promote the multifunctional activity of MoS_2-based electrocatalysts, X. Xu *et al*. [122] calculated the theoretical performance of different transition metal single-atom catalysts (SACs) supported on MoS_2 edge. The exceptional HER activity of MoS_2 edges and the OER active sites provided by single-metal atoms endowed the composite material with bifunctional properties for overall water splitting. Researchers considered the local structure of active sites and the chemical environment, which could predict OER activities of different MoS_2-based SACs by density functional theory (DFT) calculations. The results offered a theoretical basis for the experimental design of MoS_2-based SACs. J. Bao *et al*. [43] combined three-dimensional (3D) and two-dimensional (2D) structures to construct amounts of diffusion channels and well-exposed interfaces. The 2D heterogeneous structural nanosheet-assembled Co–Ni–P/MoS_2 spheres exhibited flower-like morphology, which offered amounts of continuous channels and improved mass/electron transfer. The mechanically stable 2D nanosheets prevented particle aggregation and electrochemical deformation. The DFT calculations indicated that the chemisorption of oxygen-containing species and hydrogen showed outstanding performance and improved the rate-determining step, thus enhancing the bifunctional electrocatalytic performance.

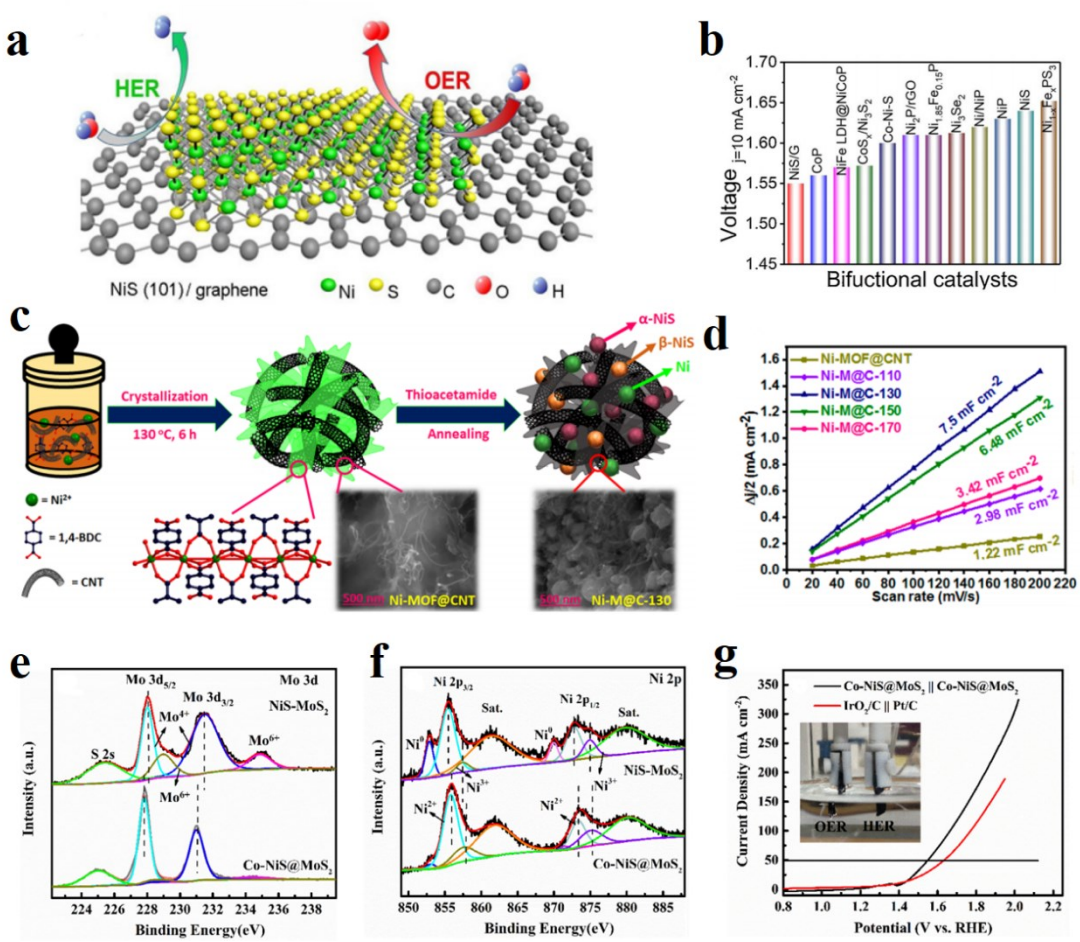

Figure 13. (a) Proposed overall water splitting mechanism on NiS/Graphene. (b) Comparison of overpotentials between NiS/G-3 and other catalysts for overall water splitting at 10 mA cm^{-2}. Reproduced with permission. [120] Copyright 2019, Elsevier. (c) Schematic illustration of Ni/(α,β)-NiS heteronanoparticle-implanted semi-MOF nanosheet fabrication strategy. Reproduced with permission. [121] Copyright 2021, American Chemical Society. (d) Estimated double-layer capacitances (C_{dl}) and electrochemical active surface areas (ECSA) of pristine Ni-MOF@CNT and the semi-MOF derivatives. Reproduced with permission. [121] Copyright 2021, American Chemical Society. (e) High-resolution XPS spectra of Mo 3d for NiS-MoS_2 and Co-NiS@MoS_2. Reproduced with permission. [123] Copyright 2021, Elsevier. (f) High-resolution XPS spectra of Ni 2p for NiS-MoS_2 and Co-NiS@MoS_2. Reproduced with permission. [123] Copyright 2021, Elsevier. (g) LSV curves of Co-NiS@MoS_2 || Co-NiS@MoS_2 and IrO_2/C || Pt/C (Inset: the device diagram of two-electrode water splitting system). Reproduced with permission. [123] Copyright 2021, Elsevier.

Heterojunction fabrication and corresponding interfacial engineering have been widely utilized for catalysts' design and development. W. H. Huang *et al*. [124] fabricated a mesoporous binary transition metal sulfide CoS/MoS_2 by a facile sulphuration of the bimetallic zeolitic imidazolate framework (ZIF). This mesoporous morphology provided contacting interfaces for charge/mass transfer, increased electrochemical surface area, and accessible active sites. The strong interaction between the transition metal Co and Mo resulted in excellent performance in water splitting, and the electrolyzer achieves a low cell voltage of 1.61 V at 10 mA cm^{-2}. Y. Li *et al*. [125] designed a complex structure based on transition metal sulfides. Researchers fabricated Mo-doped NiS_x nanoarrays and then electrodeposited the NiFe LDH on them. Compared with the NiS_x nanoarrays, Mo-doping lowered the hydrogen evolution reaction energy barrier, while the NiFe LDH regulated the electronic structure and facilitated the desorption of oxygen. Besides, the charge density difference simulations indicated that the O-H bond's charge transferred to the Fe-O bond, accelerating the hydrogen desorption. The morphology displayed a three-dimensional hollow core-shell structure, providing favorable mass transfer volume and exposed active centers. As a result, the electrocatalytic performance and stability performed better than previously reported counterparts, requiring low overpotentials of 61.3 mV for HER and 224 mV for OER to deliver 10 mA cm^{-2}. This architectural engineering showcased a design strategy for TMS's modification. H. Zhang *et al*. [126] used a solvothermal method and *in-situ* growth strategy to realize transition metal doping and interface engineering simultaneously. Researchers chose Mo element as the doping agent and $NiS/Ni(OH)_2$ as a host to synthesize a multisite electrocatalyst. This foreign metal doping promoted electronic conductivity and accelerated electron transfer. The theoretical calculations showcased that the NiS (110) and $Ni(OH)_2$ (001) surfaces exhibited intrinsic catalytic properties and strongly interacted with each other, thus improving the overall water splitting performance. Y. Li *et al*. [34] developed a new strategy to grow two-dimensional nanomaterials on three-dimensional carbon substrates. By using sodium dodecyl sulfate as a surfactant, thiourea as S source, $NiAc_2\ 4H_2O$ as Ni source, and

ammonium molybdate as Mo source, researchers designed a one-step method to achieve the collaborative growth of NiS–MoS_2 hetero-nanosheet arrays on carbon substrates. Well-exposed electroactive sites provided by this 2D/3D structure, along with the catalysis-relevant species, facilitated the electrocatalytic performance in alkaline medium. H. Gao *et al*. [123] prepared Co-doped NiS@MoS_2 core-shell nanorods (Co-NiS@MoS_2) through the hydrothermal reaction. As a bifunctional catalyst, Co-NiS@MoS_2 exhibited stable electrocatalytic performance due to the core–shell structure, and required a low cell voltage of 1.54 V to afford 50 mA cm^{-2}, largely exceeding other reported counterparts. **Figure 13e** shows the Mo 3d high-resolution XPS spectra of NiS-MoS_2 and Co-NiS@MoS_2 samples. The peaks' negative shift of the Co-NiS@MoS_2 sample indicated that the Co doping changed the charge distribution of the MoS_2 nanosheets since the incorporation of Co atoms attracted the outer layer electrons of S atoms. The negative shift of XPS peaks could also be investigated in the Ni 2p high-resolution XPS spectra shown in **Figure 13f**. The electron transfer exhibited faster speed between the doped Co atoms and S atoms, resulting in the transformation of the surrounding environment of Ni. These negative shifts of XPS peaks showcased the strong interaction between doped Co and host materials (i.e., MoS_2 nanosheets and NiS), thus accelerating the electron transfer and enhancing the catalytic performance. **Figure 13g** shows the LSV curves of the electrolyzer constructed by Co-NiS@MoS_2, which shows lower overpotentials and better bifunctional performance compared to the counterpart (IrO_2/C || Pt/C electrolyzer). K. Min *et al*. [127] coupled CoS and Co_3O_4 to construct a microcube heterostructure for bifunctional ORR/OER electrocatalysis and rechargeable zinc air batteries. Researchers utilized hydrothermal reaction to coprecipitate Co–Co Prussian blue analog (PBA), further oxidation of furnace heating in air to get Co_3O_4, and sulfidation with Na_2S to fabricate the final product of Co_3O_4/CoS cubes. Compared to commercial Pt/C catalysts, Co_3O_4/CoS cubes displayed a competitive ORR half-wave potential of 0.82 V (vs. RHE) and better methanol tolerance. Rechargeable zinc air battery assembled by Co_3O_4/CoS cathode displayed a cell voltage of 1.51 V and power density of 168 mW cm^{-2} at 269 mA cm^{-2}. Y. Tian *et al*.

[128] anchored CoS/CoO heterostructure on the nitrogen-doped graphene to fabricate rechargeable zinc air batteries. The superior electronic conductivity of graphene materials and local charge redistribution caused by heterogeneous structures cooperatively enhanced the ORR/OER activities. The aqueous zinc air battery fabricated by CoS/CoO@N-doped graphene cathode exhibited a power density of 137.8 mW cm^{-2} and a specific capacity of 723.9 mAh g^{-1}.

1.3.2.3 Transition metal oxides

Transition metal oxides (TMO) and TMO-based nanomaterials have been commonly used for electrocatalysis, such as CoO, MnO_2, CuO, Fe_2O_3, and so on [33,40]. The earth-abundant 3d-transition metals could be easily transformed to their oxides. The unique strength of TMO compared to other transition metal compounds is attributed to the highly active oxygen vacancies. Besides, the superior designability makes it easier to implement heteroatom-doping strategies for TMO, including the metallic atom-doping [40] like Co, Mn, Ni, Fe, Cu, Mo and nonmetal atom-doping like P, S, C, N, thus further facilitating the catalytic activity. D. Guo *et al*. [129] coupled metallic Co with CoO supported on the Ti_3C_2–MXene (defined as Co–CoO/Ti_3C_2–MXene) for cost-effective and highly-efficient electrocatalysis. **Figure 14a** shows the synthetic procedure of this Co–CoO/Ti_3C_2–MXene hybrid material, including etching and exfoliation processes. Characterizations and DFT calculations demonstrated that the metallic Co and CoO could be favorable for HER activity and OER activity, respectively. The Ti_3C_2–MXene could accelerate the charge transfer, facilitate electronic conductivity, and prevent the aggregation of Co–CoO. By coupling these three parts, the synergistic effect resulted in highly efficient bifunctional activity and also superior stability. Co–CoO/Ti_3C_2–MXene displayed excellent electrocatalytic performance with an ultralow onset potential of 8 mV and 196 mV for HER and OER, respectively. Besides, the Tafel slope of Co–CoO/Ti_3C_2–MXene exhibited close to that of Pt/C for HER and superior to that of RuO_2 for OER, indicating exceptional reaction

kinetics for both HER and OER. J. Lu *et al*. [130] applied the cationic intercalation method to tune the electronic state of MnO_2 nanosheets. The intercalated transition metal ions of Co, Ni, and Fe resulted in the transformation of Mn ions from a stable d^3 state Mn^{4+} to an unstable d^4 state Mn^{3+}, thus increasing the oxygen vacancy density in the MnO_2. Oxygen vacancies enhanced the adsorption capacity of *OH intermediate and improved the OER activity. Compared to intercalated Co and Ni ions, Fe-intercalated MnO_2 (Fe–MnO_2/NF) exhibited superior OER performance, requiring a low overpotential of 330 mV at 20 mA cm^{-2}. S. Zhu *et al*. [131] developed a facile synthetic procedure to fabricate the CoO/NF nanowires by hydrothermal reaction and calcination treatment. In the synthetic process, urea served as a morphology regulation agent for the nanowire-like morphology. **Figure 14b** shows the contact angle 147° of bubbles on the CoO/NF catalyst, which could attenuate the interaction between the surface of catalysts and the bubbles, thus accelerating the release of the products. J. Kim *et al*. [132] used the sol–gel method to fabricate bimetallic transition metal oxide Fe_2O_3–MnO heterojunction and coated it on nickel foam (Fe_2O_3–MnO/NF). During the self-redox reactions on the electrodes, Fe reduced hydrogen while Mn oxidized oxygen. This synergistic effect of Mn and Fe improved the electron migration and facilitated the OER activity. Compared to single transition metal oxide samples (Fe_2O_3/NF, MnO/NF), Fe_2O_3–MnO/NF exhibited lower overpotentials and smaller Tafel slope values, and it remained stable without deterioration after 1000 cycles.

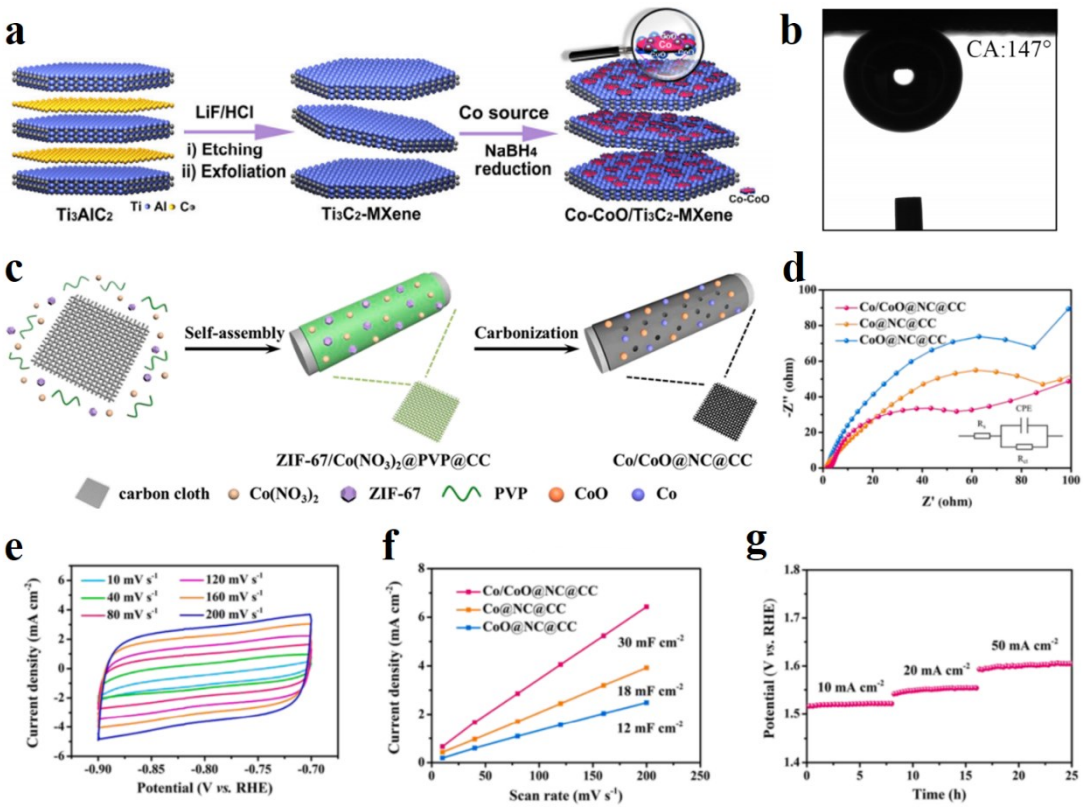

Figure 14. (a) Schematically synthetic procedure of Co-CoO/Ti_3C_2-MXene hybrid. Reproduced with permission. [129] Copyright 2021, Springer Nature. (b) Bubble contact angle of CoO/NF. Reproduced with permission. [131] Copyright 2020, Elsevier. (c) The schematic of preparation process of Co/CoO@NC@CC. Reproduced with permission. [133] Copyright 2021, Elsevier. (d) EIS for the electrocatalysts recorded with an overpotential of 10 mV, inset shows its fitting equivalent circuit. Reproduced with permission. [133] Copyright 2021, Elsevier. (e) CV curves of Co/CoO@NC@CC in the non-Faradic region at various scan rates. Reproduced with permission. [133] Copyright 2021, Elsevier. (f) Plots of the capacitive currents derived from CV curves versus scan rates exhibiting the extraction of C_{dl}. Reproduced with permission. [133] Copyright 2021, Elsevier. (g) Long-term durability test of Co/CoO@NC@CC conducted at various current densities. Reproduced with permission. [133] Copyright 2021, Elsevier.

Combining different types of TMOs contributed to the increasing active sites and synergistic effects. S. Sirisomboonchai *et al*. [134] combined different transition metal

oxides to optimize the electronic distribution and facilitate the intrinsic electrocatalytic activity. Researchers fabricated a core–shell structure of CuO_x nanowires core and $NiMnO_x$ nanosheets shell (CuO_x NWs@ $NiMnO_x$ NSs). Specifically, researchers electrochemically deposited the defect-rich $NiMnO_x$ nanosheets on the $Cu(OH)_2$ nanowires and then implemented a thermal process to transform the $Cu(OH)_2$ nanowires into CuO_x nanowires. A Large number of vacancies, defects, and dislocations in the $NiMnO_x$ nanosheets shell provided numerous active edge sites and the coordination-unsaturated crystal structure, thus promoting the intrinsic electrocatalytic activity. Except for the defect engineering, valence state regulation caused by the synergistic effect of CuO_x nanowires core and $NiMnO_x$ nanosheets shell could also provide more adsorption sites and active centers. As a result, CuO_x NWs@ $NiMnO_x$ NSs exhibited prominent performance in both alkaline and neutral media. It required ultralow overpotentials of 80.7 mV and 390 mV at 10 mA cm^{-2} with a Tafel slope of 77.6 mV dec^{-1} and 101.6 mV dec^{-1} in a neutral electrolyte for HER and OER, respectively. K. Dai *et al*. [133] developed a self-assembly-carbonization strategy to fabricate bifunctional electrocatalysts. Researchers combined favorable OER kinetics of cobalt oxides, applicable hydrogen binding energy of Co metal, and favorable electronic conductivity of N-doped carbon layer to synthesize the N-doped carbon layer-anchored Co/CoO supported on carbon cloth (Co/CoO@NC@CC) shown in **Figure 14c**. To unravel the mass/electron transfer properties, researchers utilized EIS spectra to evaluate the charge transfer resistance shown in **Figure 14d**. The resistance value of Co/CoO@NC@CC (69.4 Ω) was smaller than that of counterparts. The double-layer capacitance (C_{dl}) values derived from cyclic voltammetry (CV) curves at different scan rates shown in **Figure 14e** indicated that Co/CoO@NC@CC exhibited larger C_{dl} value shown in **Figure 14f** and improved electrochemical surface area. The result suggested that the hierarchical porous structure benefited the electrolyte penetration and accelerated the ion diffusion to adsorption sites. The durability test in **Figure 14g** indicated that Co/CoO@NC@CC remained stable for 8 h at 10 and 20 mA cm^{-2}, while it displayed a 13 mV overpotential increase at 50 mA cm^{-2} for 9 h. M. Wang

et al. [135] utilized reconstructing method to *in situ* generate CoO_x for efficient OER electrocatalysis. By using characterizations including X-ray absorption spectroscopy, Raman spectroscopy, and X-ray reflectivity, researchers investigated the conversion of Co_9S_8 to CoO_x cluster. The *in situ* generated cobalt oxide cluster consisting of CoO_6 octahedral clusters provided active sites for OER, which could be further verified by DFT calculations. This work brings new insights for designing and reconstructing transition metal-based materials as efficient electrocatalysts. F. Nasim *et al*. [136] designed a nonprecious metal-based nitrogen-doped carbon nanotube (NCNT) to solve the high-cost, self-poisoning problems of noble metal-based electrocatalysts. Researchers used NCNT to in situ encapsulate the CoO_x and further partial phosphating process to get CoO_x–CoP/NCNT, showcasing an onset potential of 0.96 V and a half-wave potential of 0.81 V in alkaline medium. The acid treatment before the partial phosphating process successfully removed extra Co species and promoted catalytic activity.

1.3.2.4 Transition metal nitrides

The unique physical, chemical properties [38], and electronic structure endow transition metal nitrides (TMN) with superior catalytic performance, especially for overall water splitting. The introduction of N atom into the transition metal elements successfully increases the electron density and regulates the surface electronic structure [37]. The ionic bonds between N atoms and metal ions, covalent bonds in N atoms, and metallic bonds in metal elements coexist in the TMN-based materials, thus improving the activity and durability. Y. Lu *et al*. [137] prepared Co–Mo nitride nanosheet arrays supported on nickel foam ($CoMoN_x$ NSAs/NF) for non-noble metal electrocatalyst fabrication. Researchers utilized hydrothermal reactions to get transition metal oxides supported on nickel foam named $CoMoO_4$/NF and then applied a nitridation process via furnace heating at different temperatures (300, 400, 500, and 600 °C) in NH_3/Ar atmosphere. Co_2N and Mo_2N in the material synergistically improved the charge

transfer and facilitated the catalytic activity. **Figure 15a** shows the high-resolution TEM image of $CoMoN_x$ NSAs/NF. The lattice fringes of 0.314 nm and 0.208 nm corresponded to Co_2N (311) plane and Mo_2N (200) plane, respectively. The HER performance comparison shown in **Figure 15b** indicated that the sample via furnace heating at 500 ℃ ($CoMoN_x$-500 NSAs/NF) exhibited a low overpotential of 208 mV at the current density of 100 mA cm^{-2}, smaller than $CoMoO_4$/NF precursor and other $CoMoN_x$ NSAs/NF samples. The OER performance comparison shown in **Figure 15c** indicated that the $CoMoN_x$-500 NSAs/NF sample performed better than other counterparts at both 10 and 100 mA cm^{-2}. The electrolyzer assembled by $CoMoN_x$ NSAs/NF exhibited superior performance compared to other reported transition metal nitrides, requiring a cell voltage of 1.55 V to afford 10 mA cm^{-2}. Z. Liu *et al*. [138] designed a novel bimetallic nitride $FeNi_3N$ for bifunctional electrocatalysis by structure and morphology modification. Researchers fabricated these hollow structured $FeNi_3N$ nanoparticles via oxygen-etching and the following thermal nitridation. After the nitridation process of $FeNi_3$, OER performance has been improved without the HER performance loss. The metallic $FeNi_3N$ phase, numerous active site exposure by hollow structure, and enhanced charge transfer cooperatively contributed to the superior water splitting performance. X. Zhou *et al*. [139] engineered active Fe sites in the Fe_2P/Co_2N porous heterostructure arrays to construct highly efficient and stable electrocatalysts for large-current-density hydrogen production. This hybrid catalyst displayed superb bifunctional performance, requiring ultralow overpotentials of 131 mV and 283 mV to attain the large current density of 500 mA cm^{-2}. Besides, the electrolyzer assembled by Fe_2P/Co_2N only required cell voltages of 1.56 and 1.66 V to afford 100 and 500 mA cm^{-2}, respectively. The Fe sites, served as active centers, possessed optimal *H intermediate binding energy due to the interfacial interaction between the Fe_2P/Co_2N heterostructure. C. Zhu *et al*. [140] fabricated trimetallic transition metal nitride Ni-Fe-MoN nanotubes (Ni-Fe-MoN NTs) via room-temperature reaction to achieve iron incorporation and the following annealing process in NH_3 atmosphere, shown in **Figure 15d**. The nonprecious transition-metal nitride nanostructure endowed this catalyst with

cost-effective, robustly durable, highly efficient properties, and the Ni-Fe-MoN NTs||Ni-Fe-MoN NTs electrolyzer delivered a current density of 10 mA cm^{-2} at a low overpotential of 1.513 V. The SEM image shown in **Figure 15e** showed the nanotubes with diameters of approximately 300 nm, exposing a large number of active sites.

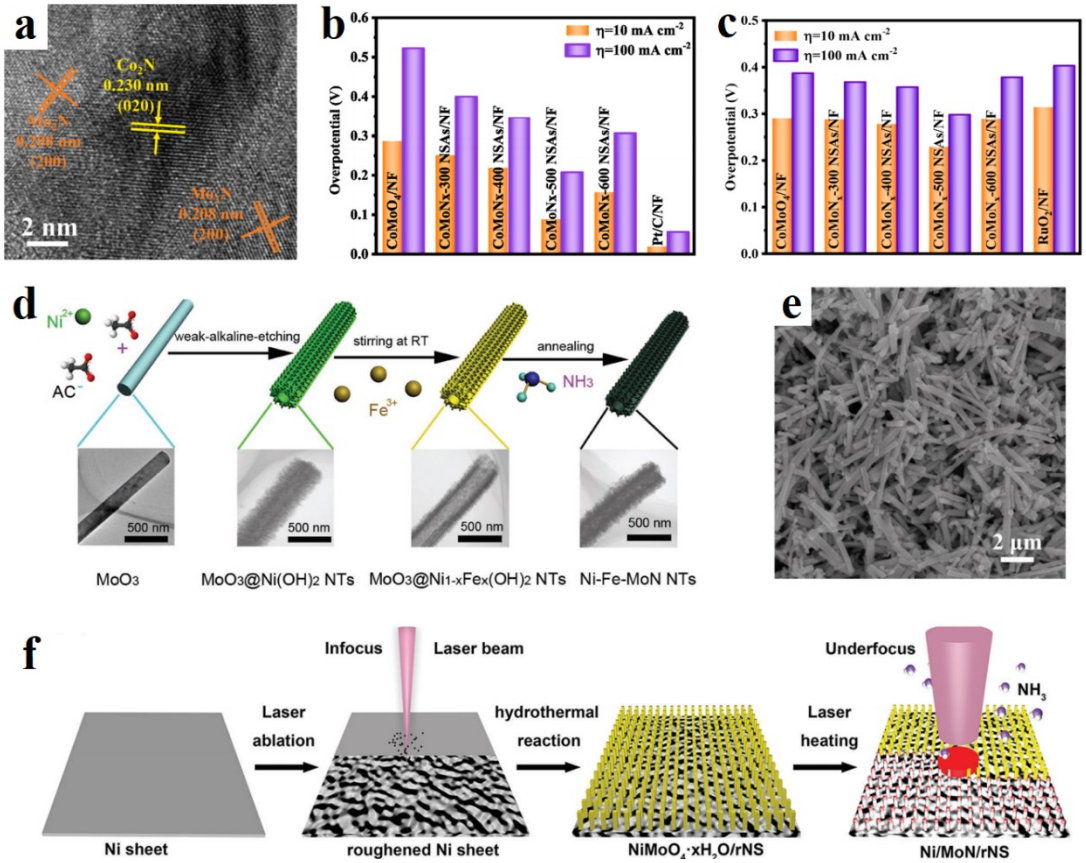

Figure 15. (a) HRTEM image of $CoMoN_x$-500 NSAs/NF. Reproduced with permission. [137] Copyright 2021, Elsevier. (b) Comparison of the overpotential at the current densities of 10 mA cm^{-2} and 100 mA cm^{-2} for the HER performance of Pt/C/NF, $CoMoO_4$/NF, and a series of $CoMoN_x$ NSAs/NF catalysts. Reproduced with permission. [137] Copyright 2021, Elsevier. (c) Comparison of the overpotential at the current densities of 10 mA cm^{-2} and 100 mA cm^{-2} for the OER performance of RuO_2/NF, $CoMoO_4$/NF, and a series of $CoMoN_x$ NSAs/NF catalysts. Reproduced with permission. [137] Copyright 2021, Elsevier. (d) Synthesis of the Ni-Fe-MoN NTs. Reproduced with permission. [140] Copyright 2018, John Wiley and Sons. (e) SEM image of the trimetallic Ni-Fe-MoN NTs. Reproduced with permission. [140] Copyright 2018, John Wiley and Sons. f) Synthetic scheme of Ni/MoN/rNS. Reproduced with permission.

[141] Copyright 2022, John Wiley and Sons.

The morphology of nanomaterials has an important influence on the properties, because the exposed active surface area determines the number of active sites, and the porous morphology benefits the mass transfer. Y. Sun *et al*. [142] *in situ* synthesized porous MoN with petal-like morphology and coated MoO_2 heterojunction (MoO_2@MoN) via a localized nitride transformation method. The combination of transition metal nitrides and transition metal oxides endowed the material with superb electronic conductivity and ion transfer, thus promoting electrocatalytic activity. Q. Zhang *et al*. [143] utilized transition metal nitride WN with metallic Ni to construct Mott-Schottky heterostructure via one-pot pyrolysis and combined it with N, P co-doped carbon nanotubes (WN–Ni@N, P–CNT). This novel multifunctional material performed superior activity for ORR/OER/HER. Mott-Schottky heterostructure accelerated the charge transfer and H_2O dissociation process at atomic level. Attributed to the excellent ORR and OER activity, rechargeable zinc air battery (ZAB) assembled by WN–Ni@N, P–CNT exhibited an enhanced power density of 126.2 mW cm^{-2}, which outperformed the commercial Pt/C||IrO_2 ZAB. The durability test showcased that the battery performance remained stable after 330 h discharge-charge process. P. Wang *et al*. [144] reported a novel strategy to fabricate a heterostructure consisting of metallic Ni and transition metal nitride MoN encapsulated by N-doped carbon nanotubes (CNT) supported on carbon cloth (Ni/MoN@NCNT@CC). This complex nanocomposite combined the advantages of different parts for efficient water splitting, including the high electronic conductivity of N-doped CNT, high intrinsic activity of Ni/MoN heterostructure, enlarged surface area, and numerous exposed active sites provided by 3D carbon cloth skeleton. R. Jamil *et al*. [145] focused on the function of nitrogen in transition metal nitrides for water splitting. Except for the superior intrinsic properties such as wide pH durability, potential for structural design and modification, and high corrosion resistance, researchers identified active sites and decoded the inherent mechanisms. They revealed that ordered and disordered structure properties had a significant impact

on the HER activity. Y. Chen *et al*. [141] designed a new strategy to fabricate an inexpensive transition metal nitride catalyst Ni/MoN/rNS, combining MoN microrods and Ni nanoparticles supported on roughened nickel sheet. **Figure 15f** shows the synthetic procedure of Ni/MoN/rNS, consisting of laser ablation, hydrothermal reaction, and laser heating process. As a result, the stress and local high temperature induced by laser heating controllably fabricated the Ni/MoN/rNS material, performing an exceptional bifunctional activity. Specifically, the Ni/MoN/rNS electrode required low overpotentials of 67 mV to deliver a current density of 10 mA cm^{-2} in 1.0 M KOH for HER. The theoretical calculations revealed that the Ni/MoN interface reduced Gibbs free energy barrier of hydrogen absorption to -0.19 eV, compared to that of MoN (-0.39 eV) and Ni cluster (-0.34 eV), thus improving the HER kinetics. C. Feng *et al*. [146] designed a novel Fe/FeN@N–C electrocatalyst to construct nitrogen-coordinated transition metal atoms as active centers for highly efficient ORR. Researchers utilized 2-methylimidazole as nitrogen source and Fe-MIL-101-2-MI as precursor, and optimized the catalytic activity by tuning the doping amount of nitrogen and calcination temperature. As a result, as-obtained sample exhibited an initial potential of 0.873 V (vs. RHE), a half-wave potential of 0.813 V (vs. RHE), and a limit current density of 6.04 mA/cm^2. The nanorod morphology benefited the charge transfer and the coordination of 2-methylimidazole largely increased the FeN active centers, thus enhancing the ORR electrocatalytic performance.

1.3.2.5 Transition metal carbides

Transition metal carbides (TMC) possess many excellent properties, including high conductivity [37], superior chemical stability, remarkable flexibility, *etc*. The morphology of ultrathin 2D transition metal carbides can enhance the intrinsic catalytic activity and endow the TMC-based nanomaterial with superb designability to construct hybrid materials [147,148]. Q. Hu *et al*. [149] reported a one-step method to fabricate bimetallic alloy transition metal carbides. Researchers coupled the Mo_2C-doped

bimetallic NiFe alloy with N-doped graphene to get NG-NiFe@MoC_2 nanohybrids. The hybrid precursors contained polyvinylpyrrolidone, Mo^{6+} cations, and NiFe Prussian blue analogues, shown in **Figure 16a**, and further calcination of the hybrid precursors yielded the NG-NiFe@MoC_2 nanohybrids. The electrolyzer assembled by NiFe@MoC_2 in alkaline medium required a cell voltage of 1.53 V to afford 10 mA cm^{-2} over 10-hour operation, exhibiting superb performance and long-term durability. R. Zhang *et al*. [147] prepared MoO_2/MoC_2 heterogeneous microspheres via hydrothermal reaction and the following annealing process. The morphology of the annealing precursor H_xMoO_3/C and the product MoO_2/Mo_2C microspheres was shown in **Figure 16b** and **Figure 16c**, respectively. It suggested that the annealing process reduced the diameter from 1.2–1.4 μm of precursors to 300–500 nm of MoO_2/Mo_2C microspheres, thus exposing more surface area. The XRD patterns shown in **Figure 16d** further verified the composition of the MoO_2/Mo_2C microspheres. The peak strength comparison between MoO_2/Mo_2C, MoO_2, and Mo_2C indicated that the principal part of MoO_2/Mo_2C microspheres was MoO_2, due to the weak Mo_2C characteristic peak in MoO_2/Mo_2C sample. MoO_2/Mo_2C microspheres exhibited good electrocatalytic performance in 0.5 M H_2SO_4 with low overpotentials. Y. Yu *et al*. [150] investigated the electrocatalytic performance of 2D transition metal carbides systematically via first-principles calculations. These 2D TMC possessed fast charge transfer due to the intrinsic properties of high electronic conductivity and good stability. Among numerous TMC materials, NbC_2, TaC_2, and MoC_2 exhibited superior HER activity with low overpotentials and reduced Gibbs free energy barrier of hydrogen adsorption shown in **Figure 16e**. H. Huang *et al*. [148] embedded the Co/MoC nanoparticles into the nitrogen-doped graphene structure (Co/MoC@N–C) via ball milling process and furnace heating. Specifically, researchers used zinc oxide, dimethylimidazole, and Co/Mo carbonyl to *in situ* encapsulate the Co/Mo species into ZIF–8, and further annealing under Ar atmosphere for 2 h to construct the graphene structure. As ORR/OER bifunctional catalysts, Co/MoC@N–C exhibited an ORR half-wave potential of 0.824 V (vs. RHE) and an OER overpotential of 290 mV at 10 mA cm^{-2} in

alkaline medium, outperforming the performance of commercial catalysts like Pt/C and RuO_2.

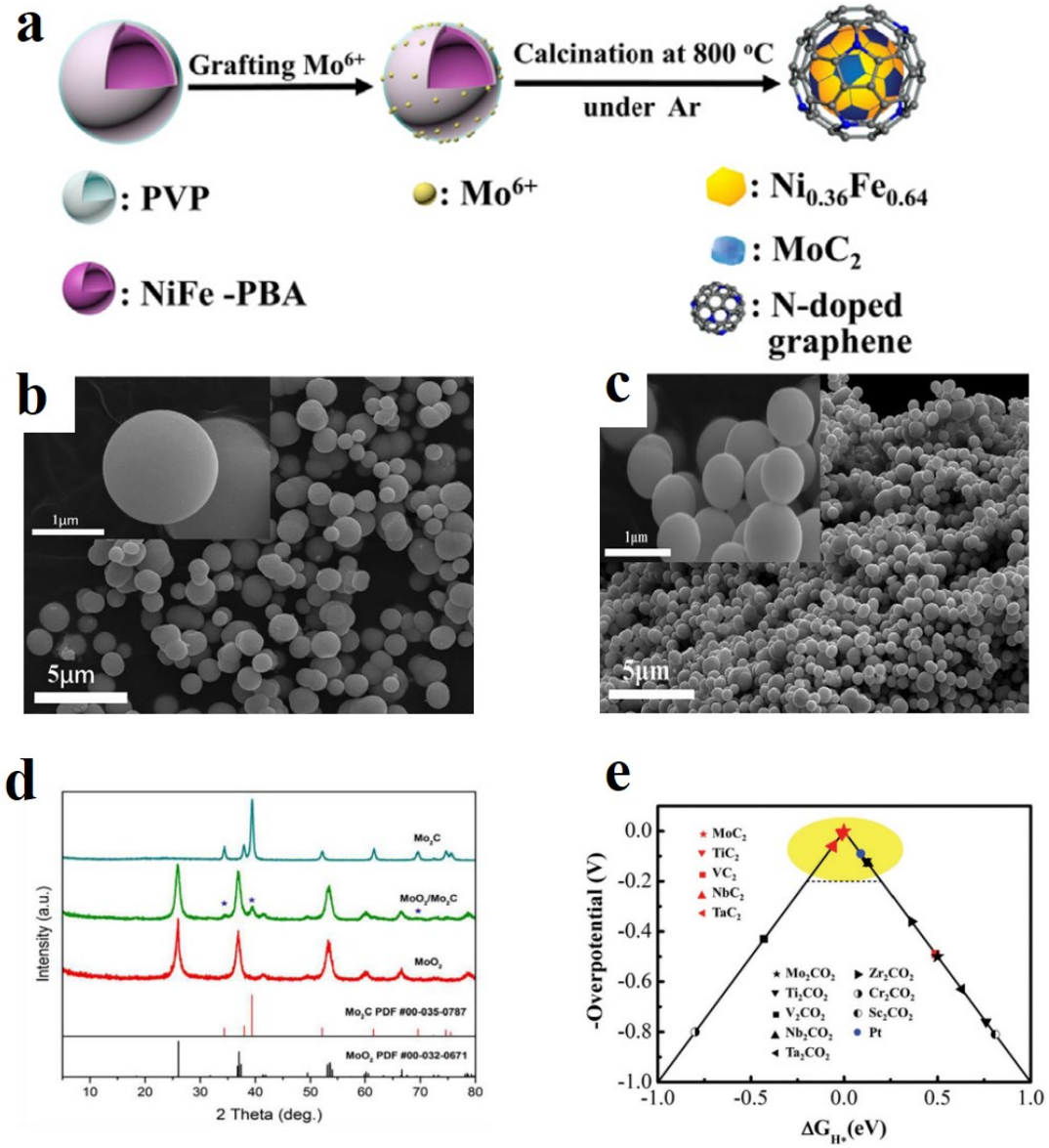

Figure 16. (a) Synthetic scheme of NG-NiFe@MoC_2. Reproduced with permission. [149] Copyright 2018, Elsevier. (b) SEM images of H_xMoO_3/C precursors. Reproduced with permission. [147] Copyright 2021, Elsevier. (c) SEM images of MoO_2/Mo_2C microspheres. Reproduced with permission. [147] Copyright 2021, Elsevier. (d) XRD patterns of Mo_2C, MoO_2/Mo_2C and MoO_2. Reproduced with permission. [147] Copyright 2021, Elsevier. (e) HER volcano curve of MC_2 (red) compared to previously reported traditional MXenes (black) and the most commonly used Pt (blue). The

systems with overpotentials below 0.2 V are located in the yellow shaded area. Reproduced with permission. [150] Copyright 2020, John Wiley and Sons.

1.3.2.6 Cobalt phosphides

Among various transition metal phosphides, cobalt phosphides have attracted extensive interest and have been studied comprehensively regarding the aspects of intrinsic advantages, synthetic routes, and modification methods [39]. The properties of natural abundance, catalytic activity, and electronic conductivity endow the cobalt phosphide-based nanomaterials with the potential to fabricate good bifunctional electrocatalysts. Cobalt phosphides possess a trigonal prism crystal structure and different chemical bonds including covalent bonds and metallic bonds [36]. These structural features can lead to unique metallic or semiconductor properties, providing various design possibilities and modification strategies.

The commonly used preparation ways for cobalt phosphides are solid-phase reaction, electrodeposition, and organic ligand-assisted fabrication [31]. The solid-phase reaction means the thermal reaction of mixed cobalt sources and phosphorus sources under an inert atmosphere. Researchers could synthesize some frameworks containing cobalt species like ZIF-67 frameworks, and further calcination and phosphating process in the furnace tube can fabricate cobalt phosphides. Electrodeposition could directly grow the cobalt phosphides on the electrode surface, or just coat a thin layer of cobalt species followed by the phosphating process. For the organic ligand-assisted fabrication, researchers usually used oleic acid or oleylamine as the organic solvent to synthesize cobalt phosphide nanoparticles.

According to effective strategies such as electronic structure modification, surface active area amplification, and interface engineering, most cobalt phosphide-based nanomaterials developed in recent years could achieve low overpotentials of less than 80 mV at the current density of 10 mA cm^{-2} for HER, while some of the cobalt phosphide-based nanomaterials could achieve low overpotentials of less than 50 mV at

the current density of 10 mA cm^{-2} like CoP/NiCoP NTs [151]. For OER, most cobalt phosphide-based nanomaterials could achieve low overpotentials of less than 300 mV at the current density of 10 mA cm^{-2} while some nanomaterials could achieve low overpotentials of less than 220 mV like Fe-CoP/CoO [152].

1.3.2.7 Nickel sulfides

Nickel sulfide is one of the most promising water-splitting electrocatalysts due to its excellent bifunctional HER/OER activity. As transition metal compound, nickel sulfide is cost-effective and earth-abundant. It also shows some unique properties resulting in good electrocatalytic performance, including adjustable electronic structure, superb conductivity, multiple crystalline structures [32], *etc*. We can analyze the nickel sulfide nanomaterials starting with the atomic structure. Nickel sulfide, including Ni_3S_2, NiS_2, and NiS, exhibits different nickel valences like the divalent nickel and trivalent nickel [153]. This multivalent state facilitates the adsorption of reactants on the surface and accelerates the dissociation of the water molecules into the reaction intermediate *OOH. Besides, the Ni-Ni bonds can largely improve the electronic conductivity of the whole material. Except for the excellent properties of the nickel part, Ni-S bonds in nickel sulfides are reactive to hydrogen molecules and the adsorption energy barrier is low, leading to the accelerated kinetics for the HER rate-determining step [154]. The different crystal structures of nickel sulfides provide extensive crystal planes for efficient electrocatalysis. For example, the Ni_3S_2 is a hexagonal phase, and the nickel atoms are located at the center of the body-centered cubic crystal structure while the sulfur atoms mainly form the inclined body-centered cubic crystal structure. In the synthesis design, researchers can expose the high-index surface as much as possible to construct multiple active sites on the surface.

For the preparation of nickel sulfides, researchers usually have three choices. The first one is the hydrothermal method [155], involving both sulfur sources and nickel sources. Sodium sulfide, thiourea, and thioacetamide can be selected as sulfur sources, while the

nickel salts like nickel nitrate can be selected as nickel sources. Besides, when we choose the nickel foam as substrate, this substrate automatically contains nickel sources. The second method is gas sulfurization under the hydrogen sulfide gas or other sulfur gas atmosphere. The third one is the electrodeposition method to directly deposit the target nanomaterials on the electrode surface.

Researchers developed multiple modification methods to enhance the electrocatalytic activity of nickel sulfides and achieved pretty good water-splitting performance. The methods include extensive doping strategies, high-index exposure strategies, controllable morphology designs, and nanocomposite designs with different nanomaterials. After the modifications, most nickel sulfide-based nanomaterials could require low overpotentials of less than 100 mV at the current density of 10 mA cm^{-2} for HER, while some excellent performances achieved ultralow overpotentials less than 60 mV at 10 mA cm^{-2} like V-Ni_3S_2/CC [156]. For OER, nickel sulfide-based nanomaterials could require low overpotentials of less than 300 mV at the current density of 10 mA cm^{-2} while some excellent performances achieved ultralow overpotentials less than 200 mV at 10 mA cm^{-2} such as P-MoS_2/Ni_3S_2/NF [157] and FeS/Ni_3S_2@NF [158]. For the overall water splitting, the cell voltage of the electrolyzer assembled by nickel sulfide-based nanomaterials is around 1.50 V at the current density of 10 mA cm^{-2}. Some efficient bifunctional electrocatalysts only require a cell voltage of less than 1.50 V at 10 mA cm^{-2} like 1.45 V of the leaf-like Ni_3S_2 nanosheets [159].

1.4 Conclusion and perspectives

With the development of electrocatalysis, more and more materials have been studied for different electrocatalytic reactions. Except for the researches on commercial catalyst-based materials (like Pt-based catalysts), researchers have proposed and designed lots of novel materials [160] such as alloys, transition metal phosphides, sulfides, nanocomposites, single-atom catalysts, *etc*.

Owing to the various design strategies, transition metal compound-based nanomaterials have been gradually studied in the past few years. It's a promising way to fabricate low-cost, highly efficient, and strongly stable electrocatalysts based on transition metal compounds, benefiting the development of large-scale applications for practical industrialization. Based on the above literature review, transition metal compound-based nanomaterials possess the following properties: a) Transition metal compounds possess a large number of active sites provided by metal ions on the surface, while the anions could regulate the electronic structure to influence the intrinsic catalytic activity. b) The different oxidation states of metal ions contribute to the multifunctionality of the nanomaterial. c) The heterojunction constructed by different transition metal compounds redistributes the electronic structure and accelerates the charge transfer. d) The superior designability makes it possible to fabricate complex structures for multifunctional electrocatalysis.

Due to the higher reserves compared with Pt [161], researchers try to fabricate Pd-based on catalysts for efficient and stable ORR, OER, and HER. Recent works demonstrated that the precious metal Pd has the potential to achieve equivalent or even better electrocatalytic performance in comparison with Pt [162]. According to the comprehensive analysis, Pd-containing nanomaterials have the following intrinsic advantages: a) Palladium is more abundant than platinum. b) Pd could provide active sites for both ORR and HER, and PdO could provide active sites for OER. Therefore, the palladium element has intrinsic activities for these reactions, providing the foundation for further electrocatalytic performance improvement. c) Pd-based materials are closer to the optimized oxygen binding strength in the alkaline medium, so it's easier to balance the oxygen-containing chemicals' adsorption and desorption, which plays an important role in the electrocatalytic ORR and OER reactions [163]. d) Pd-containing materials with different nanostructures and morphologies are studied by extensive researchers and they developed relatively mature methods for designing and synthesizing novel materials.

Recent studies on transition metal compound-based and Pd-based nanomaterials for

ORR, OER, HER, and multifunctional applications are summarized in this review. There are many challenges no matter in ORR, OER, or HER, and the key point is to design electrocatalysts towards the goal of low cost, high activity, good stability, and multifunction. Many studies proposed useful strategies to further towards the goal such as alloying, defect engineering, strain engineering, single atom catalyst design, framework-directed nanocomposite design, morphology engineering, surface treatment, and so on [164]. There is still a long way to go before the successful commercialization of these novel nanomaterials. Although some novel nanomaterials exhibit excellent mass activity, the mass production needs multi-dimensional investigation, and the industry production conditions are quite different from the laboratory conditions. It is believed that transition metal compound-based, Pd-based, and other metal-based nanomaterials are promising for high-performance and stable electrocatalysis.

Chapter 2. Objectives

The objective of this work is to design a facile synthetic route to fabricate cost-effective, highly efficient, and stable multifunctional electrocatalysts.

Based on the literature review in Chapter 1, the following aspects can be further improved through experimental research: a) As a typical application of multifunctional electrocatalysis, electrocatalytic water splitting is one of the most promising hydrogen production technologies. However, several challenges still exist and need to be overcome: the high cost of the state-of-the-art HER electrocatalysts Pt/C and OER electrocatalysts RuO_2 or IrO_2; the sluggish reaction kinetics of both HER and OER limits the overall performance and energy conversion efficiency; the poor stability and performance at large current densities impedes the development of large-scale hydrogen production. b) Transition metal-based electrocatalysts have recently attracted much attention due to their low cost, facile fabrication, and numerous active sites. However, the catalytic performance gap between the transition metal-based and noble metal-based nanomaterials still exists, especially at large current densities. c) The poor electronic conductivity of non-noble metal-based nanomaterials hinders charge transfer.

To further improve the above aspects, the following objectives have been defined for the scope of this thesis: a) Design and synthesize a transition metal compound-based nanomaterial for large-current-density bifunctional HER/OER water splitting in alkaline conditions. Based on the as-synthesized catalysts, further fabricate the HER/OER electrodes and the water splitting device. b) Construct heterogeneous structures during the synthetic process to increase active sites, accelerate charge transfer, and optimize the reactant adsorption, thus improving the overall performance. c) Support the nanomaterials on the nickel foam to enhance the electronic conductivity and fabricate self-supported electrodes.

Chapter 3. Fabrication of Co_2P-Ni_3S_2/NF heterogeneous structural hollow nanowires as bifunctional electrocatalysts for efficient overall water splitting

3.1 Introduction

Traditional energy forms (e.g., fossil energy) have been gradually replaced by some novel energy forms (e.g., wind energy, electrochemical energy) due to the development of environmentally friendly energy generation strategies [1-3]. More importantly, fossil fuels are non-renewable resources, while novel energy generation methods (e.g., fuel cells, solar cells) show inexhaustible properties. These kinds of clean and highly efficient energy attracted much attention from scientists, among which hydrogen energy is one of the most important sustainable energy forms [31]. However, the traditional hydrogen production is still from the steam-methane reforming that is not renewable. Aiming at green hydrogen, electrocatalytic water splitting is one of the most promising implementations [33]. To fabrication water splitting electrolyzer, we need to synthesize bifunctional catalysts for HER and OER.

Recently, transition metal compounds exhibit promising properties towards both HER and OER, such as transition metal phosphides/sulfides/oxides/nitrides/carbides [119,122,126,127,132,144]. The advantages of transition metal compounds are shown in the following: a) lower cost compared with noble metal-based materials [40]; b) optimal *d* electronic structure resulting in suitable adsorption energy towards reactants, intermediates, and products [39]; c) good flexibility to construct diverse nanostructures and morphologies in terms of different metal compounds; d) multiple active sites provided by the transition metals in the surface. Based on these properties, transition metal compounds such as CoP have been widely studied. Xiulin Yang and co-workers [165] fabricated CoP nanosheet assemblies supported on the carbon cloth for highly

efficient hydrogen generation, exhibiting a Tafel slope of 30.1 mV dec^{-1} in the acidic media, and the rugae-like nanosheet structure largely increased the active sites in the surface. Ting Feng and co-workers [155] reported a novel kind of heteronanoparticles CoP/Ni_2P with both Co and Ni active sites on the surface of transition metal compounds. The synergistic effect of these two metal phosphides and the dual sites enhanced the HER performance and exhibited a small Tafel slope of 53.01 mV dec^{-1} in the 0.5 M H_2SO_4. Furthermore, nickel sulfide is also a promising catalyst for water splitting. Deliang Zhang and co-workers [120] synthesized 2D NiS @ 2D graphene by one-step method and environment-friendly precursors. The heterostructure composites and the interface between NiS and graphene provided high surface-active sites and enhanced electrical conductivity.

Though transition metal compounds provide basic electrocatalytic activity and promising water splitting performance, and further improve the activity and stability of the catalysts by constructing heterostructures becomes more critical. For example, Pengyan Wang and coworkers [166] designed a novel synthesis route containing selenization and partial phosphating treatments to combine $NiSe_2$ and Ni_2P as heterostructures. The fabricated heterostructure improved the adsorption performance and accelerated the catalytic kinetics. Panlong Zhai and coworkers [167] developed a surface reconfiguration strategy to fabricate $NiMoO_x$/NiMoS heterostructure array and it exhibited relatively low overpotential and good stability at a large current density. The results demonstrated that this strategy successfully constructed an interface with active sites and enhanced the water splitting performance.

Herein, we propose a novel and facile method to construct a heterogeneous structure composite by using the elements Co, Ni, P, and S. Through the growth of nickel sulfides and cobalt-containing intermediates, followed by phosphorization, the as-prepared Co_2P-Ni_3S_2 heterogeneous structural hollow nanowires evenly grow on nickel foam (denotes as Co_2P-Ni_3S_2/NF). The Co_2P-Ni_3S_2/NF exhibits remarkable HER/OER performance, especially at a large current density over 500 mA cm^{-2}. It achieves the low overpotentials of 110, 164 mV for HER and 331.7, 358.3 mV for OER at 100, 500 mA

cm^{-2} in 1.0 M KOH. Moreover, the electrocatalytic performance maintains stable after testing 48 h at 100 mA cm^{-2} in 1.0 M KOH and it proves long-term durability under a practical working environment. A two-electrode electrolyzer using Co_2P-Ni_3S_2/NF demonstrates a cell voltage of 1.54 V at 10 mA cm^{-2} in alkaline electrolyte, with impressive long-term stability. The outstanding water splitting performance is attributed to the multiple active sites provided by cobalt phosphide and nickel sulfide, a synergistic effect of heterostructure interfaces, and the large surface area of the unique hollow nanowire morphology. This work proposes an effective synthetic method to take advantage of earth-abundant transition metal compounds with heterostructures and fabricate bifunctional water splitting electrocatalysts with remarkable electrocatalytic activity at large current density and long-term stability.

3.2 Experimental section

3.2.1 Chemicals

Cobalt (II) nitrate hexahydrate ($Co(NO_3)_2 \cdot 6H_2O$), nickel foam (NF), sodium sulfide (Na_2S), urea (NH_2CONH_2), ammonium fluoride (NH_4F), ethanol, sodium hypophosphite hydrate ($NaH_2PO_2 \cdot xH_2O$), deionized water (DI). All chemicals were used directly without any further purification.

3.2.2 Synthesis of Ni_3S_2/NF nanowires

Ni_3S_2/NF nanowires were synthesized by one-step hydrothermal method as follows: 400 mg Na_2S was dissolved in 50 mL DI under stirring to get uniform solution. One piece of clean nickel foam (size: 3 * 2 cm^2) was immersed into the as-prepared solution and reacted at 180 ℃ for 24 h in a 100-mL Taflon-lined stainless steel autoclave. After the hydrothermal process, the Ni_3S_2/NF was washed with DI and ethanol several times

and dried at 60 ℃ overnight.

3.2.3 Synthesis of Co_2P-Ni_3S_2/NF nanowires

The growth of Co_2P on the Ni_3S_2/NF nanowires can be divided into two steps. Firstly, 3.9 mmol $Co(NO_3)_2 \cdot 6H_2O$, 11.9 mmol urea, and 6 mmol NH_4F were dissolved in 40 mL DI under stirring to get uniform solution. One piece of as-synthesized Ni_3S_2/NF was immersed into the as-prepared solution and reacted at 120 ℃ for 4 h in a 100-mL Taflon-lined stainless steel autoclave. After cooling down, the sample was washed with DI and ethanol several times and dried at 60 ℃ overnight. Secondly, the phosphating process was performed in the tube furnace. The sample was put at the downstream side of the tube furnace and 0.6 g $NaH_2PO_2 \cdot xH_2O$ was put at the upstream side of the tube furnace. The furnace was heated to 300 ℃ at 5 ℃/min and maintained 300 ℃ for 2 h under nitrogen flow. After cooling down to room temperature, the Co_2P-Ni_3S_2/NF was successfully fabricated.

3.2.4 Material characterization

The microstructure and morphology of samples were observed by Zeiss Sigma field emission scanning electron microscopy (FESEM) at 5 kV. Transmission electron microscope (TEM) images, high-resolution TEM (HR-TEM) images, and elemental distribution mapping were captured via the JEM-ARM200CF at the accelerating voltage of 200 kV equipped with an energy dispersive spectrometer (EDS) at 300 kV. X-ray diffraction (XRD) was performed on the Rigaku Ultima IV with Cu Kα (λ = 1.54056 Å) as the radiation source. X-ray photoelectron spectroscopy (XPS) was characterized by a Kratos Axis (Ultra) spectrometer with an Al Kα X-ray source.

3.2.5 Electrochemical measurement

The electrochemical measurement for HER and OER catalytic activities were performed in a standard three-electrode system in 1 M KOH solution (pH = 13.8), in which a saturated calomel electrode (SCE) as the reference electrode, a graphite rod as the counter electrode, and the as-synthesized catalysts supported on nickel foam as the working electrode. Polarization curves were measured at a scan rate of 5 mV s^{-1}. The potential was further presented with *iR* compensation for both HER and OER performance tests to eliminate the potential difference of solution resistance (R_s). In this work, all potentials were converted to potentials versus the reversible hydrogen electrode (RHE) with the formula (Nernst equation): $E_{RHE} = E_{SCE} + 0.241 + 0.0591$ pH. The Tafel plots were constructed by the Tafel equation, $\eta = b \log j + a$, where η is the overpotential, j is the current density, b is the Tafel slope, and a is the intercept relative to the exchange current density. Electrochemical impedance spectroscopy (EIS) was recorded in a frequency range from 0.01 Hz to 100 kHz at open circuit potential with 5 mV amplitude and the measurements of samples were tested in 1.0 M KOH at -0.14 V and 1.56 V (vs. RHE) for HER and OER, respectively. The double-layer capacitance (C_{dl}) was assessed by the cyclic voltammetry curves measured in the potential range of 0.1 V (vs. RHE) to 0.3 V (vs. RHE), calculated by $C_{dl} = I / v$, where I is the charging current (mA cm^{-2}), and v is the scan rate (mV s^{-1}). The long-term stability test was carried out via the chronopotentiometry method. The overall water splitting performance was tested in a two-electrode system using as-obtained catalysts Co_2P-Ni_3S_2/NF, and the polarization curves were measured at a scan rate of 5 mV s^{-1} without *iR* compensation.

3.3 Fabrication procedure exploration

The fabrication procedure of the final product Co_2P-Ni_3S_2/NF has been changed several

times. To improve the electrocatalytic performance step by step, we have done some modifications, including the composition and order of the nanomaterials on the nickel foam base, the detailed phosphating procedure of the last fabrication step, and the fabrication area of the nickel foam base.

Here are the basic synthetic ideas for transition metal compounds. The transition metal compound Ni_3S_2 can be synthesized on the surface by a one-step hydrothermal method containing both Na_2S and nickel foam, which means the nickel foam served as both the nickel source and the supporting base. For the nickel source, we can also grow nickel species on the NF surface by hydrothermal reactions by using $Ni(NO_3)_2 \cdot 6H_2O$. When we synthesize cobalt-based compounds, we can use hydrothermal reactions with $Co(NO_3)_2 \cdot 6H_2O$ as a cobalt source to grow cobalt species on the surface. Besides, synthesizing ZIF-67 by room temperature reactions is also a good choice to grow cobalt species. Based on these synthetic methods, we have tried different synthetic procedures and arrangements of the transition metal compounds to construct the heterojunction structure. The phosphating process has been implemented for all the samples as the last step to improve the HER performance. We have prepared the following samples and tested the electrocatalytic performance: (1) Co_xP/NF. The fabrication involves the hydrothermal reaction to grow cobalt species on the surface and the phosphating process of furnace heating. (2) P/NF. It's one of the final counterpart samples only involving the phosphating of the bare nickel foam. (3) Co_xP-Ni_3S_2/NF. It's our target sample, and the fabrication procedure is shown in the experimental section. (4) P-Ni_3S_2/NF. The fabrication involves the hydrothermal reaction with Na_2S to form Ni_3S_2 on the surface and the phosphating process of furnace heating. (5) Ni_xP-Ni_3S_2/NF. The first step is to grow Ni_3S_2 on the surface by hydrothermal reactions, and then we used the second hydrothermal reaction with $Ni(NO_3)_2 \cdot 6H_2O$ to synthesize nickel species for further fabrication of Ni_xP by the phosphating process. (6) Co_xNi_yP-Ni_3S_2/NF. In the second hydrothermal reaction step, we used $Ni(NO_3)_2 \cdot 6H_2O$ and $Co(NO_3)_2 \cdot 6H_2O$ at the same time for the concurrent growth of Co_xNi_yP at the phosphating step. (7) ZIF-67 derived Co_xP-Ni_3S_2/NF. For the growth of cobalt species on the surface, we used room

temperature reaction to construct ZIF-67 frameworks containing the cobalt species, followed by the phosphating process. (8) Hybrid Co_xP-Ni_3S_2/NF. We can fabricate hybrid cobalt species on the surface of both ZIF-67-derived and hydrothermal-derived ones. The electrocatalytic HER/OER performance is shown in **Figure 17-24**. The data is at an early stage and the potential is without *iR* compensation. We can compare the relative values of the electrocatalytic performance to decide the following fabrication procedure.

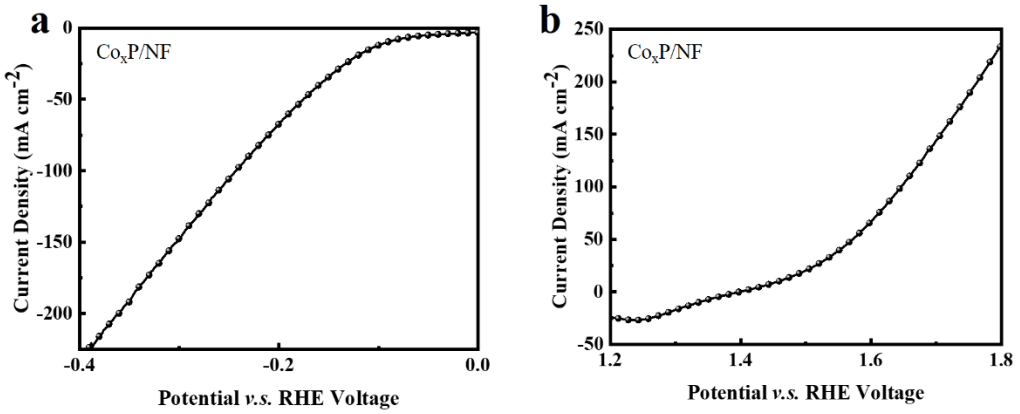

Figure 17. LSV curves of Co_xP/NF for (a) HER performance, (b) OER performance.

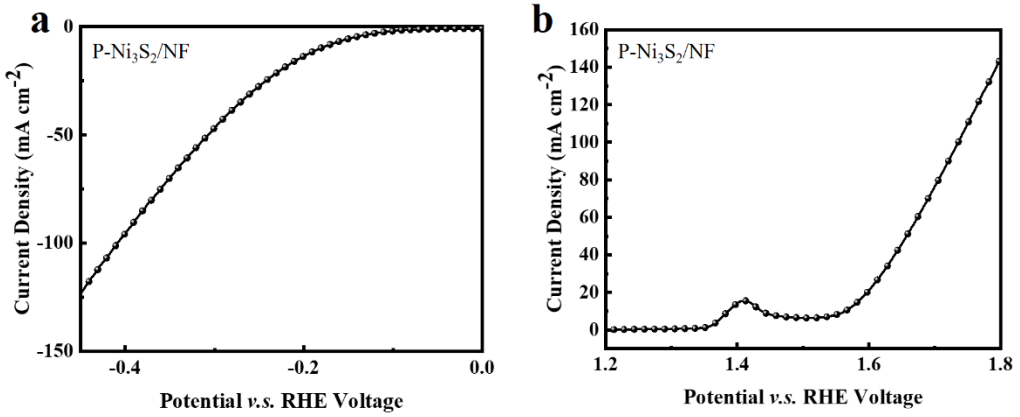

Figure 18. LSV curves of P-Ni_3S_2/NF for (a) HER performance, (b) OER performance.

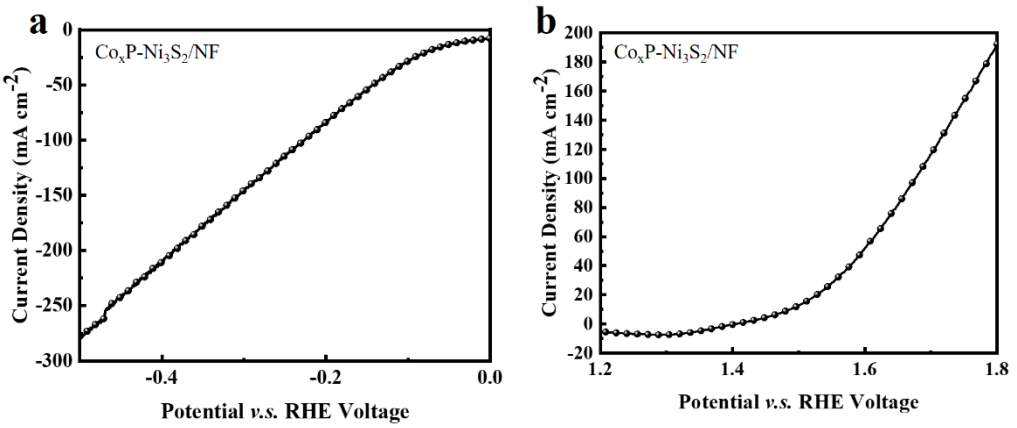

Figure 19. LSV curves of Co_xP-Ni_3S_2/NF for (a) HER performance, (b) OER performance.

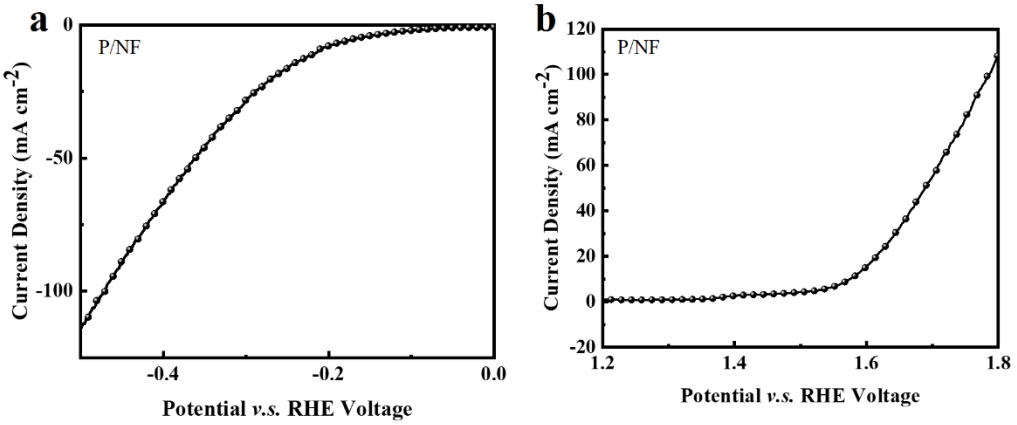

Figure 20. LSV curves of P/NF for (a) HER performance, (b) OER performance.

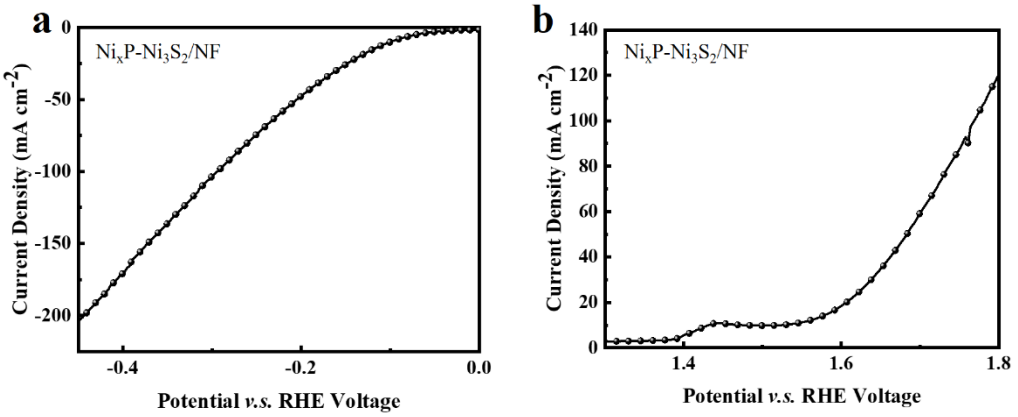

Figure 21. LSV curves of Ni_xP-Ni_3S_2/NF for (a) HER performance, (b) OER

performance.

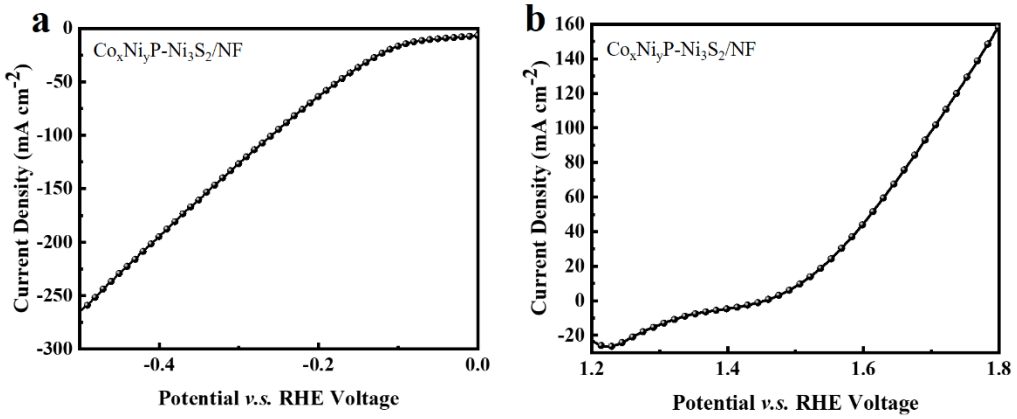

Figure 22. LSV curves of Co_xNi_yP-Ni_3S_2/NF for (a) HER performance, (b) OER performance.

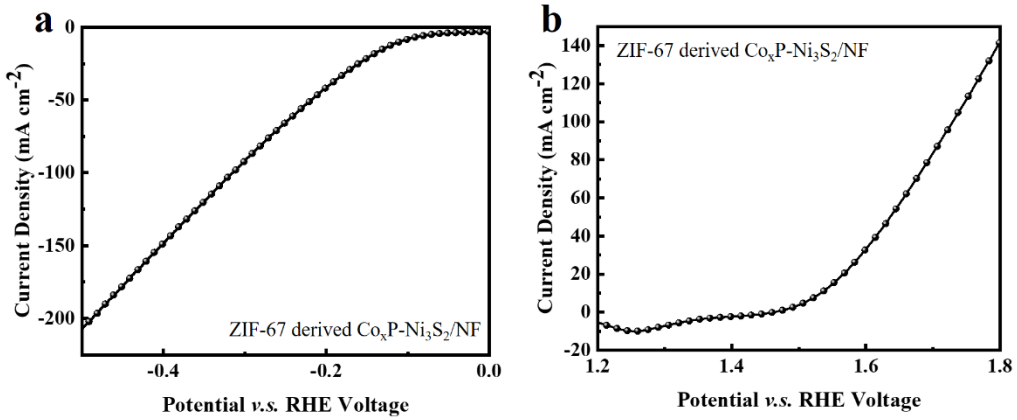

Figure 23. LSV curves of ZIF-67 derived Co_xP-Ni_3S_2/NF for (a) HER performance, (b) OER performance.

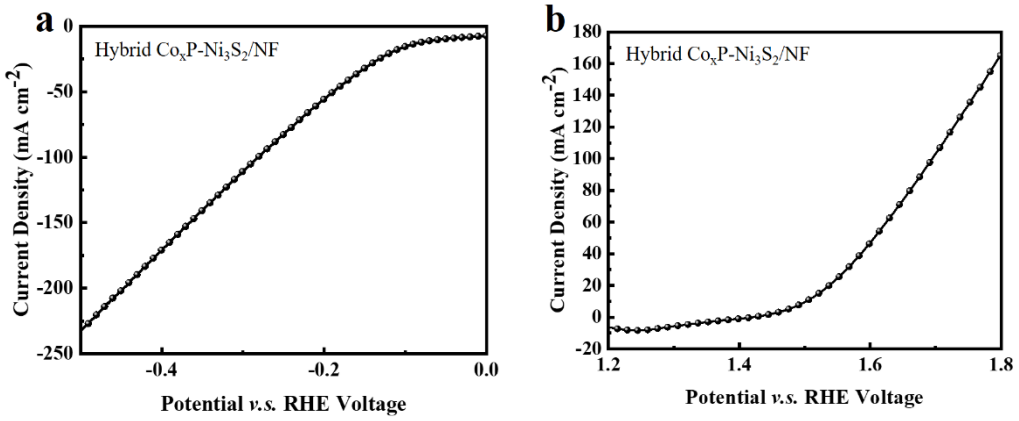

Figure 24. LSV curves of hybrid Co_xP-Ni_3S_2/NF for (a) HER performance, (b) OER performance.

We can evaluate the electrocatalytic performance and sort it as follows: Co_xP-Ni_3S_2/NF, Co_xP/NF, Co_xNi_yP-Ni_3S_2/NF, hybrid Co_xP-Ni_3S_2/NF, Ni_xP-Ni_3S_2/NF, ZIF-67 derived Co_xP-Ni_3S_2/NF, P-Ni_3S_2/NF, P/NF. Among the different samples, the best one is the CoP-Ni_3S_2/NF, and its synthesis route is the vulcanization of nickel foam and the growth of cobalt species on the surface, followed by the phosphating process. If I add some nickel source like $Ni(NO_3)_2 \cdot 6H_2O$ with cobalt, the final material is Co_xNi_yP-Ni_3S_2/NF and it shows a little bit lower performance compared to the original one. This result demonstrates that the growth of nickel phosphide occupies some active sites of cobalt phosphide, and the intrinsic activity of nickel phosphide is lower, thus decreasing the overall HER and OER performance. The performance of hybrid Co_xP-Ni_3S_2/NF is worse than that of the sample CoP-Ni_3S_2/NF and it could result from the same reason. The ZIF-67 framework-derived synthesis could lead to the growth of cobalt carbide after the furnace heating process, and its intrinsic activity for HER/OER is worse than the cobalt phosphide. The result also shows that the intrinsic activity of nickel phosphide is better than carbonized ZIF-67 framework after the furnace heating process because the performance of Co_xNi_yP-Ni_3S_2/NF is better than that of hybrid Co_xP-Ni_3S_2/NF and also the performance of Ni_xP-Ni_3S_2/NF is better than that of ZIF-67 derived Co_xP-Ni_3S_2/NF. The addition of Ni_3S_2 indeed improved the HER performance by comparing the performance between Co_xP/NF and Co_xP-Ni_3S_2/NF, and also between

P/NF and P-Ni_3S_2/NF.

Based on the initial objective, my plan is to design a facile synthetic strategy to fabricate multifunctional electrocatalysts. Considering both the electrocatalytic performance and synthetic routes, the sample Co_xP-Ni_3S_2/NF has pretty good intrinsic activity and needs three steps to be synthesized on the NF surface, including the vulcanization of nickel foam, the growth of cobalt species on the surface, and the phosphating process. Then, we adjusted the detailed fabrication procedures like the temperature of the hydrothermal reactions, the mass of phosphorus source NaH_2PO_2, and the ramp rate for the phosphating process. **Figure 25** shows the influence of phosphorus source mass on the electrocatalytic performance. The sample with 0.6 g NaH_2PO_2 in the phosphating process exhibits similar HER performance and much better OER performance compared with the sample with 1.2 g NaH_2PO_2.

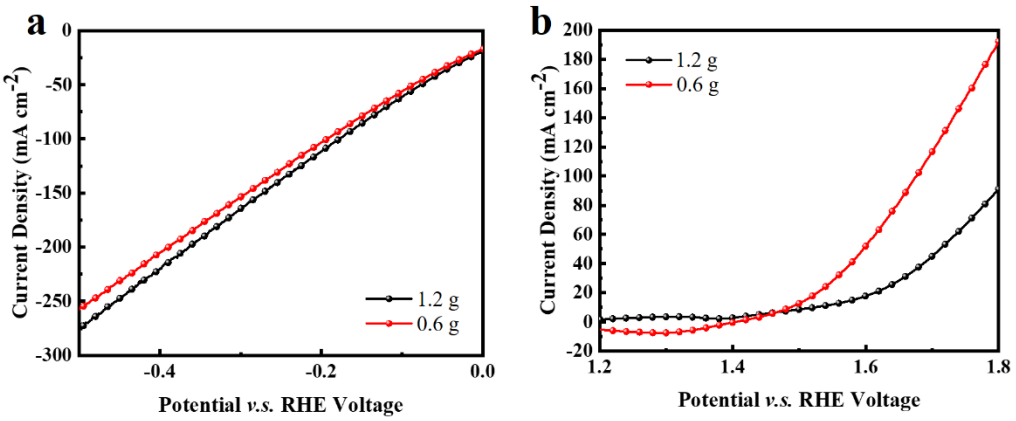

Figure 25. LSV curves of Co_xP-Ni_3S_2/NF sample with different phosphorus source mass for (a) HER performance, (b) OER performance.

3.4 Results and discussion

3.4.1 Structure characterization

The morphology and elemental composition of the Co_2P-Ni_3S_2/NF were characterized by scanning electron microscope (SEM), low magnification transmission electron

microscopy (TEM), high-resolution transmission electron microscopy (HRTEM), and energy-dispersive X-ray spectroscopy (EDS). As shown in **Figure 26a-d**, the Co_2P-Ni_3S_2/NF exhibits a nanowire structure uniformly grown on the nickel foam. The tip diameter of a single nanowire is less than 150 nm and the length of the nanowires is more than 10 μm, exhibiting smaller diameter and larger length than the that of P-Ni_3S_2/NF and P/NF (**Figure 27**, **28**), resulting in greater surface area and larger number of active sites. The uniform and dense nanowires grow in diverse directions and cover the entire base, indicating increased contact with the electrolyte and adequate mass/charge transfer at large current density. The structure also shows some gap regions under the numerous nanowires (**Figure 26d**) and provides enough space to expose the root of nanowires, enhancing the active sites' exposure near the nickel foam base. The SEM image of P/NF in **Figure 28d** shows the incomplete growth of the nanowires and some bare nickel foam surface area, indicating the following fabrication of Ni_3S_2 and Co_2P benefits the formation of uniform nanowires. Elemental mapping images in **Figure 29** display the uniform elemental distribution in the Co_2P-Ni_3S_2/NF surface. A large amount of Co and P elements on the surface indicates the formation of Co_2P in the last synthetic step, which can be further verified by HRTEM and X-ray diffraction patterns. The O element in the surface originates from the surface oxidation in the air.

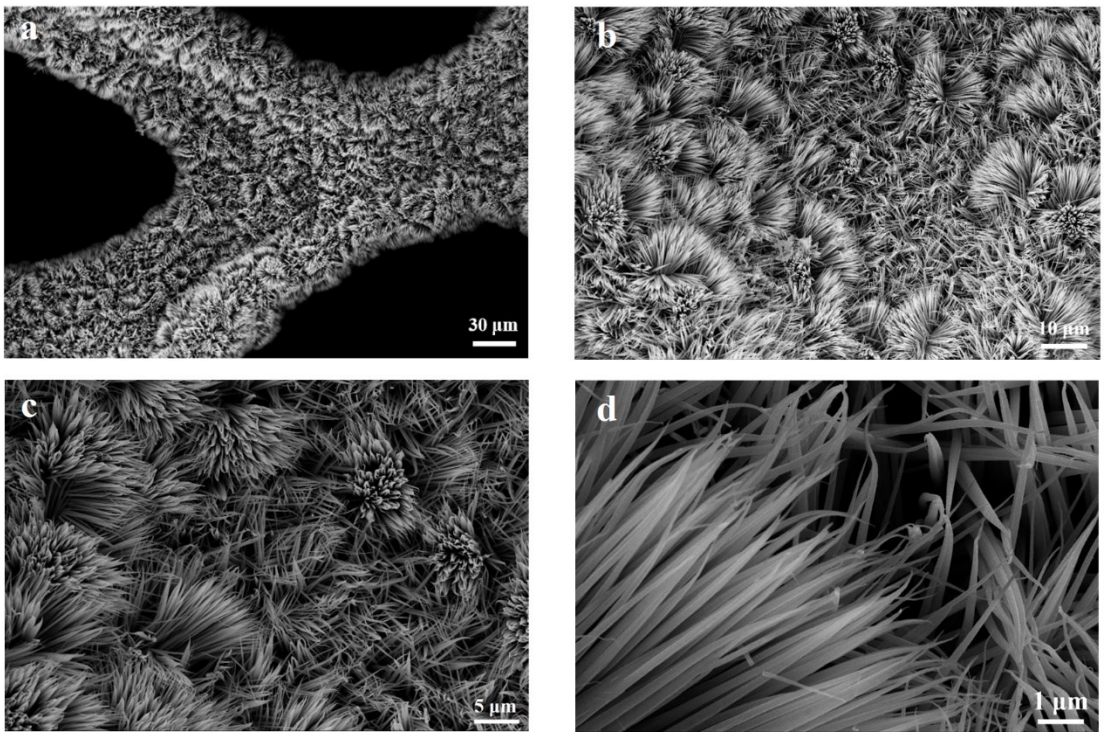

Figure 26. SEM images of Co_2P-Ni_3S_2/NF with scale bar of (a) 30 μm, (b) 10 μm, (c) 5 μm, and (d) 1 μm.

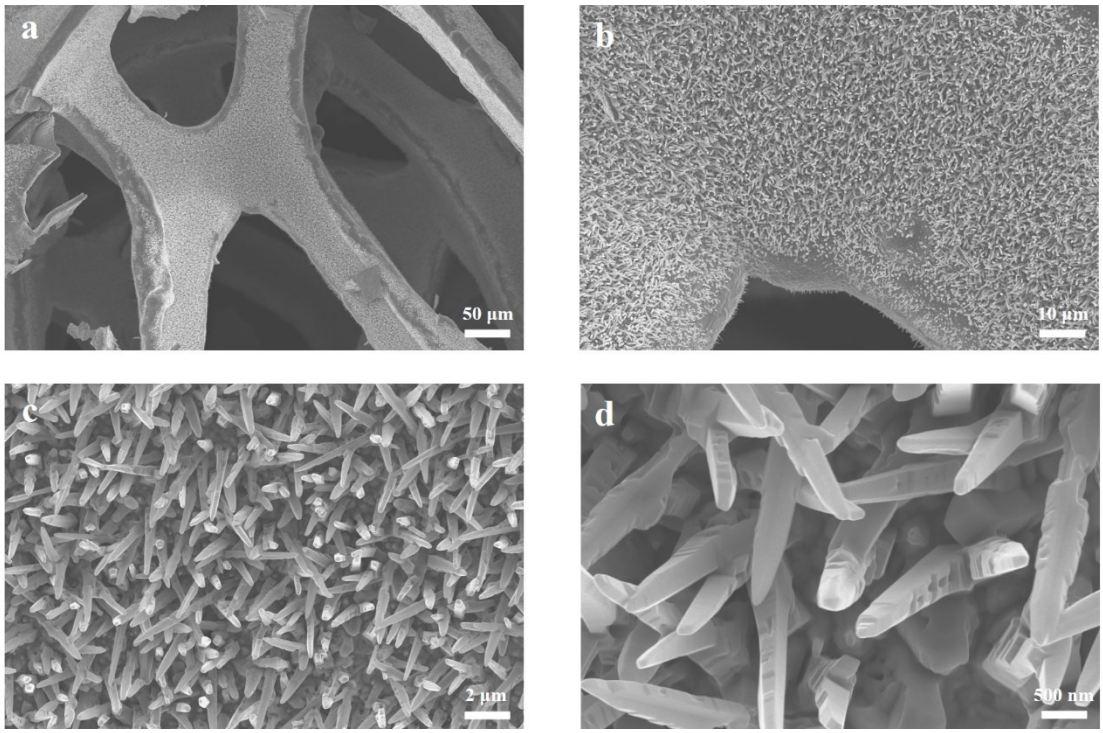

Figure 27. SEM images of P-Ni_3S_2/NF with scale bar of (a) 50 μm, (b) 10 μm, (c) 2 μm, and (d) 500 nm.

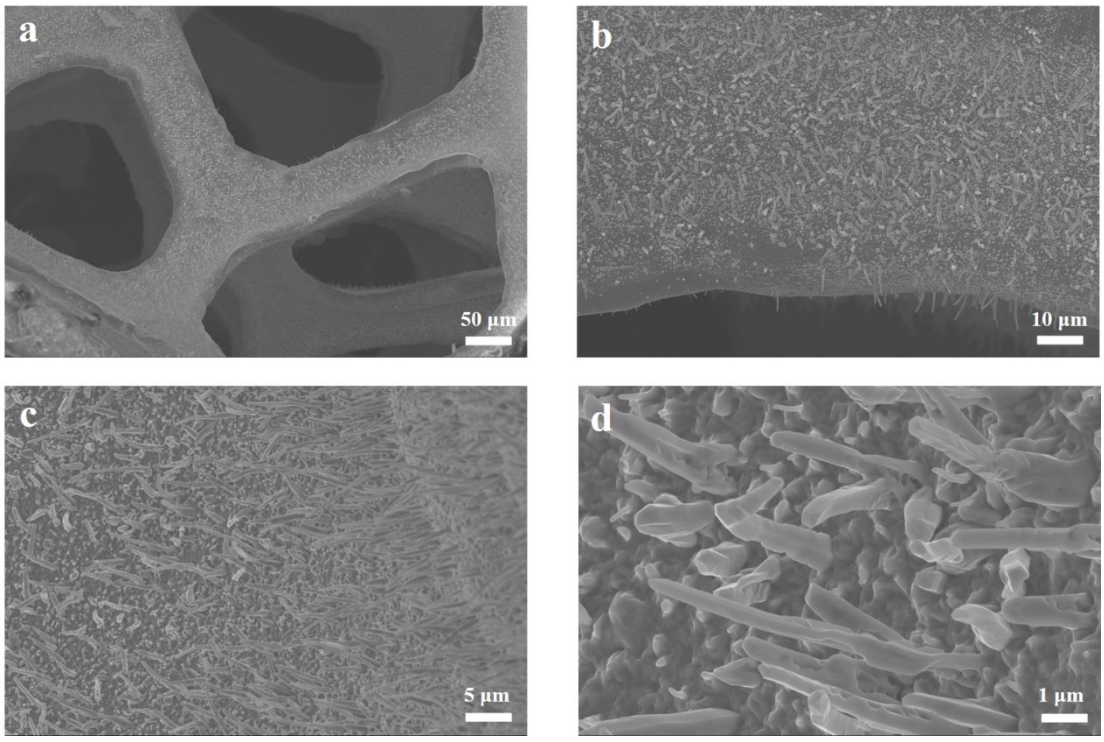

Figure 28. SEM images of P/NF with scale bar of (a) 50 μm, (b) 10 μm, (c) 5 μm, and (d) 1 μm.

From the TEM images of the Co_2P-Ni_3S_2/NF (**Figure 30a-c**), both Co_2P and Ni_3S_2 can be observed. The element distributions near the edge of nanowires could largely enhance the atom utilization, which can be further proved by elemental mappings in **Figure 30d**. The lattice spacing in **Figure 30b-c** reveals the presence of Co_2P, Ni_3S_2, and the interface in the heterojunction. Specifically, the lattice fringes of 0.209 nm, 0.187 nm, and 0.288 nm are corresponded to the (211) and (031) planes of Co_2P, (110) plane of Ni_3S_2, respectively. The red dotted line shows the interface between Co_2P crystal planes and Ni_3S_2 crystal planes, suggesting the presence of the heterojunction structure. EDS elemental mapping images in **Figure 30d** further indicate the concurrent presence of Co, Ni, S, and P, and suggest the uniform distribution of these elements as well.

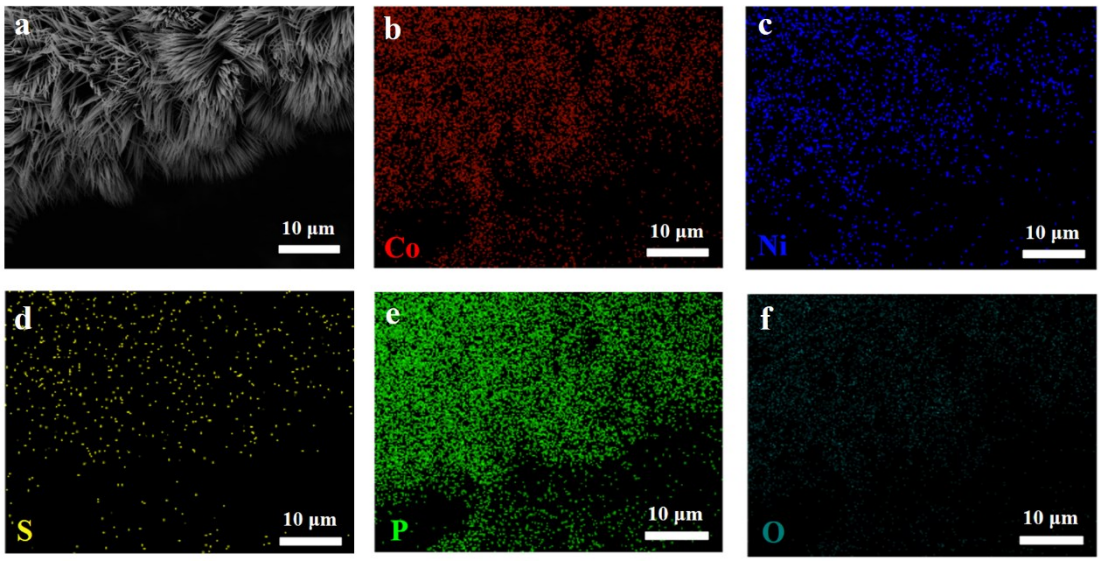

Figure 29. (a) SEM image of Co_2P-Ni_3S_2/NF, and corresponding elemental mapping images for (b) Co, (c) Ni, (d) S, (e) P, and (f) O.

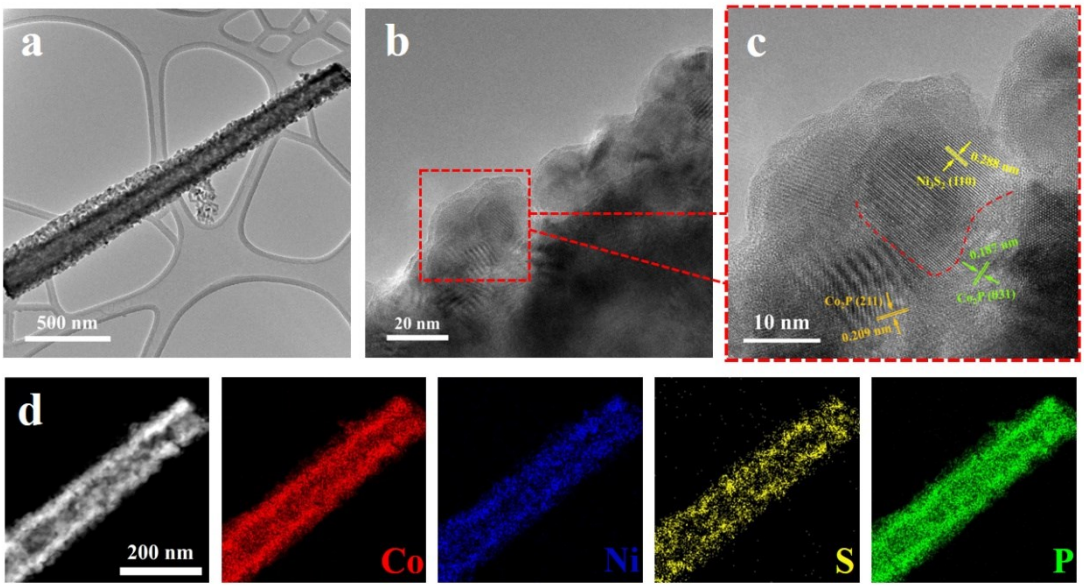

Figure 30. (a) TEM image and (b, c) HRTEM images of Co_2P-Ni_3S_2/NF. (d) TEM-EDX elemental mapping images of Co, Ni, S, P elements in Co_2P-Ni_3S_2/NF.

To further identify the crystalline structure and composition, the X-ray diffraction patterns (XRD) of synthesized samples are revealed in **Figure 31**. According to PDF# 04-0850, the diffraction peaks located at 44.5°, 51.8°, and 76.3°, correspond to the (111), (200), and (220) planes of Ni foam. These three diffraction peaks with strong intensity

exist in all samples, indicating the exposure of Ni crystal planes on the surface. After the phosphating process of bare Ni foam, the P/NF sample shows additional diffraction peaks at 40.8°, 44.6°, 47.3°, 54.2°, 54.9°, 66.2°, 72.7°, and 74.7°, corresponding to the (111), (201), (210), (300), (211), (310), (311), and (400) planes of Ni_2P (PDF# 03-0953). The (201) plane of Ni_2P overlaps with the (111) crystal plane of Ni foam with the peak at about 44.6°, and others exhibit unique characteristic peaks, indicating the successful phosphating on the Ni foam surface and the formation of Ni_2P. The P-Ni_3S_2/NF sample contains additional diffraction peaks at 31.1°, 44.3°, and 55.1°, corresponding to (110), (202), and (122) planes of Ni_3S_2 (PDF# 44-1418). At the same time, the diffraction peak intensity of Ni_2P decreases compared to the P/NF sample, indicating that the former sulfurization process occupies partial Ni first and leaves partial Ni for the following reactions. For the Co_2P-Ni_3S_2/NF sample, two unique characteristic peaks at 43.3° and 48.7° verify the growth of Co_2P after the final synthesis step, and they correspond to the (211) and (031) planes of Co_2P (PDF# 32-0306), respectively.

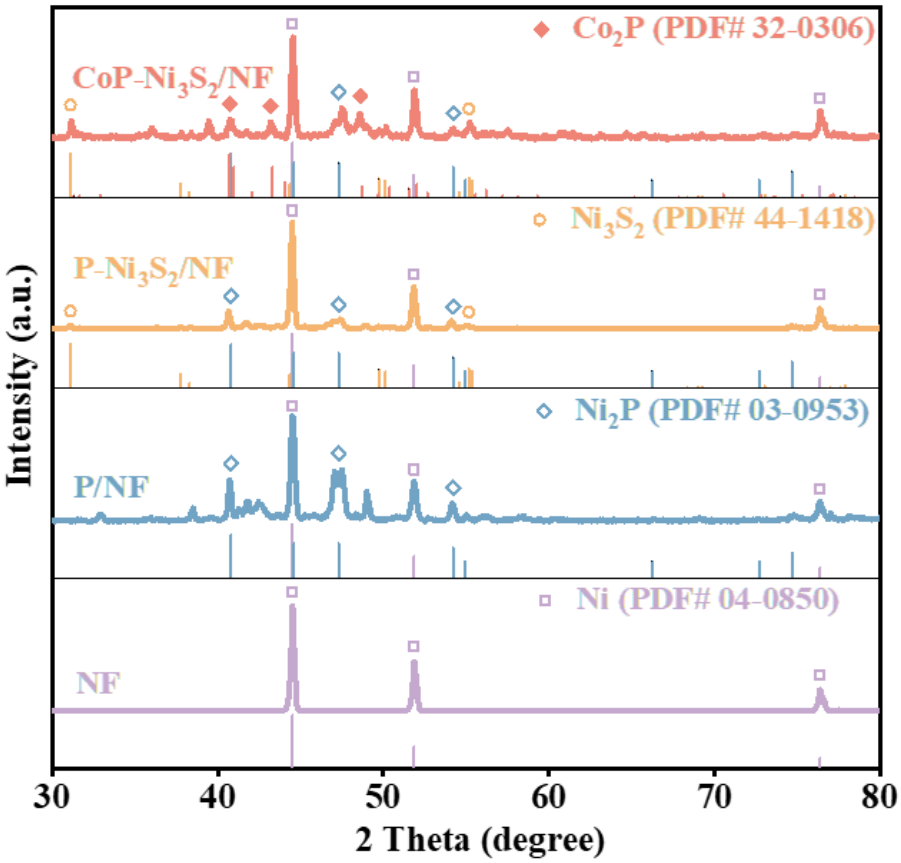

Figure 31. XRD patterns of Co_2P-Ni_3S_2/NF, P-Ni_3S_2/NF, P/NF and bare NF.

The surface elemental compositions and electronic states of Co_2P-Ni_3S_2/NF are probed by X-ray photoelectron spectroscopy (XPS). The high-resolution spectra for each elemental are displayed in **Figure 32a-d**. The amount of oxygen in the Co_2P-Ni_3S_2/NF material originates from the surface oxidation exposed in the air. The Co 2p spectrum in **Figure 32a** indicates the existence of two strong peaks related to Co $2p_{3/2}$ and Co $2p_{1/2}$ states. Specifically, the peaks located at 778.6 eV (Co $2p_{3/2}$) and 793.7 eV (Co $2p_{1/2}$) belong to $Co^{\delta+}$ in Co_2P [110,112], while the peaks located at 780 eV (Co $2p_{3/2}$) and 795.1 eV (Co $2p_{1/2}$) belong to oxidized Co species [113] due to the surface oxidation in air [112]. The left two peaks located at 782.5 eV (Co $2p_{3/2}$) and 797.6 eV (Co $2p_{1/2}$) correspond to the shake-up satellite peaks [110,113]. In **Figure 32b**, the P 2p spectrum is composed of three peaks. The peak located at 132.4 eV corresponds to the P-O bond

owing to the surface oxidation of Co_2P-Ni_3S_2/NF exposed in the air [112], while the other two peaks located at 129.3 eV and 130.2 eV are attributed to P $2p_{3/2}$ and $2p_{1/2}$, respectively [110]. In **Figure 32c**, the two main peaks located at 855.5 eV (Ni $2p_{3/2}$) and 873.7 eV (Ni $2p_{1/2}$) correspond to Ni^{3+}, while the two peaks located at 853.2 eV (Ni $2p_{3/2}$) and 871.6 eV (Ni $2p_{1/2}$) correspond to Ni^{2+} [120,126]. In **Figure 32d**, the S 2p spectrum is fitted into two peaks located at 160.5 eV (S $2p_{3/2}$) and 163.5 eV (S $2p_{1/2}$) belonging to the Ni–S bond [120], which confirms the formation of Ni–S bond during the sulfurization process [126]. The contact angle (CA) measurement in **Figure 33** suggests that the sulfurization process successfully reduces the contact angle to 0° and makes the P-Ni_3S_2/NF, and Co_2P-Ni_3S_2/NF samples hydrophilic. This wettable surface can accelerate mass transfer and largely promote electrocatalytic performance.

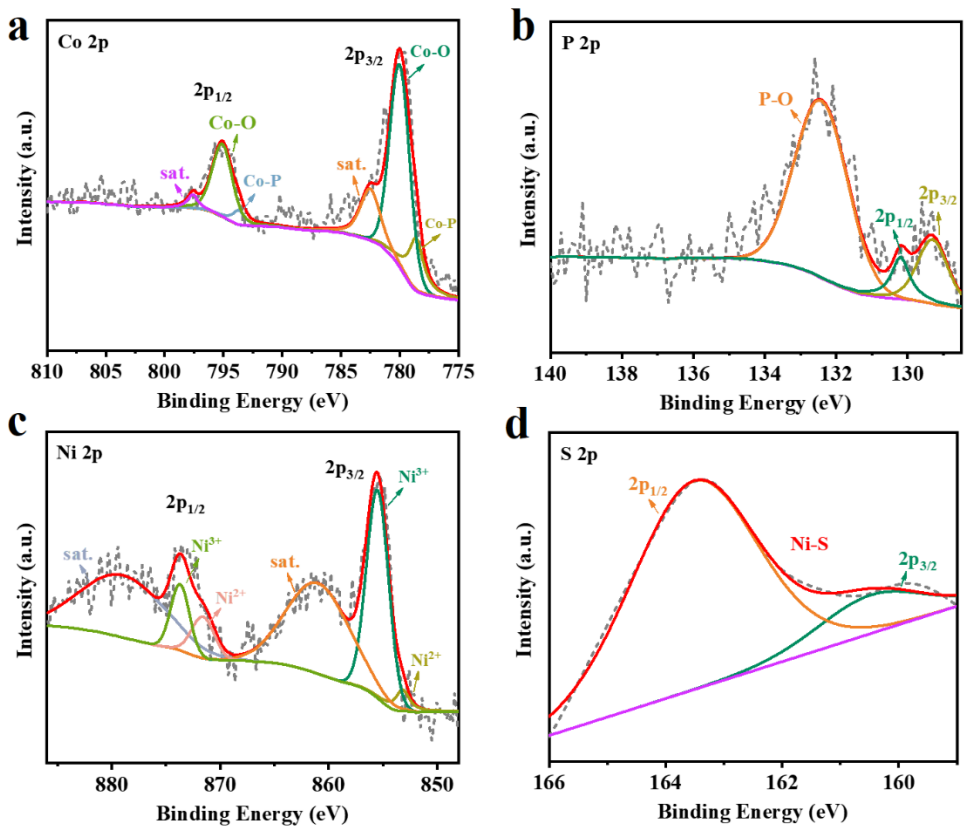

Figure 32. High-resolution XPS spectra of Co_2P-Ni_3S_2/NF for (a) Co 2p, (b) P 2p, (c) Ni 2p, (d) S 2p.

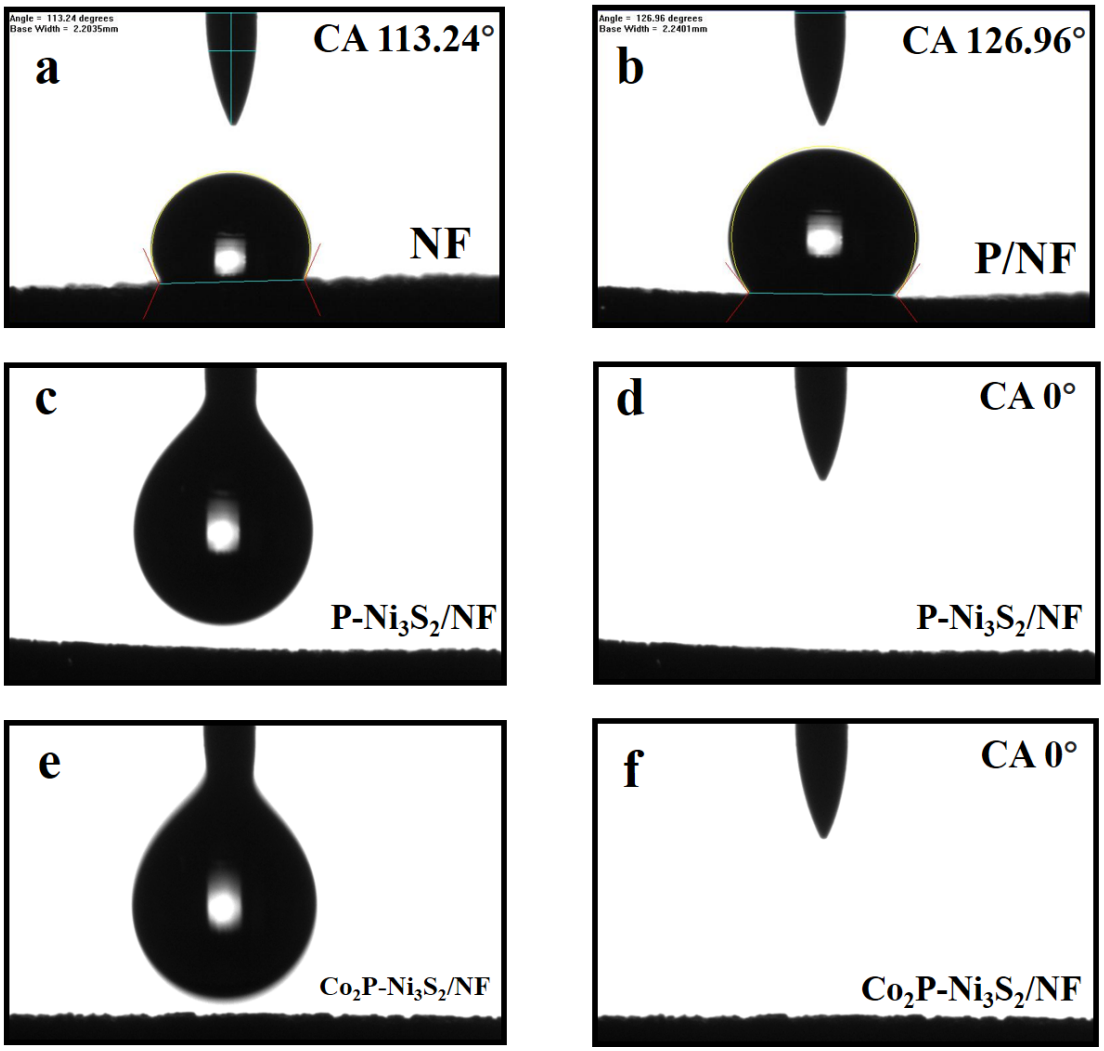

Figure 33. Contact angle measurement with 1.0 M KOH aqueous solution droplets. (a) Bare NF. (b) P/NF. (c, d) P-Ni_3S_2/NF. (e, f) Co_2P-Ni_3S_2/NF.

3.4.2 Electrocatalytic performance for HER and OER

The HER performance of Co_2P-Ni_3S_2/NF is examined in 1.0 M KOH electrolyte with a traditional three-electrode setup. As displayed in **Figure 34a**, the obtained Co_2P-Ni_3S_2/NF exhibits ultralow overpotentials compared to the samples of P-Ni_3S_2/NF, P/NF, and bare NF at the whole range of current density from 0 to 1000 mA cm^{-2}. Specifically, the Co_2P-Ni_3S_2/NF achieves 100, 500, and 1000 mA cm^{-2} by small overpotential values of 110, 164, and 196 mV, while the P-Ni_3S_2/NF requires 262, 385 mV to drive 100, 500 mA cm^{-2}, the P/NF requires 312, 494 mV to drive 100, 500 mA

cm^{-2}, and the bare NF requires 373, 556 mV to drive 100, 500 mA cm^{-2}. The commercial 20%wt Pt/C supported on NF shows better catalytic activity at the small current density below 250 mA cm^{-2} (η_{100} = 69 mV, η_{250} = 143 mV, η_{500} = 240 mV), while the electrocatalytic performance of Co_2P-Ni_3S_2/NF grows rapidly with the increase of current density, indicating the enhanced large-current-density performance of the Co_2P-Ni_3S_2/NF catalyst. The column graph in **Figure 34b** shows the HER performance comparison between commercial 20%wt Pt/C NF, Co_2P-Ni_3S_2/NF, P-Ni_3S_2/NF, P/NF, and bare NF. To further study the reaction kinetics of these samples, the corresponding Tafel plots are performed by LSV curves in **Figure 34c**. Tafel slope is an important kinetic parameter to explore the electrocatalytic performance, and a smaller Tafel slope indicates faster kinetics for an electrochemical reaction involving charge transfer. The enhanced HER performance of Co_2P-Ni_3S_2/NF is further confirmed by its Tafel slope of 114.2 mV dec^{-1}, which is much smaller than that of P-Ni_3S_2/NF (131.5 mV dec^{-1}), P/NF (169.1 mV dec^{-1}), and bare NF (165.9 mV dec^{-1}), indicating its accelerated kinetics for HER in 1.0 M KOH electrolyte.

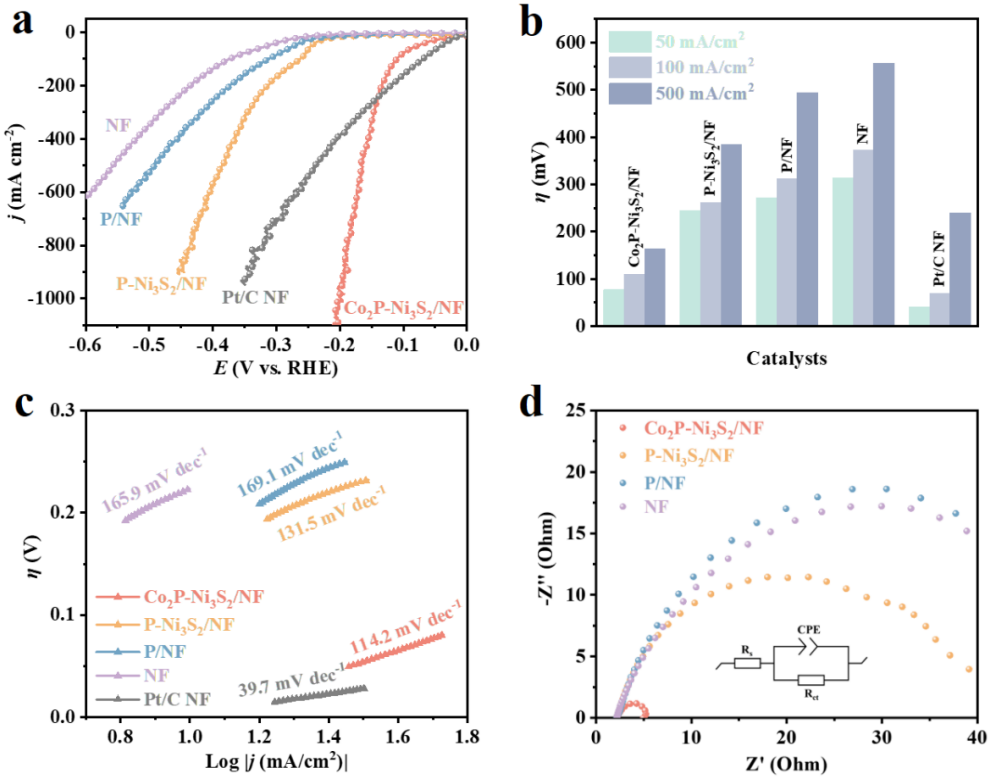

Figure 34. HER performance of samples in 1.0 M KOH. (a) Polarization curves, (b)

overpotentials, and (c) Tafel slopes of Co_2P-Ni_3S_2/NF, P-Ni_3S_2/NF, P/NF, bare NF, and 20%wt Pt/C NF. (d) Nyquist plots of Co_2P-Ni_3S_2/NF, P-Ni_3S_2/NF, P/NF, and bare NF.

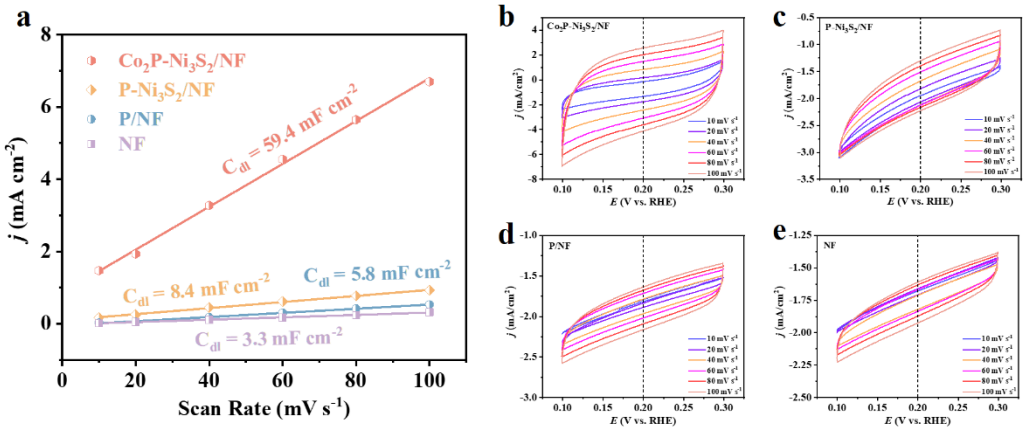

Figure 35. (a) C_{dl} values of Co_2P-Ni_3S_2/NF, P-Ni_3S_2/NF, P/NF, and bare NF. CV curves at the non-Faradic potential scope of (b) Co_2P-Ni_3S_2/NF, (c) P-Ni_3S_2/NF, (d) P/NF, and (e) bare NF.

To estimate the ECSA values of the samples, the electrochemical double-layer capacitance (C_{dl}) in a non-faradic region is measured via cyclic voltammetry with different scan rates. The C_{dl} is considered to be linearly proportional to the electrode ECSA. As shown in **Figure 35a**, the C_{dl} values of the samples, derived from CV curves at the non-Faradic potential scope in **Figure 35 b-e**, increase with every synthesis step, from bare NF (C_{dl} = 3.3 mF cm^{-2}), to P/NF (C_{dl} = 5.8 mF cm^{-2}), to P-Ni_3S_2/NF (C_{dl} = 8.4 mF cm^{-2}), then to Co_2P-Ni_3S_2/NF (C_{dl} = 59.4 mF cm^{-2}), indicating the increasing ECSA and more active sites step by step of transition metal compounds' growth. Also, the large C_{dl} value gap between Co_2P-Ni_3S_2/NF and the other three samples indicates that the introduction of Co_2P and the construction of heterogeneous structure have greatly enlarged the active site exposure. Electrochemical impedance spectroscopy (EIS) provides insights into the intrinsic charge transport properties and the catalytic kinetics. The EIS measurements of samples are tested in 1.0 M KOH at 0.14 V vs. RHE, shown in **Figure 34d**. The smallest charge transfer resistance (R_{ct}) value of Co_2P-Ni_3S_2/NF (R_{ct} = 3.28 Ω) compared with P-Ni_3S_2/NF (R_{ct} = 36.2 Ω), P/NF (R_{ct} = 53.4

Ω), and bare NF (R_{ct} = 54.2 Ω), attributes to the improved charge transfer kinetics. The intrinsic properties such as low resistance and large electrochemical active surface area (ECSA), contribute to the enhanced HER electrocatalytic activity of Co_2P-Ni_3S_2/NF. The heterogeneous structure constructed by the transition metal compounds modifies the electronic structure and synergistically contributes to the rapid catalytic kinetics.

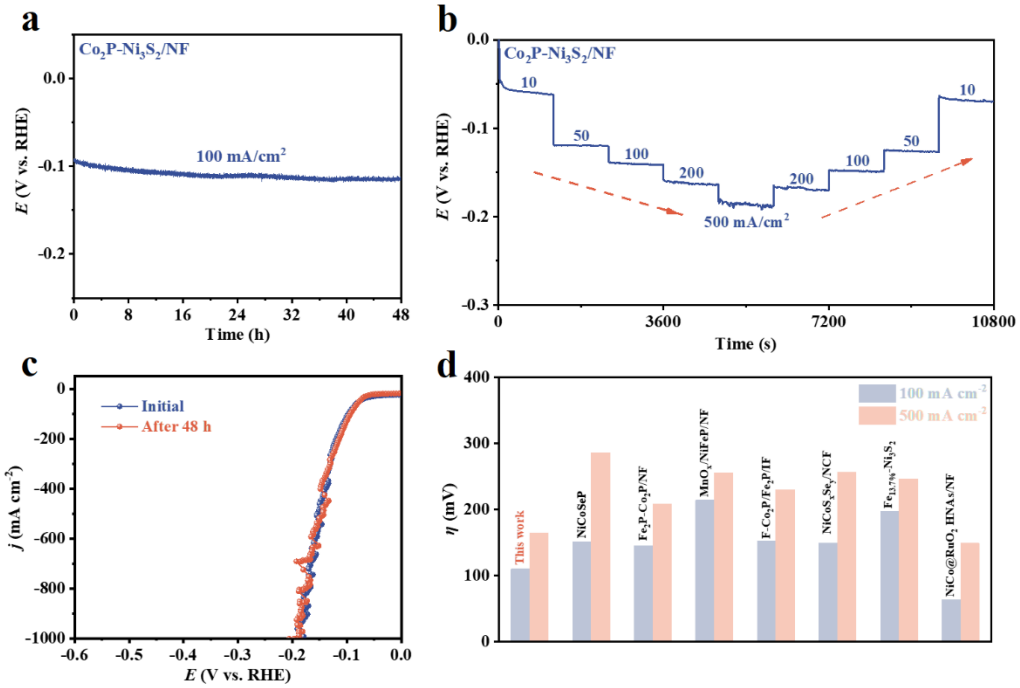

Figure 36. HER stability test of samples in 1.0 M KOH. (a) Long-term stability test of Co_2P-Ni_3S_2/NF at -100 mA cm^{-2} for 48 h. (b) Multi-step chronopotentiometric curves of Co_2P-Ni_3S_2/NF. (c) Polarization curves before and after 48 h stability test. (d) Summarized overpotentials of other reported transition metal compound-based HER electrocatalysts working at 100 mA cm^{-2} and 500 mA cm^{-2}.

The durability of Co_2P-Ni_3S_2/NF is evaluated via chronopotentiometric curves and the sample maintains stable electrocatalytic HER working at the current density of 100 mA cm^{-2} for 48 h. As shown in **Figure 36a**, the overpotential only shows a tiny increase during the stability test. The LSV comparison between the initial state and working after 48 h in **Figure 36c** exhibits the excellent long-term stability of Co_2P-Ni_3S_2/NF. To further investigate the durability in practical work, the multi-step chronopotentiometric

curve is obtained in 1.0 M KOH. The Co_2P-Ni_3S_2/NF works in a wide current density range from 10 mA cm^{-2} to 500 mA cm^{-2}, then returns to 10 mA cm^{-2}. Unlike the continuous current density change in the LSV curves, the step change of gradient current density requires mass transfer properties to deal with the reactants' adsorption and the products' release. The symmetric curve shown in **Figure 36b** indicates the efficient mass diffusion and charge transfer in the dynamic process. As shown in **Figure 36d**, **Table 1**, and **Table 3**, the Co_2P-Ni_3S_2/NF exhibits superior HER activity compared with other reported transition metal compound catalysts. Above results clearly demonstrates that the introduction of multiple transition metal compounds and the construction of a Co_2P/Ni_3S_2 heterogeneous structure successfully expose more active sites on the surface, increase the mass diffusion and charge transfer, and enhance the intrinsic activity towards HER.

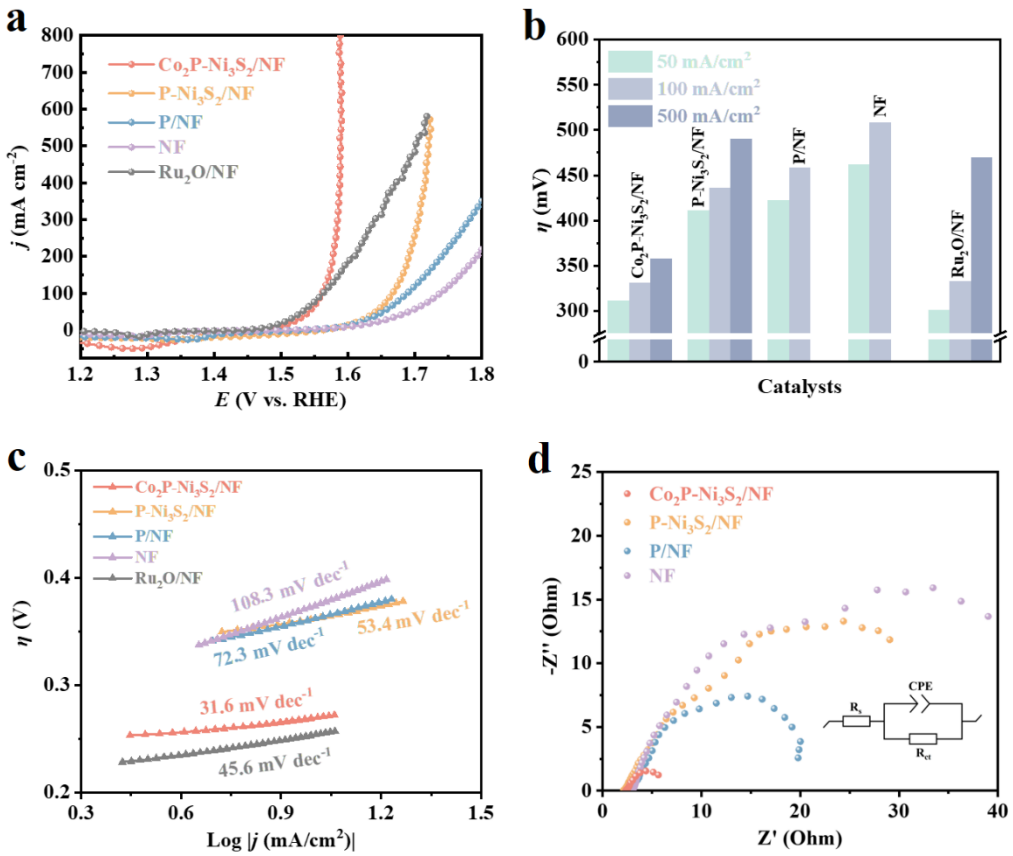

Figure 37. OER performance of samples in 1.0 M KOH. (a) Polarization curves, (b) overpotentials, and (c) Tafel slopes of Co_2P-Ni_3S_2/NF, P-Ni_3S_2/NF, P/NF, bare NF, and 20%wt Pt/C NF. (d) Nyquist plots of Co_2P-Ni_3S_2/NF, P-Ni_3S_2/NF, P/NF, and bare NF.

To investigate the bifunctional properties of Co_2P-Ni_3S_2/NF, the OER performance is further assessed in 1.0 M KOH electrolyte. As shown in **Figure 37a**, the Co_2P-Ni_3S_2/NF exhibits outstanding activity and an ultralow overpotential of about 332 mV at 100 mA cm^{-2}, which is smaller than that of P-Ni_3S_2/NF (436 mV), P/NF (458 mV), bare NF (508 mV), and Ru_2O/NF (333 mV). The Co_2P-Ni_3S_2/NF also shows promising activity toward large-current-density applications. It only requires an overpotential of 358 mV to obtain 500 mA cm^{-2}, which is far ahead of P-Ni_3S_2/NF (490 mV) and Ru_2O/NF (469 mV). **Figure 37b** shows the OER performance comparison between Ru_2O/NF, Co_2P-Ni_3S_2/NF, P-Ni_3S_2/NF, P/NF, and bare NF. The corresponding Tafel slopes of the tested samples are displayed in **Figure 37c**. The Co_2P-Ni_3S_2/NF exhibits the smallest Tafel slope of 31.6 mV dec^{-1} compared with Ru_2O/NF (45.6 mV dec^{-1}), P-Ni_3S_2/NF (53.4 mV dec^{-1}), P/NF (72.3 mV dec^{-1}), and bare NF (108.3 mV dec^{-1}), unraveling the accelerated reaction kinetics and better intrinsic activity of Co_2P-Ni_3S_2/NF in OER. The EIS results shown in **Figure 37d** demonstrate that Co_2P-Ni_3S_2/NF exhibits the smallest charge transfer resistance (R_{ct}) value of 4.86 Ω, compared with P-Ni_3S_2/NF (R_{ct} = 47.2 Ω), P/NF (R_{ct} = 22.4 Ω), and bare NF (R_{ct} = 45.7 Ω), indicating the lower resistance and accelerated electron transfer between electrocatalyst and electrolyte. The stability test of Co_2P-Ni_3S_2/NF is implemented by long-term and multi-step chronopotentiometry tests. **Figure 38c** exhibits an LSV comparison between the initial state and working after 48 h, where the two curves almost overlap each other. As shown in **Figure 38a**, during the 48 h electrocatalysis at a current density of 100 mA cm^{-2}, the catalyst maintains constant overpotential, implying good catalytic durability. **Figure 38b** presents a multi-step chronopotentiometric curve in a wide current density range from 10 to 500 mA cm^{-2}, then return to 10 mA cm^{-2}. The curve exhibits a stable performance for Co_2P-Ni_3S_2/NF working in the gradient current density with only a slight fluctuation at a large current density of 500 mA cm^{-2}. As shown in **Figure 38d**, **Table 2**, and **Table 4**, the as-synthesized Co_2P-Ni_3S_2/NF shows competitive OER performance compared with other reported transition metal compound catalysts.

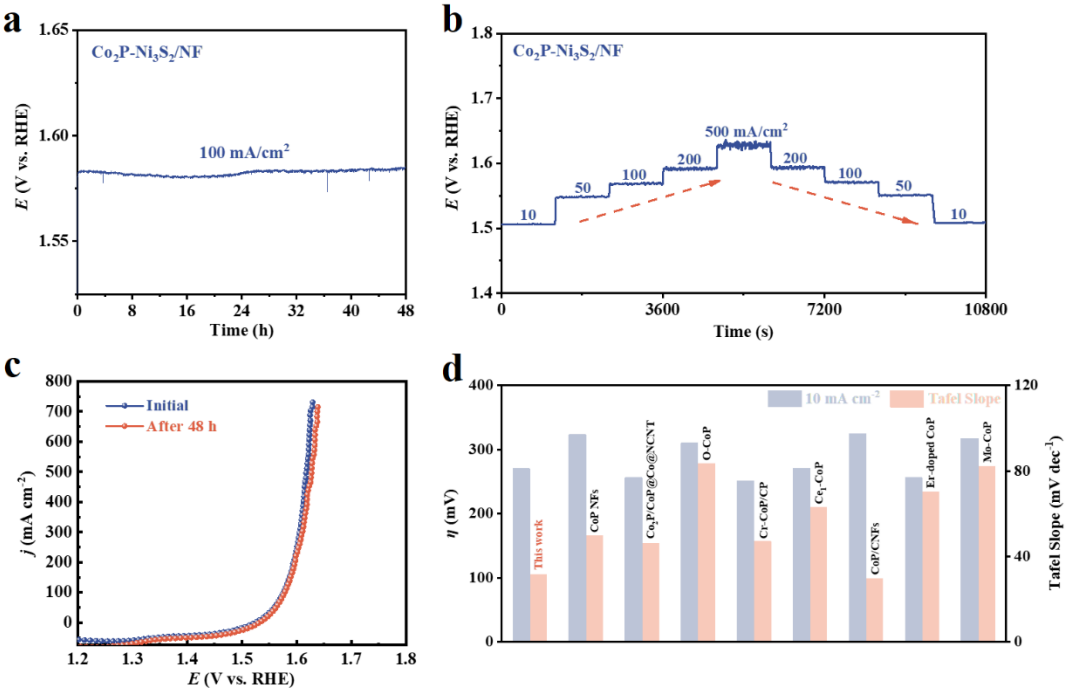

Figure 38. OER stability test of samples in 1.0 M KOH. (a) Long-term stability test of Co_2P-Ni_3S_2/NF at 100 mA cm^{-2} for 48 h. (b) Multi-step chronopotentiometric curves of Co_2P-Ni_3S_2/NF. (c) Polarization curves before and after 48 h stability test. (d) Summarized overpotentials and Tafel slope values of other reported transition metal compound-based OER electrocatalysts working at 10 mA cm^{-2}.

3.4.3 Electrocatalysis of water splitting

To further investigate the potential for practical applications, we use bifunctional Co_2P-Ni_3S_2/NF as two electrodes to assemble an alkaline electrolyzer for overall water splitting in alkaline medium (**Figure 39a**, **d**). As shown in **Figure 39b**, the Co_2P-Ni_3S_2/NF||Co_2P-Ni_3S_2/NF electrolyzer only requires a cell voltage of 1.54 V to afford 10 mA cm^{-2}, exhibiting admirable water splitting performance compared with other reported transition metal compound-based bifunctional electrocatalysts (**Figure 39e**, **Table 5**). To further measure the stability of overall water splitting, the Co_2P-Ni_3S_2/NF||Co_2P-Ni_3S_2/NF electrolyzer is examined in a long-term electrolysis test at a current density of 100 mA cm^{-2}, and the performance presents only slight damping after

24 h (**Figure 39c**), indicating the excellent durability of the bifunctional Co_2P-Ni_3S_2/NF electrocatalyst working at large current density for practical applications.

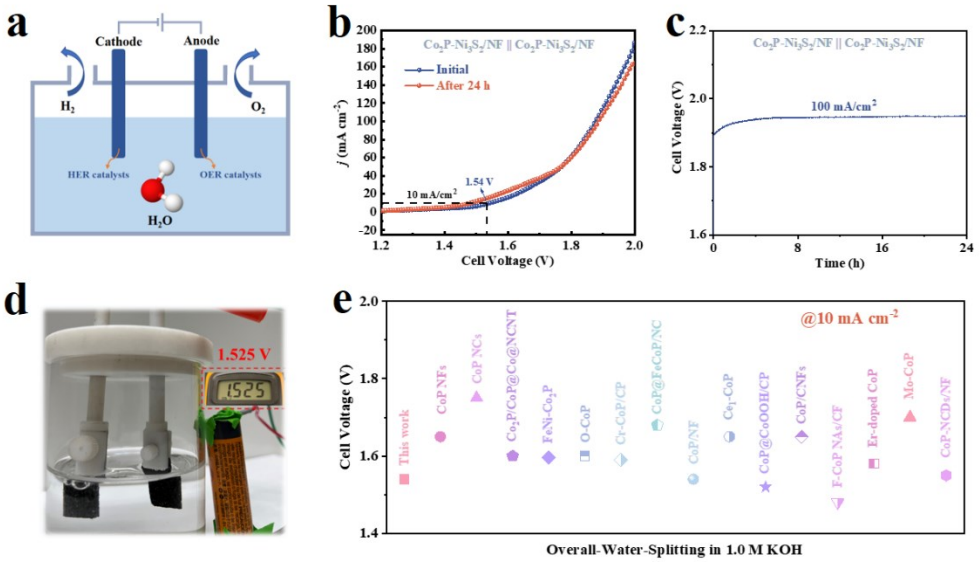

Figure 39. (a) Illustration of an electrolyzer for overall water splitting. (b) LSV curves of Co_2P-Ni_3S_2/NF||Co_2P-Ni_3S_2/NF electrolyzer before and after 24 h stability test in 1.0 M KOH without *iR* compensation. (c) Long-term stability test of Co_2P-Ni_3S_2/NF||Co_2P-Ni_3S_2/NF electrolyzer at 100 mA cm^{-2} for 24 h in 1.0 M KOH. (d) Digital photograph of the two-electrode cell. (e) Summarized cell voltages of other reported transition metal compound-based bifunctional catalysts to drive a current density of 10 mA cm^{-2}.

3.5 Future works

Although our target sample Co_2P-Ni_3S_2/NF could remain stable for HER/OER during the 48 h stability test and for overall water splitting during the 24 h stability test, there is still a large gap for practical applications. To further improve the durability in practical working conditions, we should focus on the growth of nanomaterials on the NF foam base. Nickel foam provides a stable base, resulting in intact self-supporting materials. However, the nanomaterials on the surface, serving as active sites for electrocatalysis, could be damaged or degraded into other nanomaterials during the

working conditions. **Figure 40** shows the SEM image of Co_2P-Ni_3S_2/NF after the electrocatalytic stability test. Compared with the SEM images before the stability test, surface deformation and nanomaterial aggregation are quite obvious. The length of the nanowires decreases and the surface aggregates to spherical morphology. These changes will lead to the loss of active sites and restrict the electrocatalytic performance.

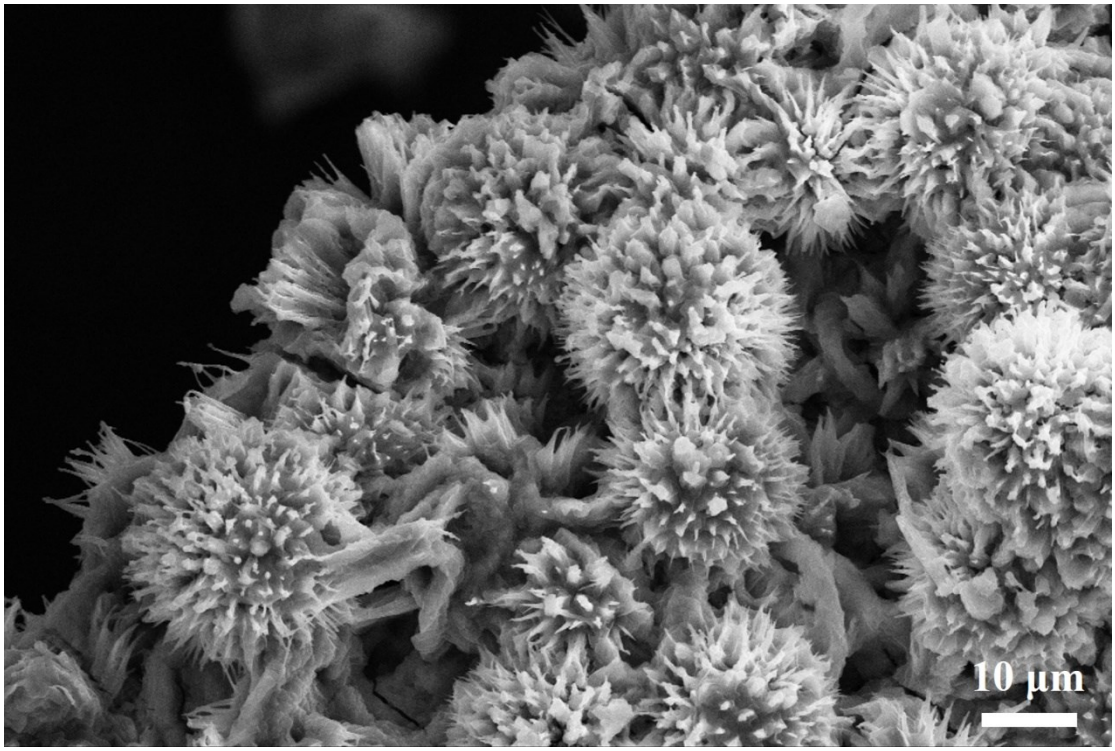

Figure 40. SEM image of Co_2P-Ni_3S_2/NF after electrocatalytic stability test.

To comprehensively evaluate the electrocatalytic stability of samples, we also need to implement all the material characterizations for our samples after the stability test, including SEM, TEM, XRD, and XPS. The changes in morphology, composition, and structure are important parameters to investigate the factors of durability. Combined with electrochemical tests, we can explain the overpotential increase and performance-damping trends.

3.6 Conclusion

In summary, Co_2P-Ni_3S_2 heterogeneous structural hollow nanowires supported on nickel foam were successfully synthesized by facile hydrothermal reactions and a low-temperature phosphating process. The as-synthesized Co_2P-Ni_3S_2/NF exhibits bifunctional electrocatalytic performance at large current density towards HER and OER in alkaline electrolyte, resulting from the large surface area of the unique hollow nanowire morphology, multiple active sites provided by transition metal compounds, and the synergistic effect of Co_2P/Ni_3S_2 heterostructure interfaces. The Co_2P-Ni_3S_2/NF demonstrates ultralow overpotentials of 110, 164 mV (HER) and 331.7, 358.3 mV (OER) at large current densities of 100, 500 mA cm^{-2} in 1.0 M KOH. Impressively, the two-electrode electrolytic cell assembled with Co_2P-Ni_3S_2/NF can provide a current density of 10 mA cm^{-2} at a cell voltage of 1.54 V in 1.0 M KOH, exhibiting competitive overall water splitting performance with reported non-noble metal-based electrocatalysts. Therefore, the present work provides an effective synthetic method to fabricate transition metal-based heterogeneous structures and brings new inspiration for designing highly efficient and stable HER/OER catalysts working at large current density and enhancing the development of novel electrocatalysts for overall water splitting.

Table 1. Summary of the HER performances of the reported electrocatalysts.

Catalysts	Electrolyte	Overpotential (mV) @ 10 mA cm^{-2}	Tafel Slope (mV dec^{-1})	Stability	Ref.
Co_2P-Ni_3S_2/NF (this work)	1.0 M KOH	41	114.2	48 h @ 100 mA cm^{-2}	–
CoP NFs	1.0 M KOH	136	56.2	30 h @ 10 mA cm^{-2}	[111]
CoP NFs	0.5 M H_2SO_4	122	54.8	30 h @ 10 mA cm^{-2}	[111]
Co_2P/CoP@Co@NCNT	1.0 M KOH	118	46	50 h @ 10 mA cm^{-2}	[110]
Co_2P/CoP@Co@NCNT	0.5 M H_2SO_4	136	49	12 h @ 10 mA cm^{-2}	[110]
O-CoP nanosheets	1.0 M KOH	98	59.9	15 h @ 10 mA cm^{-2}	[117]
Cr-CoP/CP	1.0 M KOH	67	31	30 h @ 10 mA cm^{-2}	[106]
Cr-CoP/CP	1.0 M PBS	131	67	–	[106]
Cr-CoP/CP	0.5 M H_2SO_4	47	46	30 h @ 10 mA cm^{-2}	[106]
CoP@FeCoP/NC YSMPs	1.0 M KOH	141	56.34	20 h @ 10 mA cm^{-2}	[115]

CoP/NF	1.0 M KOH	41.1	65.3	15 h @ 10 mA cm^{-2}	[114]
CoP/NF	1.0 M PBS	55.2	68.7	15 h @ 10 mA cm^{-2}	[114]
CoP/NF	0.5 M H_2SO_4	83.9	55	15 h @ 10 mA cm^{-2}	[114]
Ce_1-CoP	1.0 M KOH	144	70	1000 cycles	[107]
CoP@CoOOH/CP	1.0 M KOH	81.7	50.7	40 h @ 10 mA cm^{-2}	[116]
CoP@CoOOH/CP	1.0 M PBS	89.6	64.4	40 h @ 10 mA cm^{-2}	[116]
CoP/CNFs	1.0 M KOH	225	100.8	1000 cycles	[113]
F-CoP NAs/CF	1.0 M KOH	35	32	100 h @ 10 mA cm^{-2}	[41]
Er-doped CoP	1.0 M KOH	66	61	20 h @ 10 mA cm^{-2}	[105]
Er-doped CoP	0.5 M H_2SO_4	52	32	20 h @ 10 mA cm^{-2}	[105]
Mo-CoP	1.0 M KOH	118	76	10 h @ 10 mA cm^{-2}	[118]
Mo-CoP	0.5 M H_2SO_4	116	69	16 h @ 10 mA cm^{-2}	[118]

CoP-NCDs/NF	1.0 M KOH	103	92	24 h @ 20 mA cm^{-2}	[109]

Table 2. Summary of the OER performances of the reported electrocatalysts.

Catalysts	Electrolyte	Overpotential (mV) @ 10 mA cm^{-2}	Overpotential (mV) @ 50 mA cm^{-2}	Tafel Slope (mV dec^{-1})	Stability	Ref.
Co_2P-Ni_3S_2/NF (this work)	1.0 M KOH	270	311.7	31.6	48 h @ 100 mA cm^{-2}	–
CoP NFs	1.0 M KOH	323	–	49.6	30 h @ 10 mA cm^{-2}	[111]
Co_2P/CoP@ Co@NCNT	1.0 M KOH	256	–	46	50 h @ 10 mA cm^{-2}	[110]
FeNi-Co_2P	1.0 M KOH	225	–	42.8	18 h @ 10 mA cm^{-2}	[168]
O-CoP	1.0 M KOH	310	–	83.5	15 h @ 20 mA cm^{-2}	[117]
Cr-CoP/CP	1.0 M KOH	251	–	47	30 h @ 10 mA cm^{-2}	[106]
CoP@FeCoP /NC YSMPs	1.0 M KOH	238	–	47.98	20 h @ 20 mA cm^{-2}	[115]
CoP/NF	1.0 M KOH	–	317	65.6	12 h @ 10 mA cm^{-2}	[114]

Ce_1-CoP	1.0 M KOH	270	–	63	1000 cycles	[107]
CoP@CoOOH /CP	1.0 M KOH	200	–	131,8	40 h @ 10 mA cm^{-2}	[116]
CoP@CoOOH /CP	1.0 M PBS	318	–	127.4	40 h @ 10 mA cm^{-2}	[116]
CoP/CNFs	1.0 M KOH	325	–	29.4	1000 cycles	[113]
F-CoP NAs/CF	1.0 M KOH	–	231	73.2	100 h @ 50 mA cm^{-2}	[41]
Er-doped CoP	1.0 M KOH	256	–	70	20 h @ 10 mA cm^{-2}	[105]
Mo-CoP	1.0 M KOH	317	–	82	12 h @ 10 mA cm^{-2}	[118]
CoP-NCDs/NF	1.0 M KOH	226	–	86	24 h @ 20 mA cm^{-2}	[109]

Table 3. Summary of the reported large-current-density HER electrocatalysts.

Catalysts	Electrolyte	Overpotential (mV) @ 100 mA cm^{-2}	Overpotential (mV) @ 500 mA cm^{-2}	Overpotential (mV) @ 1000 mA cm^{-2}	Tafel Slope (mV dec^{-1})	Stability	Ref.
Co_2P-Ni_3S_2/NF (this work)	1.0 M KOH	110	164	196	114.2	48 h @ 100 mA cm^{-2}	–
NiCoSeP	1.0 M KOH	151	286	381	50	15 h @ 250 mA cm^{-2}	[169]
NiCoSeP	0.5 M H_2SO_4	93	131	–	–	15 h @ 250 mA cm^{-2}	[169]
Ni–W	1.0 M KOH	–	303	–	67	31 h @ 500 mA cm^{-2}	[170]
NiFe-LDH/ MXene/NF	1.0 M KOH	–	205	–	70	280 h @ 10 mA cm^{-2}	[171]
Fe_2P-Co_2P /CF	1.0 M KOH	145	208	254	56	300 h @ multi-current-density	[168]
Ni-Co-P/NF	1.0 M KOH	–	210	–	46	24 h @ 10 mA cm^{-2}	[172]
MnO_x/ NiFeP/NF	1.0 M KOH	214	255	–	41.8	100 h @ 100 mA cm^{-2}	[173]
F-Co_2P/ Fe_2P/IF	1.0 M KOH	151.8	229.8	260.5	115.01	10 h @ 500 mA cm^{-2}	[174]
$NiCoS_xSe_y$ /NCF	1.0 M KOH	149	256	345	34	100 h @ 100 mA cm^{-2}	[175]

$Fe_{13.7\%}$-Ni_3S_2	1.0 M KOH	197	246	266	49.5	14 h @ 500 mA cm^{-2}	[153]
NiCo@RuO_2 HNAs/NF	1.0 M KOH	63	148.5	236.1	69.3	300 h @ 500 mA cm^{-2}	[176]
$Ce_{0.2}$-CoP/Ni_3P @NF	1 M KOH	139	185	225	55	200 h @ 500 mA cm^{-2}	[108]

Table 4. Summary of the reported large-current-density OER electrocatalysts.

Catalysts	Electrolyte	Overpotential (mV) @ 100 mA cm^{-2}	Overpotential (mV) @ 500 mA cm^{-2}	Tafel Slope (mV dec^{-1})	Stability	Ref.
Co_2P-Ni_3S_2/NF (this work)	1.0 M KOH	332	358	31.6	48 h @ 100 mA cm^{-2}	–
NiFe-LDH/ MXene/NF	1.0 M KOH	–	300	44	60 h @ 100 mA cm^{-2} 280 h @ 10 mA cm^{-2}	[171]
Fe_2P-Co_2P/CF	1.0 M KOH	243	291	51	250 h @ multi-current-density	[168]
MnO_x/ NiFeP/NF	1.0 M KOH	247	296	59.8	150 h @ 100 mA cm^{-2}	[173]
$NiCoS_xSe_y$ /NCF	1.0 M KOH	314	–	42	100 h @ 100 mA cm^{-2}	[175]
$Fe_{13.7\%}$-Ni_3S_2	1.0 M KOH	–	245	55.7	14 h @ 500 mA cm^{-2}	[153]

Table 5. Summary of the reported water splitting performances.

Catalysts	Electrolyte	Cell Voltage at 10 mA cm^{-2}	Stability	Ref.
Co_2P-Ni_3S_2/NF (this work)	1 M KOH	1.54 V	24 h @ 100 mA cm^{-2}	–
CoP NFs	1 M KOH	1.65 V	30 h @ 10 mA cm^{-2}	[111]
CoP NCs	1 M KOH	1.75 V	–	[111]
Co_2P/CoP@Co@NCNT	1 M KOH	1.6 V	12 h @ 10 mA cm^{-2}	[110]
FeNi-Co_2P	1 M KOH	1.596 V	120 h @ 10 mA cm^{-2}	[112]
O-CoP nanosheets	1 M KOH	1.6 V	18 h @ 1.7 V	[117]
Cr-CoP/CP	1 M KOH	1.59 V	30 h @ 10 mA cm^{-2}	[106]
CoP@FeCoP/NC YSMPs	1 M KOH	1.68 V	20 h @ 10 mA cm^{-2}	[115]
CoP/NF	1 M KOH	1.54 V	28 h @ 10 mA cm^{-2}	[114]
Ce_1-CoP	1 M KOH	1.65 V	15 h @ 10 mA cm^{-2}	[107]

CoP@CoOOH/CP	1 M KOH	1.52 V	140 h @ 10 mA cm^{-2}	[116]
CoP@CoOOH/CP	1 M PBS	1.65 V	100 h @ 10 mA cm^{-2}	[116]
CoP/CNFs	1 M KOH	1.65 V	8 h @ 10 mA cm^{-2}	[113]
F-CoP NAs/CF	1 M KOH	1.48 V	100 h @ 1.48 V (10 mA cm^{-2})	[41]
Er-doped CoP	1 M KOH	1.58 V	25 h @ multi-current-density	[105]
Mo-CoP	1 M KOH	1.7 V	24 h @ 1.7 V (10 mA cm^{-2})	[118]
CoP-NCDs/NF	1 M KOH	1.55 V	24 h @ 10 mA cm^{-2}	[109]
NiFe-LDH/MXene/NF	1 M KOH	1.51 V	200 h @ 10 mA cm^{-2}	[171]
$Fe_{13.7\%}$-Ni_3S_2	1 M KOH	1.53 V	14 h @ 10 mA cm^{-2}	[153]
Fe_2P-Co_2P/CF	1 M KOH	1.51 V	300 h @ multi-current-density	[168]
$NiCoS_xSe_y$/NCF	1 M KOH	1.58 V	50 h @ 100 mA cm^{-2}	[175]

Chapter 4. Summary and prospect

To solve the existing problems and promote the development of multifunctional HER/OER/ORR electrocatalysts for commercialization, many strategies and solutions have been proposed and implemented. The current state-of-the-art commercial catalyst, Pt-based, and Ru/Ir-based electrocatalysts, still have some problems such as high cost, scarcity, poor impurity tolerance, and so on. Among numerous electrocatalysts, metal-based nanomaterials (including non-platinum Pd-based and nonprecious transition metal-based nanomaterials) have been widely studied in recent years. The unique physical, chemical, and electronic properties of these nanomaterials play an important role in multifunctional electrocatalysis by exposing more active sites, regulating the electronic structure, accelerating the mass transfer, reducing the Gibbs free energy barrier of reactant adsorption, *etc*. Thus, in the first three chapters of this thesis, a literature review for both Pd-based and transition metal-based nanomaterials, and an experiment for catalyst fabrication are carried out to investigate and design novel multifunctional electrocatalysts.

Inspired by the rapid development of numerous novel strategies in the electrocatalytic research field, the mechanism of electrocatalytic OER/HER reactions is clearly demonstrated, and metal-based electrocatalysts including Pd-based and transition metal-based nanomaterials are summarized in Chapter 1.

Based on the literature review in Chapter 1, the objectives and experimental design are clarified in Chapter 2.

In Chapter 3, a novel and facile synthetic strategy is proposed to construct a heterogeneous structure composite. The Co_2P/Ni_3S_2 heterojunction is fabricated by the growth of nickel sulfides, cobalt-containing intermediates, and further phosphating process. The as-prepared Co_2P-Ni_3S_2/NF exhibits remarkable HER/OER performance, demonstrating ultralow overpotentials of 110, 164 mV for HER and 331.7, 358.3 mV for OER at large current densities of 100, 500 mA cm^{-2} in 1.0 M KOH. The two-

electrode electrolytic cell assembled by Co_2P-Ni_3S_2/NF can provide a current density of 10 mA cm^{-2} at a cell voltage of 1.54 V in 1.0 M KOH, exhibiting competitive overall water splitting performance with other reported transition metal-based catalysts. This work brings new inspiration for engineering highly efficient and stable water splitting catalysts working at large current densities.

Challenges of multifunctional electrocatalysis still exist. a) The electrocatalytic mechanism is not entirely clear, especially for the four-electron transfer pathways of ORR and OER. b) Surface deformation and particle aggregation impose restrictions on the stability of nanomaterials. c) Development of cost-effective and scalable synthetic routes is still one of the problems for large-scale production. Aiming at these existing challenges and problems, more effective strategies will be proposed, and the approaches to design and fabricate highly efficient, robust, and easily scalable electrocatalysts will be developed.

Reference

[1] F.D. Sanij, P. Balakrishnan, P. Leung, A. Shah, H. Su, Q. Xu, Advanced Pd-based nanomaterials for electro-catalytic oxygen reduction in fuel cells: A review, Int. J. Hydrog. Energy 46 (2021) 14596-14627.

[2] K. Zhang, R. Zou, Advanced transition metal-based OER electrocatalysts: current status, opportunities, and challenges, Small 17 (2021) 2100129.

[3] Z.F. Huang, J. Wang, Y. Peng, C.Y. Jung, A. Fisher, X. Wang, Design of efficient bifunctional oxygen reduction/evolution electrocatalyst: recent advances and perspectives, Adv. Energy Mater. 7 (2017) 1700544.

[4] R. Devivaraprasad, N. Nalajala, B. Bera, M. Neergat, Electrocatalysis of oxygen reduction reaction on shape-controlled Pt and Pd nanoparticles—importance of surface cleanliness and reconstruction, Front. Chem. 7 (2019) 648.

[5] T. Wang, A. Chutia, D.J. Brett, P.R. Shearing, G. He, G. Chai, I.P. Parkin, Palladium alloys used as electrocatalysts for the oxygen reduction reaction, Energy Environ. Sci. 14 (2021) 2639-2669.

[6] Z. Zhao, C. Chen, Z. Liu, J. Huang, M. Wu, H. Liu, Y. Li, Y. Huang, Pt-based nanocrystal for electrocatalytic oxygen reduction, Adv. Mater. 31 (2019) 1808115.

[7] D. Bhalothia, L. Krishnia, S.-S. Yang, C. Yan, W.-H. Hsiung, K.-W. Wang, T.-Y. Chen, Recent advancements and future prospects of noble metal-based heterogeneous nanocatalysts for oxygen reduction and hydrogen evolution reactions, Appl. Sci. 10 (2020) 7708.

[8] H. Zhong, C.A. Campos-Roldán, Y. Zhao, S. Zhang, Y. Feng, N. Alonso-Vante, Recent advances of cobalt-based electrocatalysts for oxygen electrode reactions and hydrogen evolution reaction, Catalysts 8 (2018) 559.

[9] H.C. Li, Y.J. Zhang, X. Hu, W.J. Liu, J.J. Chen, H.Q. Yu, Metal–organic framework templated Pd@ PdO–Co3O4 nanocubes as an efficient bifunctional oxygen electrocatalyst, Adv. Energy Mater. 8 (2018) 1702734.

[10] B.Y. Xia, Y. Yan, N. Li, H.B. Wu, X.W.D. Lou, X. Wang, A metal–organic framework-derived

bifunctional oxygen electrocatalyst, Nat. Energy 1 (2016) 1-8.

[11] X.F. Lu, B.Y. Xia, S.Q. Zang, X.W. Lou, Metal–organic frameworks based electrocatalysts for the oxygen reduction reaction, Angew. Chem. 132 (2020) 4662-4678.

[12] J. Song, C. Wei, Z.-F. Huang, C. Liu, L. Zeng, X. Wang, Z.J. Xu, A review on fundamentals for designing oxygen evolution electrocatalysts, Chem. Soc. Rev. 49 (2020) 2196-2214.

[13] Q. Liang, G. Brocks, A. Bieberle-Hütter, Oxygen evolution reaction (OER) mechanism under alkaline and acidic conditions, Journal of Physics: Energy 3 (2021) 026001.

[14] K. Chen, S. Kim, R. Rajendiran, K. Prabakar, G. Li, Z. Shi, C. Jeong, J. Kang, O.L. Li, Enhancing ORR/OER active sites through lattice distortion of Fe-enriched FeNi3 intermetallic nanoparticles doped N-doped carbon for high-performance rechargeable Zn-air battery, J. Colloid Interface Sci. 582 (2021) 977-990.

[15] Y. Zhao, J. You, L. Wang, W. Bao, R. Yao, Recent advances in Ni3S2-based electrocatalysts for oxygen evolution reaction, Int. J. Hydrog. Energy 46 (2021) 39146-39182.

[16] G. Zhao, K. Rui, S.X. Dou, W. Sun, Heterostructures for electrochemical hydrogen evolution reaction: a review, Adv. Funct. Mater. 28 (2018) 1803291.

[17] A. Lasia, Mechanism and kinetics of the hydrogen evolution reaction, Int. J. Hydrog. Energy 44 (2019) 19484-19518.

[18] B. Tilak, C.-P. Chen, Generalized analytical expressions for Tafel slope, reaction order and ac impedance for the hydrogen evolution reaction (HER): mechanism of HER on platinum in alkaline media, J. Appl. Electrochem. 23 (1993) 631-640.

[19] H. Ooka, J. Huang, K.S. Exner, The sabatier principle in electrocatalysis: Basics, limitations, and extensions, Front. Energy Res. 9 (2021) 654460.

[20] A.B. Laursen, A.S. Varela, F. Dionigi, H. Fanchiu, C. Miller, O.L. Trinhammer, J. Rossmeisl, S. Dahl, Electrochemical hydrogen evolution: Sabatier's principle and the volcano plot, J. Chem. Educ. 89 (2012) 1595-1599.

[21] M. Zhou, J. Guo, J. Fang, Nanoscale Design of Pd-Based Electrocatalysts for Oxygen Reduction Reaction Enhancement in Alkaline Media, Small Structures 3 (2022) 2100188.

[22] Q. Chen, Z. Chen, A. Ali, Y. Luo, H. Feng, Y. Luo, P. Tsiakaras, P.K. Shen, Shell-thickness-dependent Pd@ PtNi core–shell nanosheets for efficient oxygen reduction reaction, Chem. Eng. J.

427 (2022) 131565.

[23] M. Torihata, M. Nakamura, N. Todoroki, T. Wadayama, N. Hoshi, Activity for the ORR on Pt-Pd-Co ternary alloy electrodes is markedly affected by surface structure and composition, Electrochem. Commun. 125 (2021) 107007.

[24] D. Bhalothia, J.-P. Chou, C. Yan, A. Hu, Y.-T. Yang, T.-Y. Chen, Programming ORR Activity of Ni/NiO x@ Pd Electrocatalysts via Controlling Depth of Surface-Decorated Atomic Pt Clusters, ACS omega 3 (2018) 8733-8744.

[25] Y. Wang, L. Zhang, C. Hu, S. Yu, P. Yang, D. Cheng, Z.-J. Zhao, J. Gong, Fabrication of bilayer Pd-Pt nanocages with sub-nanometer thin shells for enhanced hydrogen evolution reaction, Nano Res. 12 (2019) 2268-2274.

[26] A.A. Ensafi, N. Zandi-Atashbar, Z. Mohamadi, A. Abdolmaleki, B. Rezaei, Pt-Pd nanoparticles decorated sulfonated graphene-poly(3,4-ethylene dioxythiophene) nanocomposite, An efficient HER electrocatalyst, Energy 126 (2017) 88-96.

[27] X. Yang, J. Hu, R. Wu, B.E. Koel, Balancing Activity and Stability in a Ternary Au-Pd/Fe Electrocatalyst for ORR with High Surface Coverages of Au, ChemCatChem 11 (2019) 693-697.

[28] T. Wu, M. Sun, B. Huang, Highly active electron-affinity for ultra-low barrier for alkaline ORR in Pd3Cu, Mater. Today Energy 12 (2019) 426-430.

[29] G. Bampos, L. Sygellou, S. Bebelis, Oxygen reduction reaction activity of Pd-based bimetallic electrocatalysts in alkaline medium, Catal. Today 355 (2020) 685-697.

[30] R. Sun, W. Guo, X. Han, X. Hong, Two-dimensional noble metal nanomaterials for electrocatalysis, Chem Res Chin Univ 36 (2020) 597-610.

[31] H. Zhang, A.W. Maijenburg, X. Li, S.L. Schweizer, R.B. Wehrspohn, Bifunctional heterostructured transition metal phosphides for efficient electrochemical water splitting, Adv. Funct. Mater. 30 (2020) 2003261.

[32] Y.-N. Zhou, Y.-R. Zhu, X.-Y. Chen, B. Dong, Q.-Z. Li, Y.-M. Chai, Carbon–based transition metal sulfides/selenides nanostructures for electrocatalytic water splitting, J. Alloys Compd. 852 (2021) 156810.

[33] X.-P. Li, C. Huang, W.-K. Han, T. Ouyang, Z.-Q. Liu, Transition metal-based electrocatalysts for overall water splitting, Chin. Chem. Lett. 32 (2021) 2597-2616.

[34] Y. Li, Z. Yin, M. Cui, X. Liu, J. Xiong, S. Chen, T. Ma, Interface engineering of transitional metal sulfide–MoS 2 heterostructure composites as effective electrocatalysts for water-splitting, J. Mater. Chem. A 9 (2021) 2070-2092.

[35] L.-M. Cao, J. Zhang, L.-W. Ding, Z.-Y. Du, C.-T. He, Metal-organic frameworks derived transition metal phosphides for electrocatalytic water splitting, J. Energy Chem. 68 (2022) 494-520.

[36] N. Zhang, I. Amorim, L. Liu, Multimetallic transition metal phosphide nanostructures for supercapacitors and electrochemical water splitting, Nanotechnology (2022).

[37] P. Chen, J. Ye, H. Wang, L. Ouyang, M. Zhu, Recent progress of transition metal carbides/nitrides for electrocatalytic water splitting, J. Alloys Compd. 883 (2021) 160833.

[38] X. Peng, C. Pi, X. Zhang, S. Li, K. Huo, P.K. Chu, Recent progress of transition metal nitrides for efficient electrocatalytic water splitting, Sustainable Energy & Fuels 3 (2019) 366-381.

[39] J. Su, J. Zhou, L. Wang, C. Liu, Y. Chen, Synthesis and application of transition metal phosphides as electrocatalyst for water splitting, Science bulletin 62 (2017) 633-644.

[40] A.H. Al-Naggar, N.M. Shinde, J.-S. Kim, R.S. Mane, Water splitting performance of metal and non-metal-doped transition metal oxide electrocatalysts, Coord. Chem. Rev. 474 (2023) 214864.

[41] Y. Sun, W. Sun, L. Chen, A. Meng, G. Li, L. Wang, J. Huang, A. Song, Z. Zhang, Z. Li, Surface reconstruction, doping and vacancy engineering to improve the overall water splitting of CoP nanoarrays, Nano Res. 16 (2023) 228-238.

[42] Y. Lin, L. Yang, Y. Zhang, H. Jiang, Z. Xiao, C. Wu, G. Zhang, J. Jiang, L. Song, Defective carbon–CoP nanoparticles hybrids with interfacial charges polarization for efficient bifunctional oxygen electrocatalysis, Adv. Energy Mater. 8 (2018) 1703623.

[43] J. Bao, Y. Zhou, Y. Zhang, X. Sheng, Y. Wang, S. Liang, C. Guo, W. Yang, T. Zhuang, Y. Hu, Engineering water splitting sites in three-dimensional flower-like Co–Ni–P/MoS 2 heterostructural hybrid spheres for accelerating electrocatalytic oxygen and hydrogen evolution, J. Mater. Chem. A 8 (2020) 22181-22190.

[44] C. Kim, F. Dionigi, V. Beermann, X. Wang, T. Möller, P. Strasser, Alloy nanocatalysts for the electrochemical oxygen reduction (ORR) and the direct electrochemical carbon dioxide reduction reaction (CO2RR), Adv. Mater. 31 (2019) 1805617.

[45] M. Sankar, N. Dimitratos, P.J. Miedziak, P.P. Wells, C.J. Kiely, G.J. Hutchings, Designing

bimetallic catalysts for a green and sustainable future, Chem. Soc. Rev. 41 (2012) 8099-8139.

[46] M. Luo, Z. Zhao, Y. Zhang, Y. Sun, Y. Xing, F. Lv, Y. Yang, X. Zhang, S. Hwang, Y. Qin, PdMo bimetallene for oxygen reduction catalysis, Nature 574 (2019) 81-85.

[47]D. Wu, X. Shen, Y. Pan, L. Yao, Z. Peng, Platinum alloy catalysts for oxygen reduction reaction: Advances, challenges and perspectives, ChemNanoMat 6 (2020) 32-41.

[48] M. Neergat, V. Gunasekar, R. Rahul, Carbon-supported Pd–Fe electrocatalysts for oxygen reduction reaction (ORR) and their methanol tolerance, J. Electroanal. Chem. 658 (2011) 25-32.

[49] L.E. Betancourt, A. Rojas-Perez, I. Orozco, A.I. Frenkel, Y. Li, K. Sasaki, S.D. Senanayake, C.R. Cabrera, Enhancing ORR performance of bimetallic PdAg electrocatalysts by designing interactions between Pd and Ag, ACS Appl. Energy Mater. 3 (2020) 2342-2349.

[50] J. Kim, Y. Hong, K. Lee, J.Y. Kim, Highly stable Pt-based ternary systems for oxygen reduction reaction in acidic electrolytes, Adv. Energy Mater. 10 (2020) 2002049.

[51] X. Jiang, Y. Xiong, R. Zhao, J. Zhou, J.-M. Lee, Y. Tang, Trimetallic Au@ PdPb nanowires for oxygen reduction reaction, Nano Res. 13 (2020) 2691-2696.

[52] Z.-P. Wu, D.T. Caracciolo, Y. Maswadeh, J. Wen, Z. Kong, S. Shan, J.A. Vargas, S. Yan, E. Hopkins, K. Park, Alloying–realloying enabled high durability for Pt–Pd-3d-transition metal nanoparticle fuel cell catalysts, Nat. Commun. 12 (2021) 859.

[53] X. Wei, S. Song, W. Cai, X. Luo, L. Jiao, Q. Fang, X. Wang, N. Wu, Z. Luo, H. Wang, Tuning the spin-state of Fe single atoms by Pd nanoclusters enables robust oxygen reduction with dissociative pathway, Chem (2022).

[54] H. Cruz-Martínez, M. Tellez-Cruz, O. Solorza-Feria, P. Calaminici, D. Medina, Catalytic activity trends from pure Pd nanoclusters to M@ PdPt (M= Co, Ni, and Cu) core-shell nanoclusters for the oxygen reduction reaction: A first-principles analysis, Int. J. Hydrog. Energy 45 (2020) 13738-13745.

[55] N. Wang, X. Zhao, R. Zhang, S. Yu, Z.H. Levell, C. Wang, S. Ma, P. Zou, L. Han, J. Qin, Highly Selective Oxygen Reduction to Hydrogen Peroxide on a Carbon-Supported Single-Atom Pd Electrocatalyst, ACS Catal. 12 (2022) 4156-4164.

[56] H.E. Kim, I.H. Lee, J. Cho, S. Shin, H.C. Ham, J.Y. Kim, H. Lee, Palladium Single-Atom Catalysts Supported on C@ C3N4 for Electrochemical Reactions, ChemElectroChem 6 (2019)

4757-4764.

[57] K. Jiang, S. Back, A.J. Akey, C. Xia, Y. Hu, W. Liang, D. Schaak, E. Stavitski, J.K. Nørskov, S. Siahrostami, Highly selective oxygen reduction to hydrogen peroxide on transition metal single atom coordination, Nat. Commun. 10 (2019) 1-11.

[58] Z. Wei, B. Deng, P. Chen, T. Zhao, S. Zhao, Palladium-based single atom catalysts for high-performance electrochemical production of hydrogen peroxide, Chem. Eng. J. 428 (2022) 131112.

[59] Z. Fu, C. Ling, J. Wang, A Ti 3 C 2 O 2 supported single atom, trifunctional catalyst for electrochemical reactions, J. Mater. Chem. A 8 (2020) 7801-7807.

[60] Z. Qin, J. Zhao, 1 T-MoSe2 monolayer supported single Pd atom as a highly-efficient bifunctional catalyst for ORR/OER, J. Colloid Interface Sci. 605 (2022) 155-162.

[61] M.T. Darby, M. Stamatakis, Single-Atom Alloys for the Electrochemical Oxygen Reduction Reaction, ChemPhysChem 22 (2021) 499-508.

[62] R. Li, D. Wang, Superiority of dual-atom catalysts in electrocatalysis: one step further than single-atom catalysts, Adv. Energy Mater. 12 (2022) 2103564.

[63] M. Huang, H. Meng, J. Luo, H. Li, Y. Feng, X.-X. Xue, Understanding the Activity and Design Principle of Dual-Atom Catalysts Supported on C2N for Oxygen Reduction and Evolution Reactions: From Homonuclear to Heteronuclear, J. Phys. Chem. Lett. 14 (2023) 1674-1683.

[64] X. Wang, L. Guo, Z. Xie, X. Peng, X. Yu, X. Yang, Z. Lu, X. Zhang, L. Li, Coordination environment engineering of graphene-supported single/dual-Pd-site catalysts improves the electrocatalytic ORR activity, Appl. Surf. Sci. 606 (2022) 154749.

[65] Z. Chen, F. Lin, D. He, H. Jiang, J. Zhang, X. Wang, M. Huang, A hybrid composite catalyst of Fe 3 O 4 nanoparticles-based carbon for electrochemical reduction of oxygen, New J. Chem. 41 (2017) 4959-4965.

[66] H. Park, S. Oh, S. Lee, S. Choi, M. Oh, Cobalt-and nitrogen-codoped porous carbon catalyst made from core–shell type hybrid metal–organic framework (ZIF-L@ ZIF-67) and its efficient oxygen reduction reaction (ORR) activity, Appl. Catal. B Environ. 246 (2019) 322-329.

[67] H. Wang, W. Wang, H. Yu, Q. Mao, Y. Xu, X. Li, Z. Wang, L. Wang, Interface engineering of polyaniline-functionalized porous Pd metallene for alkaline oxygen reduction reaction, Appl. Catal. B Environ. 307 (2022) 121172.

[68] M.S. Matseke, T.S. Munonde, K. Mallick, H. Zheng, Pd/PANI/C nanocomposites as electrocatalysts for oxygen reduction reaction in alkaline media, Electrocatalysis 10 (2019) 436-444.

[69] G. Wu, Z. Chen, K. Artyushkova, F.H. Garzon, P. Zelenay, Polyaniline-derived non-precious catalyst for the polymer electrolyte fuel cell cathode, ECS Trans 16 (2008) 159.

[70] A. Ejaz, S. Jeon, The individual role of pyrrolic, pyridinic and graphitic nitrogen in the growth kinetics of Pd NPs on N-rGO followed by a comprehensive study on ORR, Int. J. Hydrog. Energy 43 (2018) 5690-5702.

[71] X. Dong, J. Li, D. Wei, R. Li, K. Qu, L. Wang, S. Xu, W. Kang, H. Li, Pd (II)/Ni (II)-dimethylglyoxime derived Pd–Ni–P@ N-doped carbon hybrid nanocatalysts for oxygen reduction reaction, Appl. Surf. Sci. 479 (2019) 273-279.

[72] Y. Wu, Z. Xiao, Z. Jin, X. Li, Y. Chen, The cobalt carbide/bimetallic CoFe phosphide dispersed on carbon nanospheres as advanced bifunctional electrocatalysts for the ORR, OER, and rechargeable Zn–air batteries, J. Colloid Interface Sci. 590 (2021) 321-329.

[73] Z.K. Ghouri, K. Elsaid, M.M. Nasef, S. Ahmed, A. Badreldin, A. Abdel-Wahab, Cooperative electrocatalytic effect of Pd and Ce alloys nanoparticles in PdCe@ CNWs electrode for oxygen evolution reaction (OER), Mol. Catal. 522 (2022) 112255.

[74] T. Zhang, S.-A. Liao, L.-X. Dai, J.-W. Yu, W. Zhu, Y.-W. Zhang, Ir-Pd nanoalloys with enhanced surface-microstructure-sensitive catalytic activity for oxygen evolution reaction in acidic and alkaline media, SCMs 61 (2018) 926-938.

[75] G.M. Salvador, A.L. Silva, L.P. Silva, F.B. Passos, N.M. Carvalho, Enhanced activity of Pd/α-MnO2 for electrocatalytic oxygen evolution reaction, Int. J. Hydrog. Energy 46 (2021) 26976-26988.

[76] A. Saad, D. Liu, Y. Wu, Z. Song, Y. Li, T. Najam, K. Zong, P. Tsiakaras, X. Cai, Ag nanoparticles modified crumpled borophene supported Co3O4 catalyst showing superior oxygen evolution reaction (OER) performance, Appl. Catal. B Environ. 298 (2021) 120529.

[77] Y. Wang, J. Ma, J. Wang, S. Chen, H. Wang, J. Zhang, Interfacial Scaffolding Preparation of Hierarchical PBA-Based Derivative Electrocatalysts for Efficient Water Splitting, Adv. Energy Mater. 9 (2019) 1802939.

[78] J. Kang, J. Chen, J. Sheng, J. Xie, X.-Z. Fu, R. Sun, C.-P. Wong, Pd nanoparticle-interspersed hierarchical copper hydroxide@ nickel cobalt hydroxide carbonate tubular arrays as efficient

electrocatalysts for oxygen evolution reaction, ACS Sustain. Chem. Eng. 7 (2019) 16459-16466.

[79] Y. Li, H. Dai, Recent advances in zinc–air batteries, Chem. Soc. Rev. 43 (2014) 5257-5275.

[80] D. Chen, J. Zhu, X. Mu, R. Cheng, W. Li, S. Liu, Z. Pu, C. Lin, S. Mu, Nitrogen-Doped carbon coupled FeNi3 intermetallic compound as advanced bifunctional electrocatalyst for OER, ORR and zn-air batteries, Appl. Catal. B Environ. 268 (2020) 118729.

[81] S. Ramakrishnan, J. Balamurugan, M. Vinothkannan, A.R. Kim, S. Sengodan, D.J. Yoo, Nitrogen-doped graphene encapsulated FeCoMoS nanoparticles as advanced trifunctional catalyst for water splitting devices and zinc–air batteries, Appl. Catal. B Environ. 279 (2020) 119381.

[82] H. Over, Fundamental studies of planar single-crystalline oxide model electrodes (RuO2, IrO2) for acidic water splitting, ACS Catal. 11 (2021) 8848-8871.

[83] J.-X. Guo, S.-Y. Wu, G.-J. Zhang, L. Yan, J.-G. Hu, X.-Y. Li, Single noble metals (Pd, Pt and Ir) anchored Janus MoSSe monolayers: Efficient oxygen reduction/evolution reaction bifunctional electrocatalysts and harmful gas detectors, J. Colloid Interface Sci. 616 (2022) 177-188.

[84] X. Liu, Q. Huang, J. Wang, L. Zhao, H. Xu, Q. Xia, D. Li, L. Qian, H. Wang, J. Zhang, In-situ deposition of Pd/Pd4S heterostructure on hollow carbon spheres as efficient electrocatalysts for rechargeable Li-O2 batteries, Chin. Chem. Lett. 32 (2021) 2086-2090.

[85] M.Y. Oh, J.H. Kim, Y.W. Lee, K.J. Kim, H.R. Shin, H. Park, K.T. Lee, K. Kang, T.H. Shin, Enhancing Bifunctional Catalytic Activity via a Nanostructured La (Sr) Fe (Co) O3− δ@ Pd Matrix as an Efficient Electrocatalyst for Li–O2 Batteries, ACS Appl. Energy Mater. 2 (2019) 8633-8640.

[86] Y. Liu, S. Jiang, S. Li, L. Zhou, Z. Li, J. Li, M. Shao, Interface engineering of (Ni, Fe) S2@ MoS2 heterostructures for synergetic electrochemical water splitting, Appl. Catal. B Environ. 247 (2019) 107-114.

[87] M. You, X. Du, X. Hou, Z. Wang, Y. Zhou, H. Ji, L. Zhang, Z. Zhang, S. Yi, D. Chen, In-situ growth of ruthenium-based nanostructure on carbon cloth for superior electrocatalytic activity towards HER and OER, Appl. Catal. B Environ. 317 (2022) 121729.

[88] Y. Wang, L. Zhao, J. Ma, J. Zhang, Confined interface transformation of metal–organic frameworks for highly efficient oxygen evolution reactions, Energy Environ. Sci. 15 (2022) 3830-3841.

[89] A.K. Ipadeola, P.V. Mwonga, S.C. Ray, R.R. Maphanga, K.I. Ozoemena, Bifunctional

Behavior of Pd/Ni Nanocatalysts on MOF-Derived Carbons for Alkaline Water-splitting, Electroanalysis 32 (2020) 3060-3074.

[90] P. Mondal, J. Satra, D.N. Srivastava, G.R. Bhadu, B. Adhikary, Pdδ+-Mediated Surface Engineering of AgMnO4 Nanorods as Advanced Bifunctional Electrocatalysts for Highly Efficient Water Electrolysis, ACS Catal. 11 (2021) 3687-3703.

[91] X. Zhang, P. Yang, Pd nanoparticles assembled on Ni-and N-doped carbon nanotubes towards superior electrochemical activity, Int. J. Hydrog. Energy 46 (2021) 2065-2074.

[92] Y.-Y. Liu, H.-P. Zhang, B. Zhu, H.-W. Zhang, L.-D. Fan, X.-Y. Chai, Q.-L. Zhang, J.-H. Liu, C.-X. He, C/N-co-doped Pd coated Ag nanowires as a high-performance electrocatalyst for hydrogen evolution reaction, Electrochim. Acta 283 (2018) 221-227.

[93] J. Li, Y. Cheng, J. Zhang, J. Fu, W. Yan, Q. Xu, Confining Pd Nanoparticles and Atomically Dispersed Pd into Defective MoO3 Nanosheet for Enhancing Electro- and Photocatalytic Hydrogen Evolution Performances, ACS Appl Mater Interfaces 11 (2019) 27798-27804.

[94] D. Ohm, K.F. Domke, Controlled deposition of 2D-confined Pd or Ir nano-islands on Au(1 1 1) following Cu UPD, and their HER activity, J. Electroanal. Chem. 896 (2021).

[95] B.T. Jebaslinhepzybai, N. Prabu, M. Sasidharan, Facile galvanic replacement method for porous Pd@Pt nanoparticles as an efficient HER electrocatalyst, Int. J. Hydrog. Energy 45 (2020) 11127-11137.

[96] J. Li, F. Li, S.X. Guo, J. Zhang, J. Ma, PdCu@Pd Nanocube with Pt-like Activity for Hydrogen Evolution Reaction, ACS Appl Mater Interfaces 9 (2017) 8151-8160.

[97] X. Liu, S. Zhu, Y. Liang, H. Jiang, Z. Li, S. Wu, Z. Cui, Self-standing nanoporous NiPd bimetallic electrocatalysts with ultra-low Pd loading for efficient hydrogen evolution reaction, Electrochim. Acta 411 (2022).

[98] U. Lačnjevac, R. Vasilić, T. Tokarski, G. Cios, P. Żabiński, N. Elezović, N. Krstajić, Deposition of Pd nanoparticles on the walls of cathodically hydrogenated TiO2 nanotube arrays via galvanic displacement: A novel route to produce exceptionally active and durable composite electrocatalysts for cost-effective hydrogen evolution, Nano energy 47 (2018) 527-538.

[99] V. Burungale, H. Bae, P. Mane, H. Rho, S.-W. Ryu, S.H. Kang, J.-S. Ha, Improved performance of CNT-Pd modified Cu2O supported on Nickel foam for hydrogen evolution reaction in basic

media, J. Mol. Liq. 343 (2021).

[100] M. Nie, Z.H. Xue, H. Sun, J.M. Liao, F.J. Xue, X.X. Wang, Pd doped Ni derived from Ni - Metal organic framework for efficient hydrogen evolution reaction in alkaline electrolyte, Int. J. Hydrog. Energy 45 (2020) 28870-28875.

[101] M. Nie, H. Sun, D. Lei, S. Kang, J. Liao, P. Guo, Z. Xue, F. Xue, Novel Pd/MOF electrocatalyst for hydrogen evolution reaction, Mater. Chem. Phys. 254 (2020).

[102] J.-Y. Yue, X.-L. Ding, L.-P. Song, Y.-T. Wang, P. Yang, Y. Ma, B. Tang, Pd(II) functionalized vinylene-linked covalent organic frameworks for acidic electrocatalytic hydrogen evolution reaction, Microporous Mesoporous Mater. 344 (2022).

[103] C. Shu, H. Du, W. Pu, C. Yang, J. Gong, Trace amounts of palladium-doped hollow TiO2 nanosphere as highly efficient electrocatalyst for hydrogen evolution reaction, Int. J. Hydrog. Energy 46 (2021) 1923-1933.

[104] M. Smiljanić, I. Srejić, J. Potočnik, M. Mitrić, Z. Rakočević, S. Štrbac, Synergistic electrocatalytic effect of Pd and Rh nanoislands co-deposited on Au(poly) on HER in alkaline solution, Int. J. Hydrog. Energy 43 (2018) 19420-19431.

[105] G. Zhang, B. Wang, J. Bi, D. Fang, S. Yang, Constructing ultrathin CoP nanomeshes by Er-doping for highly efficient bifunctional electrocatalysts for overall water splitting, J. Mater. Chem. A 7 (2019) 5769-5778.

[106] W. Li, Y. Jiang, Y. Li, Q. Gao, W. Shen, Y. Jiang, R. He, M. Li, Electronic modulation of CoP nanoarrays by Cr-doping for efficient overall water splitting, Chem. Eng. J. 425 (2021) 130651.

[107] J. Li, S. Zou, X. Liu, Y. Lu, D. Dong, Electronically modulated CoP by Ce doping as a highly efficient electrocatalyst for water splitting, ACS Sustain. Chem. Eng. 8 (2020) 10009-10016.

[108] F. Zhang, X. Wang, W. Han, Y. Qian, L. Qiu, Y. He, L. Lei, X. Zhang, The synergistic activation of Ce-doping and CoP/Ni3P hybrid interaction for efficient water splitting at large-current-density, Adv. Funct. Mater. 33 (2023) 2212381.

[109] H. Liu, Z. Liu, Y. Wang, J. Zhang, Z. Yang, H. Hu, Q. Zhao, H. Ning, L. Zhi, M. Wu, Carbon dots-oriented synthesis of fungus-like CoP microspheres as a bifunctional electrocatalyst for efficient overall water splitting, Carbon 182 (2021) 327-334.

[110] Z. Lu, Y. Cao, J. Xie, J. Hu, K. Wang, D. Jia, Construction of Co2P/CoP@ Co@ NCNT

rich-interface to synergistically promote overall water splitting, Chem. Eng. J. 430 (2022) 132877.

[111] L. Ji, J. Wang, X. Teng, T.J. Meyer, Z. Chen, CoP nanoframes as bifunctional electrocatalysts for efficient overall water splitting, ACS Catal. 10 (2019) 412-419.

[112] J. Li, D. Chu, D.R. Baker, A. Leff, P. Zheng, R. Jiang, Earth-abundant Fe and Ni dually doped Co2P for superior oxygen evolution reactivity and as a bifunctional electrocatalyst toward renewable energy-powered overall alkaline water splitting, ACS Appl. Energy Mater. 4 (2021) 9969-9981.

[113] X.-Q. Xie, J. Liu, C. Gu, J. Li, Y. Zhao, C.-S. Liu, Hierarchical structured CoP nanosheets/carbon nanofibers bifunctional eletrocatalyst for high-efficient overall water splitting, J. Energy Chem. 64 (2022) 503-510.

[114] J. Liu, Y. Gao, X. Tang, K. Zhan, B. Zhao, B.Y. Xia, Y. Yan, Metal–organic framework-derived hierarchical ultrathin CoP nanosheets for overall water splitting, J. Mater. Chem. A 8 (2020) 19254-19261.

[115] J. Shi, F. Qiu, W. Yuan, M. Guo, Z.-H. Lu, Nitrogen-doped carbon-decorated yolk-shell CoP@ FeCoP micro-polyhedra derived from MOF for efficient overall water splitting, Chem. Eng. J. 403 (2021) 126312.

[116] B. Zhang, J. Shan, W. Wang, P. Tsiakaras, Y. Li, Oxygen Vacancy and Core–Shell Heterojunction Engineering of Anemone-Like CoP@ CoOOH Bifunctional Electrocatalyst for Efficient Overall Water Splitting, Small 18 (2022) 2106012.

[117] G. Zhou, M. Li, Y. Li, H. Dong, D. Sun, X. Liu, L. Xu, Z. Tian, Y. Tang, Regulating the electronic structure of CoP nanosheets by O incorporation for high-efficiency electrochemical overall water splitting, Adv. Funct. Mater. 30 (2020) 1905252.

[118] L. Li, Y. Guo, X. Wang, X. Liu, Y. Lu, Ultraeven Mo-doped CoP nanocrystals as bifunctional electrocatalyst for efficient overall water splitting, Langmuir 37 (2021) 5986-5992.

[119] W. Gong, H. Zhang, L. Yang, Y. Yang, J. Wang, H. Liang, Core@ shell MOFs derived Co2P/CoP@ NPGC as a highly-active bifunctional electrocatalyst for ORR/OER, Journal of Industrial and Engineering Chemistry 106 (2022) 492-502.

[120] D. Zhang, H. Mou, F. Lu, C. Song, D. Wang, A novel strategy for 2D/2D NiS/graphene heterostructures as efficient bifunctional electrocatalysts for overall water splitting, Appl. Catal. B

Environ. 254 (2019) 471-478.

[121] K. Srinivas, Y. Chen, X. Wang, B. Wang, M. Karpuraranjith, W. Wang, Z. Su, W. Zhang, D. Yang, Constructing Ni/NiS heteronanoparticle-embedded metal–organic framework-derived nanosheets for enhanced water-splitting catalysis, ACS Sustain. Chem. Eng. 9 (2021) 1920-1931.

[122] X. Xu, H. Xu, D. Cheng, Design of high-performance MoS 2 edge supported single-metal atom bifunctional catalysts for overall water splitting via a simple equation, Nanoscale 11 (2019) 20228-20237.

[123] H. Gao, J. Zang, Y. Wang, S. Zhou, P. Tian, S. Song, X. Tian, W. Li, One-step preparation of cobalt-doped NiS@ MoS2 core-shell nanorods as bifunctional electrocatalyst for overall water splitting, Electrochim. Acta 377 (2021) 138051.

[124] W.-H. Huang, X.-M. Li, X.-F. Yang, H.-B. Zhang, F. Wang, J. Zhang, Highly efficient electrocatalysts for overall water splitting: mesoporous CoS/MoS 2 with hetero-interfaces, Chem. Commun. 57 (2021) 4847-4850.

[125] Y. Li, H. Guo, Y. Zhang, H. Zhang, J. Zhao, R. Song, Hollow Mo-doped NiS x nanoarrays decorated with NiFe layered double-hydroxides for efficient and stable overall water splitting, J. Mater. Chem. A 10 (2022) 18989-18999.

[126] H. Zhang, B. Xi, Y. Gu, W. Chen, S. Xiong, Interface engineering and heterometal doping Mo-NiS/Ni (OH) 2 for overall water splitting, Nano Res. 14 (2021) 3466-3473.

[127] K. Min, S. Kim, E. Lee, G. Yoo, H.C. Ham, S.E. Shim, D. Lim, S.-H. Baeck, A hierarchical Co 3 O 4/CoS microbox heterostructure as a highly efficient bifunctional electrocatalyst for rechargeable Zn–air batteries, J. Mater. Chem. A 9 (2021) 17344-17352.

[128] Y. Tian, L. Xu, M. Li, D. Yuan, X. Liu, J. Qian, Y. Dou, J. Qiu, S. Zhang, Interface engineering of CoS/CoO@ N-doped graphene nanocomposite for high-performance rechargeable Zn–Air batteries, Nano-Micro Letters 13 (2021) 1-15.

[129] D. Guo, X. Li, Y. Jiao, H. Yan, A. Wu, G. Yang, Y. Wang, C. Tian, H. Fu, A dual-active Co-CoO heterojunction coupled with Ti3C2-MXene for highly-performance overall water splitting, Nano Res. 15 (2022) 238-247.

[130] J. Lu, H. Wang, Y. Sun, X. Wang, X. Song, R. Wang, Charge state manipulation induced through cation intercalation into MnO2 sheet arrays for efficient water splitting, Chem. Eng. J. 417

(2021) 127894.

[131] S. Zhu, J. Lei, L. Zhang, J. He, CoO/NF nanowires promote hydrogen and oxygen production for overall water splitting in alkaline media, Int. J. Hydrog. Energy 45 (2020) 8031-8040.

[132] J. Kim, J.N. Heo, J.Y. Do, R.K. Chava, M. Kang, Electrochemical synergies of heterostructured Fe2O3-MnO catalyst for oxygen evolution reaction in alkaline water splitting, Nanomaterials 9 (2019) 1486.

[133] K. Dai, N. Zhang, L. Zhang, L. Yin, Y. Zhao, B. Zhang, Self-supported Co/CoO anchored on N-doped carbon composite as bifunctional electrocatalyst for efficient overall water splitting, Chem. Eng. J. 414 (2021) 128804.

[134] S. Sirisomboonchai, X. Li, N. Kitiphatpiboon, R. Channoo, S. Li, Y. Ma, S. Kongparakul, C. Samart, A. Abudula, G. Guan, Fabrication of CuO x nanowires@ NiMnO x nanosheets core@ shell-type electrocatalysts: crucial roles of defect modification and valence states for overall water electrolysis, J. Mater. Chem. A 8 (2020) 16463-16476.

[135] M. Wang, Q. Wa, X. Bai, Z. He, W.S. Samarakoon, Q. Ma, Y. Du, Y. Chen, H. Zhou, Y. Liu, The Restructuring-Induced CoO x Catalyst for Electrochemical Water Splitting, JACS Au 1 (2021) 2216-2223.

[136] F. Nasim, H. Ali, A. Waseem, M.A. Nadeem, M.A. Nadeem, Confinement of CoOx-CoP nanoparticles inside nitrogen doped CNTs: A low-cost ORR electrocatalyst, Int. J. Hydrog. Energy 47 (2022) 39898-39907.

[137] Y. Lu, Z. Li, Y. Xu, L. Tang, S. Xu, D. Li, J. Zhu, D. Jiang, Bimetallic Co-Mo nitride nanosheet arrays as high-performance bifunctional electrocatalysts for overall water splitting, Chem. Eng. J. 411 (2021) 128433.

[138] Z. Liu, D. Liu, L. Zhao, J. Tian, J. Yang, L. Feng, Efficient overall water splitting catalyzed by robust FeNi 3 N nanoparticles with hollow interiors, J. Mater. Chem. A 9 (2021) 7750-7758.

[139] X. Zhou, Y. Mo, F. Yu, L. Liao, X. Yong, F. Zhang, D. Li, Q. Zhou, T. Sheng, H. Zhou, Engineering active iron sites on nanoporous bimetal phosphide/nitride heterostructure array enabling robust overall water splitting, Adv. Funct. Mater. 33 (2023) 2209465.

[140] C. Zhu, Z. Yin, W. Lai, Y. Sun, L. Liu, X. Zhang, Y. Chen, S.L. Chou, Fe-Ni-Mo nitride porous nanotubes for full water splitting and Zn-air batteries, Adv. Energy Mater. 8 (2018) 1802327.

[141] Y. Chen, Y. Wang, J. Yu, G. Xiong, H. Niu, Y. Li, D. Sun, X. Zhang, H. Liu, W. Zhou, Underfocus laser induced ni nanoparticles embedded metallic MoN microrods as patterned electrode for efficient overall water splitting, Adv. Sci. 9 (2022) 2105869.

[142] Y. Sun, Y. Zhou, Y. Zhu, Y. Shen, A. Xie, In-situ synthesis of petal-like MoO2@ MoN/NF heterojunction as both an advanced binder-free anode and an electrocatalyst for lithium ion batteries and water splitting, ACS Sustain. Chem. Eng. 7 (2019) 9153-9163.

[143] Q. Zhang, F. Luo, X. Long, X. Yu, K. Qu, Z. Yang, N, P doped carbon nanotubes confined WN-Ni Mott-Schottky heterogeneous electrocatalyst for water splitting and rechargeable zinc-air batteries, Appl. Catal. B Environ. 298 (2021) 120511.

[144] P. Wang, J. Qi, C. Li, X. Chen, T. Wang, C. Liang, N-doped carbon nanotubes encapsulating Ni/MoN heterostructures grown on carbon cloth for overall water splitting, ChemElectroChem 7 (2020) 745-752.

[145] R. Jamil, R. Ali, S. Loomba, J. Xian, M. Yousaf, K. Khan, B. Shabbir, C.F. McConville, A. Mahmood, N. Mahmood, The role of nitrogen in transition-metal nitrides in electrochemical water splitting, Chem Catalysis 1 (2021) 802-854.

[146] C. Feng, Y. Guo, S. Qiao, Y. Xie, L. Zhang, L. Zhang, W. Wang, J. Wang, 2-Methylimidazole as a nitrogen source assisted synthesis of a nano-rod-shaped Fe/FeN@ NC catalyst with plentiful FeN active sites and enhanced ORR activity, Appl. Surf. Sci. 533 (2020) 147481.

[147] R. Zhang, X. Xiao, Z. Wang, J. Huang, Z. Wang, Y. Dong, J. Liu, Heterostructural MoO2/MoC2 microspheres for efficient electrocatalytic hydrogen evolution, Mater. Lett. 297 (2021) 129973.

[148] H. Huang, L. Kong, M. Liu, J. He, W. Shuang, Y. Xu, X.-H. Bu, Constructing bifunctional Co/MoC@ NC catalyst via an in-situ encapsulation strategy for efficient oxygen electrocatalysis, J. Energy Chem. 59 (2021) 538-546.

[149] Q. Hu, X. Liu, B. Zhu, L. Fan, X. Chai, Q. Zhang, J. Liu, C. He, Z. Lin, Crafting MoC2-doped bimetallic alloy nanoparticles encapsulated within N-doped graphene as roust bifunctional electrocatalysts for overall water splitting, Nano energy 50 (2018) 212-219.

[150] Y. Yu, J. Zhou, Z. Sun, Novel 2D Transition-Metal Carbides: Ultrahigh Performance Electrocatalysts for Overall Water Splitting and Oxygen Reduction, Adv. Funct. Mater. 30 (2020)

2000570.

[151] Y. Lin, K. Sun, S. Liu, X. Chen, Y. Cheng, W.C. Cheong, Z. Chen, L. Zheng, J. Zhang, X. Li, Construction of CoP/NiCoP nanotadpoles heterojunction interface for wide pH hydrogen evolution electrocatalysis and supercapacitor, Adv. Energy Mater. 9 (2019) 1901213.

[152] X. Hu, S. Zhang, J. Sun, L. Yu, X. Qian, R. Hu, Y. Wang, H. Zhao, J. Zhu, 2D Fe-containing cobalt phosphide/cobalt oxide lateral heterostructure with enhanced activity for oxygen evolution reaction, Nano Energy 56 (2019) 109-117.

[153] X. Wang, W. Zhang, J. Zhang, Z. Wu, Fe-Doped Ni3S2 Nanowires with Surface-Restricted Oxidation Toward High-Current-Density Overall Water Splitting, ChemElectroChem 6 (2019) 4550-4559.

[154] P. Luo, H. Zhang, L. Liu, Y. Zhang, J. Deng, C. Xu, N. Hu, Y. Wang, Targeted synthesis of unique nickel sulfide (NiS, NiS2) microarchitectures and the applications for the enhanced water splitting system, ACS Appl. Mater. Interfaces 9 (2017) 2500-2508.

[155] T. Feng, F. Wang, Y. Xu, M. Chang, X. Jin, J. Piao, J. Lei, CoP/Ni2P heteronanoparticles integrated with atomic Co/Ni dual sites for enhanced electrocatalytic performance toward hydrogen evolution, Int. J. Hydrog. Energy 46 (2021) 8431-8443.

[156] L. Ma, K. Zhang, S. Wang, L. Gao, Y. Sun, Q. Liu, J. Guo, X. Zhang, Vanadium doping over Ni3S2 nanosheet array for improved overall water splitting, Appl. Surf. Sci. 489 (2019) 815-823.

[157] F. Li, D. Zhang, R.-C. Xu, W.-F. Fu, X.-J. Lv, Superhydrophilic heteroporous MoS2/Ni3S2 for highly efficient electrocatalytic overall water splitting, ACS Appl. Energy Mater. 1 (2018) 3929-3936.

[158] H. Li, S. Yang, W. Wei, M. Zhang, Z. Jiang, Z. Yan, J. Xie, Chrysanthemum-like FeS/Ni3S2 heterostructure nanoarray as a robust bifunctional electrocatalyst for overall water splitting, J. Colloid Interface Sci. 608 (2022) 536-548.

[159] Y. Li, Y. Bu, X. Chen, T. Zhu, J. Wang, S. Kawi, Q. Zhong, Facile Dynamic Synthesis of Homodispersed Ni3S2 Nanosheets as a High-Efficient Bifunctional Electrocatalyst for Water Splitting, ChemCatChem 11 (2019) 1320-1327.

[160] H. Xu, H. Shang, C. Wang, Y. Du, Recent progress of ultrathin 2D Pd-based nanomaterials

for fuel cell electrocatalysis, Small 17 (2021) 2005092.

[161] M. Li, Z. Xia, M. Luo, L. He, L. Tao, W. Yang, Y. Yu, S. Guo, Structural Regulation of Pd-Based Nanoalloys for Advanced Electrocatalysis, Small Science 1 (2021) 2100061.

[162] S. Han, C. He, Q. Yun, M. Li, W. Chen, W. Cao, Q. Lu, Pd-based intermetallic nanocrystals: From precise synthesis to electrocatalytic applications in fuel cells, Coord. Chem. Rev. 445 (2021) 214085.

[163] T. Gunji, F. Matsumoto, Electrocatalytic activities towards the electrochemical oxidation of formic acid and oxygen reduction reactions over bimetallic, trimetallic and core–shell-structured Pd-based materials, Inorganics 7 (2019) 36.

[164] Q.T. Phan, K.C. Poon, H. Sato, A review on amorphous noble-metal-based electrocatalysts for fuel cells: Synthesis, characterization, performance, and future perspective, Int. J. Hydrog. Energy 46 (2021) 14190-14211.

[165] X. Yang, A.-Y. Lu, Y. Zhu, M.N. Hedhili, S. Min, K.-W. Huang, Y. Han, L.-J. Li, CoP nanosheet assembly grown on carbon cloth: A highly efficient electrocatalyst for hydrogen generation, Nano Energy 15 (2015) 634-641.

[166] P. Wang, Z. Pu, W. Li, J. Zhu, C. Zhang, Y. Zhao, S. Mu, Coupling NiSe2-Ni2P heterostructure nanowrinkles for highly efficient overall water splitting, J. Catal. 377 (2019) 600-608.

[167] P. Zhai, Y. Zhang, Y. Wu, J. Gao, B. Zhang, S. Cao, Y. Zhang, Z. Li, L. Sun, J. Hou, Engineering active sites on hierarchical transition bimetal oxides/sulfides heterostructure array enabling robust overall water splitting, Nat. Commun. 11 (2020) 5462.

[168] X. Liu, Y. Yao, H. Zhang, L. Pan, C. Shi, X. Zhang, Z.-F. Huang, J.-J. Zou, In situ-grown cobalt–iron phosphide-based integrated electrode for long-term water splitting under a large current density at the industrial electrolysis temperature, ACS Sustain. Chem. Eng. 8 (2020) 17828-17838.

[169] M. Maleki, A. Sabour Rouhaghdam, G. Barati Darband, D. Han, S. Shanmugam, Highly active and durable NiCoSeP nanostructured electrocatalyst for large-current-density hydrogen production, ACS Appl. Energy Mater. 5 (2022) 2937-2948.

[170] H. Wu, L. Kong, Y. Ji, J. Yan, Y. Ding, Y. Li, S.T. Lee, S. Liu, Double-Site Ni–W Nanosheet for Best Alkaline HER Performance at High Current Density> 500 mA cm− 2, Advanced

Materials Interfaces 6 (2019) 1900308.

[171] M. Yu, Z. Wang, J. Liu, F. Sun, P. Yang, J. Qiu, A hierarchically porous and hydrophilic 3D nickel–iron/MXene electrode for accelerating oxygen and hydrogen evolution at high current densities, Nano Energy 63 (2019) 103880.

[172] C. Yu, F. Xu, L. Luo, H.S. Abbo, S.J. Titinchi, P.K. Shen, P. Tsiakaras, S. Yin, Bimetallic Ni–Co phosphide nanosheets self-supported on nickel foam as high-performance electrocatalyst for hydrogen evolution reaction, Electrochim. Acta 317 (2019) 191-198.

[173] P. Wang, Y. Luo, G. Zhang, M. Wu, Z. Chen, S. Sun, Z. Shi, MnOx-Decorated Nickel-Iron Phosphides Nanosheets: Interface Modifications for Robust Overall Water Splitting at Ultra-High Current Densities, Small 18 (2022) 2105803.

[174] X.-Y. Zhang, Y.-R. Zhu, Y. Chen, S.-Y. Dou, X.-Y. Chen, B. Dong, B.-Y. Guo, D.-P. Liu, C.-G. Liu, Y.-M. Chai, Hydrogen evolution under large-current-density based on fluorine-doped cobalt-iron phosphides, Chem. Eng. J. 399 (2020) 125831.

[175] S. Ma, J. Huang, C. Zhang, G. Chen, W. Chen, T. Shao, T. Li, X. Zhang, T. Gong, K.K. Ostrikov, One-step in-situ sprouting high-performance NiCoSxSey bifunctional catalysts for water electrolysis at low cell voltages and high current densities, Chem. Eng. J. 435 (2022) 134859.

[176] H. Yi, X. Zhang, Z. Ai, S. Song, Q. An, Hollow Nanowire Constructed by NiCo Doped RuO2 Nanoparticles for Robust Hydrogen Evolution at High-Current-Density, ChemSusChem 15 (2022) e202201532.